THE UNIVERSITY OF CHICAGO

THE NATURE OF α-SYNUCLEIN INTERACTIONS WITH MODEL MEMBRANE SYSTEMS: BINDING, STRUCTURE, AND PHYSIOLOGICAL IMPLICATIONS

A DISSERTATION SUBMITTED TO

THE FACULTY OF THE DIVISION OF THE PHYSICAL SCIENCES

IN CANDIDACY FOR THE DEGREE OF

DOCTOR OF PHILOSOPHY

DEPARTMENT OF CHEMISTRY

BY

HYEONDO LUKE HWANG

CHICAGO, ILLINOIS

JUNE 2020

Dedicated to *Nam Jung Ok*, my grandmother

TABLE OF CONTENTS

LIST OF FIGURES

LIST OF TABLES

LIST OF ABBREVIATIONS

αS	alpha synuclein
αSΔCTD	C-terminal domain truncated alpha synuclein
αSF4W	Tryptophan mutant of alpha synuclein (fourth residue, phenylalanine, mutated to tryptophan)
CBS	citrate buffered saline
Chol	cholesterol
DLS	dynamic light scattering
DOPC	1,2-dioleoyl-sn-glycero-3-phosphocholine
DOPS	1,2-dioleoyl-sn-glycero-3-phospho-L-serine
DOPA	1,2-dioleoyl-sn-glycero-3-phosphate
DOPE	1,2-dioleoyl-sn-glycero-3-phosphoethanolamine
DOTAP	1,2-dioleoyl-3-trimethylammonium-propane
DSPE	1,2-distearoyl-sn-glycero-3-phosphorylethanolamine
EGTA	ethylene glycol-bis(β-aminoethyl ether)-N,N,N′,N′-tetraacetic acid
GFP	green fluorescent protein
HB7	HEPES (10 mM) + NaCl (100 mM) buffer at pH 7
HBS	HEPES buffered saline
HEPES	4-(2-hydroxyethyl)-1-piperazineethanesulfonic acid
LUV	large unilamellar vesicle
MW	molecular weight
NAC	non-amyloid-beta component
PEG	polyethylene glycol
PEG10k	polyethylene glycol with an average MW 10,000

PDI	polydispersity index
SAXS	small angle X-ray scattering
SLB	supported lipid bilayer
SNARE	soluble NSF attachment proteins receptor
SSLB	spherical silica nanoparticle supported lipid bilayer
SUV	small unilamellar vesicle
TEM	transmission electron microscope
XPCS	X-ray photon correlation spectroscopy

ACKNOWLEDGMENTS

I couldn't have completed this dissertation without the enormous support of people who have patiently guided me over the last six and a half years. First person I acknowledge is my advisor Ka Yee C. Lee, an accomplished applied physicist and a wonderful human being all around. I cannot thank Ka Yee enough for her extraordinary patience and faith in me especially in the early years of research when I, struggling through multiple projects and not fulfilling my own expectations of myself, lacked the confidence to move forward and enjoy the art of scientific research. She uplifted and empowered me as a scientist, bearing with me through the ups and downs of graduate level research and giving me, above all else, the space to grow – to be the composed and critically thinking scientist that I am today. I would also point out that her personal qualities of generosity, good-naturedness, and concern for others are most inspiring and worthy of emulation. It has been a huge privilege for me to be her graduate student.

I have been the recipient of a gracious and supportive research environment – that is the Lee Lab. I would like to thank the current members of the lab: Peter, Dan, Ben, Sofi, Miah, Tiffany, and Sam. Every one of them offered me friendship, advice (scientific and otherwise), and concrete help. My special thanks to Peter whom I worked closely with on a complex project with many working parts, and my best wishes to him as he begins his physics professorship next year. I thank the past Lee Lab members as well for their friendship and help in various ways: Alessandra, Zhiliang, Michael, Andrew, Nishanth, Lanijah, Pascale, Kathleen, Charles, and more. Everyone in the lab inspired me in their unique way and has made my journey all the more meaningful.

I have been fortunate to collaborate and do experiments with biologists, chemists, physicists. The fact that my dissertation work required me to be reasonably proficient in all three branches of science made it really challenging and also fulfilling at the same time. A big thank you to my collaborators, it was a pleasure to think about science together and do experiments side-by-side: Qingteng, Suresh, and Eric for X-ray photon correlation spectroscopy at Sector 8, Argonne National Laboratory; Ivan and Thomas for small angle X-ray scattering at beamline 4-2, Stanford Synchrotron Radiation Laboratory; David and Tapo for α-Synuclein and NMR measurements at Weill Cornell; Wei, Binhua, and Joe Z. for X-ray reflectivity and diffraction of lipids at Sector 15, Argonne; and Erin Adams in the biochemistry department at the University of Chicago whose facilities we used to express and purify α-Synuclein and do molecular biology. I also carried out a lot of measurements in university facilities including the Material Research Science & Engineering Center Materials Property Measurements lab (MRSEC MPML), Biophysics core, and Advanced Electron Microscopy core. I would like to thank the technical directors Justin, Qiti, Elena, Tera, and Joe for helping me with instruments and measurements of all sorts.

I would like to acknowledge the support groups within the university: Center for Identity + Inclusion, UChicago first-generation, low income, and immigrant (FLI) student network, (a special thanks to Ireri Rivas, its director, and Haekyung Im, professor of genetics and a FLI mentor, for being extremely supportive of me personally), UCCIR, UChicagoGRAD for connections and various help. An important part of my life in Chicago has been my involvement in the local community and non-profit grassroots organizations, which have been the lifeblood of friendships and community — Hana Center, ENoK,

HPKMC, and NAKASEC, all of which have given me a fresh meaning on how I ought to live my life and give back to the people and communities I strongly identify with. In this regard I would like to acknowledge two personal mentors, Inhe Choi and Nayoung Ha, who have watched and inspired my personal growth over the years. While leading truly remarkable lives of their own, they have always been there for me as role models since the beginning of my PhD journey and owe them my gratitude for accepting me for who I am and also for challenging me to venture outside of my comfort zone.

A special thank you to friends and family. There are too many friends to name so I will not get to name everyone in this document, but I know I have made lifelong friendships during my time in Chicago. I would like to thank Shinhae, my dear wife and my best friend. I look forward to our life ahead. I would like to thank my parents and my brother for being understanding and supportive in ways I couldn't dare imagine. I would also like to thank my grandma, an angel who raised me through my childhood and teen years and loves me unconditionally.

Finally, I would like to acknowledge Profs. Bozhi Tian and Norbert Scherer for being on my sixth-year and thesis committee. I appreciate your energy, time, and rigorous feedback on my research. And I would like to acknowledge the National Science Foundation grant (Award #1413613) that supported my research.

ABSTRACT

This dissertation work aims to advance the current understanding of the native function of α-Synuclein (αS), an intrinsically disordered protein whose intraneuronal aggregation is most notably recognized as a pathological hallmark of Parkinson's disease, among many other neurodegenerative disorders classified as synucleopathies. The putative function of αS is its interaction with synaptic vesicles, though it remains unclear on the molecular level how its membrane binding and surface activity can specifically regulate synaptic vesicle organization and homeostatic mechanisms at large. From a membrane biophysics perspective, the partial folding of αS leading to helix formation on synaptic membrane surface presents several interesting questions in the context of functional relevance of its membrane bound structure. While the first ~100 residues participate in lipid binding, the remaining 40 residues (the C-terminal domain) retain the protein's intrinsic disorder, creating a physisorbed polymer on the membrane surface. How the sterically projecting C-terminal domain can mediate the interactions of synaptic vesicles with one another is an important fundamental question we address.

We probe αS interactions with model membranes mimicking synaptic vesicles using biophysical approaches inspired by nano-bio interface, X-ray scattering, and polymer physics. We first produce and validate a silica nanoparticle-based model membrane system that mimics the curvature and composition of a synaptic vesicle using electron microscopy and isothermal titration calorimetry. We then examine the surface activity of membrane bound αS by a combination of small angle X-ray scattering, depletion force response, and X-ray photon correlation spectroscopy, in order to characterize the polymeric nature of the C-terminal domain. We find that our model

system, spherical supported lipid bilayers (SSLBs), can be efficiently prepared by a generalizable osmotic stress approach. We demonstrate that a critical density of αS on SSLB surface confers complete steric stabilization of SSLBs, which is driven by the polymeric properties of the C-terminal domain that were assessed from quantitating its steric effect with depletion force measurements. Overall, our findings implicate the role of αS in the release of synaptic vesicles from clustered pools within the presynaptic terminal— an important physiological step in the propagation of neurotransmission. The biophysical insights obtained from fundamental αS-membrane interaction experiments establish structure-property relationships in the context of the synaptic vesicle organization.

CHAPTER 1.

BACKGROUND AND MOTIVATION

1.1. Background

Structure and function of α-Synuclein (αS) remain an active area of research in biophysics and beyond, as αS manifests as a major structural component of intracellular protein aggregates called Lewy bodies (Fig. 1.1) found in Parkinson's disease, multiple system atrophy, Lewy body dementia, and Alzheimer's disease — all of which affect millions of people worldwide.[1–4] Since the first identification of αS in Lewy bodies in 1997,[4] *in vitro* biophysical efforts have broadly focused on: (1) identifying the molecular mechanisms of αS aggregation, (2) how its aggregation leads to neuronal toxicity and contributes to overall neurodegeneration, and (3) understanding the healthy, physiological function of αS in the neuron. Strikingly, the community still cannot clearly define what αS does in the body — a key missing piece of information needed to address the group of neurodegenerative diseases classified as "synucleopathies," where aggregation of αS is the defining pathological hallmark.[3,5]

This dissertation work aims to elucidate the normal function of αS through a set of biophysical experiments using model lipid membrane systems, mimicking the ones found under physiological conditions. All experiments in this work are performed in non-aggregating conditions for αS, specifically to capture how αS monomer interacts with lipid membranes and reveal the unknowns of αS-lipid interactions in the physiological context. In the αS community it has been well known that the protein is highly expressed in the presynaptic terminal (the biological junction within the neuron containing chemical information that needs to be transmitted from one neuron to the next)

constituting as much as 0.5 to 1.0% of all cytosolic proteins[6] and interacts directly with lipid vesicles known as synaptic vesicles that are responsible for neurotransmission. This work characterizes the structure-property relationships of membrane-bound αS and attempt to bridge the gap between protein's biophysical behavior and pathophysiological states. The obtained results and insights can help establish rigorous drug development contexts and aid *in vivo* experiments critical to understanding pathogenesis of diseases mentioned above and to developing suitable therapeutic targets.

1.2. Structural characteristics of α-Synuclein (αS)

Structurally, αS is a 14-kDa, 140-residue, intrinsically disordered protein that folds partially upon membrane binding, forming a helical structure. It is often described by three functional domains (Fig. 1.1B):

1. The amino terminus (residues 1-64) is rich with positively charged and amphipathic lysines, which contribute to crucial interaction with lipid membranes. The reason for helix formation on the membrane is its 11-mer repeat sequence with a KTKGEV motif present throughout the first 95 residues.[5,7] The helix wheel of αS shows localization of hydrophobic and cationic residues in such a way that promote αS interactions with anionic lipids and hydrophobic core of the membrane. The mutations identified with disease states all occur in this region: A30P, E46K, H50Q, G51D, A53E, and A53T, hinting at changes in membrane binding in disease and increase in αS self-association.[5]
2. The intermediate hydrophobic residues (65-95) comprise a region known as the non-amyloid-beta component (NAC) that is responsible for αS aggregation.

Deletion of this region has been shown to prevent *in vitro* αS aggregation and fibril formation.[8] The research community generally denotes residues 1 through 95 as the "N-terminal domain" of αS.

3. Finally, the carboxyl terminus (96-140) is the acidic, persistently disordered tail that may have a variety of small molecule, protein, and ion interaction partners. Unlike the N-terminal domain, the disorder persists upon membrane binding. It is unclear to what extent the tail has disease relevance, but its presence inhibits αS from natural aggregation and may also alter membrane binding. As with other intrinsically disordered proteins, αS may be inherently multifunctional and carry a dynamic and homeostatic role, as its lack of intrinsic structure allows it to adopt multiple conformations depending upon its interaction partners.[7] The C-terminal domain may be important for this conformational flexibility and the diverse behavior of αS on biological substrates.

From a purely structural perspective the seeding and fibrillation of αS continue to be a challenging problem for pathogenesis and disease states. Although this dissertation work does not cover this topic and focuses entirely on αS-lipid membrane interactions, there have been excellent review articles and published cryo-EM fibril structures that delve into the structural biology and biophysics of pathogenic forms.[9–11]

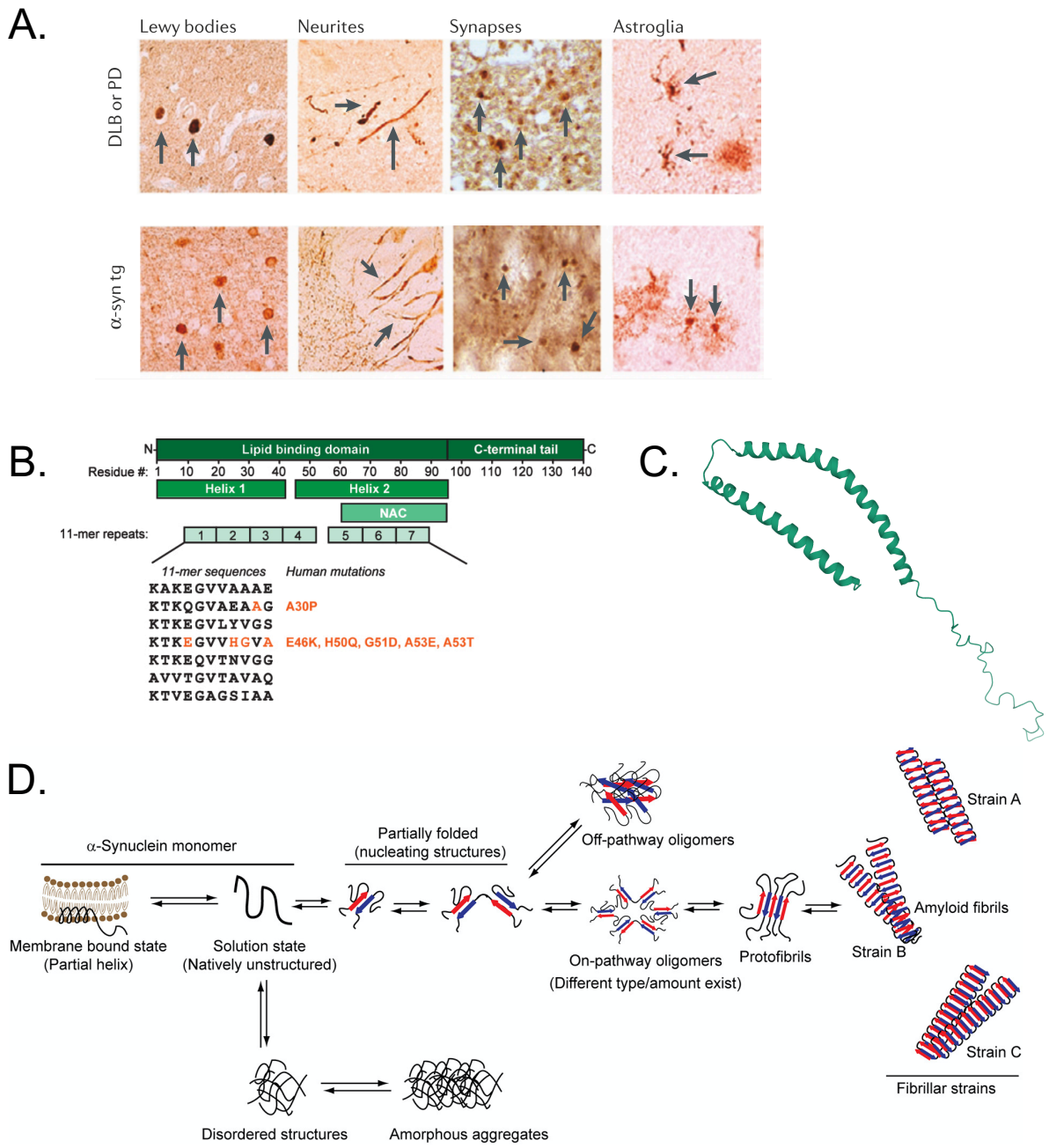

Fig. 1.1. Structure and aggregation of α-Synuclein (αS).
(A). Aggregated αS, indicated by arrows, is present throughout Lewy bodies, neurites, synapses and astroglia in Lewy body dementia and Parkinson's disease, as well as in transgenic (tg) mice overexpressing human wild-type αS. Reproduced from ref. (2).
(B). The domain structure of αS depicting the lipid-binding domain (N-terminal domain), NAC region, and C-terminal tail (or C-terminal domain). Highly conserved 11-mer sequences responsible for helix formation are shown, as well as the identified mutations linked to human disease states. Reproduced from ref. (5).
(C). Schematic of a micelle-bound αS (Protein data bank ID: 1XQ8) showing the two helices and disordered C-terminal domain.

(D). Natively unstructured αS, while it monomerically interacts with membrane, can form amorphous aggregates, oligomers, and multiple fibrillar strains. Adapted from ref. (29).

1.3. Current cellular and animal models suggest a nuanced regulatory role of αS in the axon terminal

The healthy function of αS has been rigorously explored in a variety of cellular and animal experiments via knockout, depletion, or overexpression in appropriate models. The current consensus is that αS, predominantly expressed in the brain, is not an essential protein (αS knockout mice still survive despite some age-dependent overall neurological impairments[12,13]) but is involved in the normal, long-term regulation of neurotransmitter release, synaptic vesicle cycle, and overall neuronal plasticity.

We first note that the literature on knockout or overexpression studies appear conflicting for the specific effect of αS on synaptic transmission. Several studies for instance showed no discernible effect of αS on neurotransmitter release,[12,14,15] but most studies contend *some* deficiency in synaptic transmission (due to αS knockout or overexpression) with some suggesting that αS is responsible for generally enhanced synaptic transmission[16–18] and others for impaired transmission.[19–21] At a first glance, there is not much consistency — what can we make of these conflicting results? First, it is clear that some discrepancy is bound to result from experimental models, investigated brain regions, and so on. Second, we cannot discount the existence of synuclein isoforms (β- and γ-synuclein) that may be playing a "compensatory" function for αS in the event of single αS knockout or overexpression. This might be the reason why some studies revealed little to no neurotransmission effect.[5] Some have taken this possibility into account and knocked out *all* synucleins to observe physiological effects, revealing that in

the absence of all synucleins expression, the presynaptic terminal size decreased by ~30% both *in vivo* and *in vitro*, and additionally, aged mice (12 months old) showed changes in overall synaptic protein composition and impairment in neurobehavioral responses.[13]

What happens to synaptic vesicle maintenance when αS is compromised by knockout or overexpression? The findings to this question are less contradictory, compared to the question of synaptic transmission. The *SNCA* (gene encoding αS) knockout mice show impaired trafficking of synaptic vesicles, from being unable to replenish these vesicles once they are used up for neurotransmitter release.[22,23] Tissue derived primary cultures of hippocampal neurons support this picture, showing a reduction in available reserve synaptic vesicles.[24] In the opposite limit, αS overexpression mice show reduced synaptic vesicle exocytosis by inhibiting vesicle re-clustering after exocytosis,[19] as do rodent models[25,26] and cell lines.[21] Ultrastructural changes to the presynaptic terminal have been documented, showing a reduction in the size of synaptic vesicle recycling pool.[12,27] Overall, compromising αS levels leads to an imbalance of mobilized synaptic vesicles (for direct neurotransmission) and reserve vesicles sequestered within the neuron which need to be activated for mobilization.

The picture that emerges from the studies referenced above is a nuanced regulatory physiological role of αS at the animal and cellular scale. Clarification is needed at the molecular level to ascertain αS interactions with its binding partners — the most well known of which is the synaptic vesicle membrane surface.

1.4. Where αS comes into play: Synaptic vesicles and their regulation

Consistent with its presynaptic prevalence and amphipathic nature, αS association with synaptic vesicles has been well documented.[28] Regulated membrane binding of αS has been posited to organize synaptic vesicles, how they are used and recycled.[1,29]

Synaptic vesicles are the basic subcellular units of neurotransmission, carrying chemical messengers from cell to cell via highly regulated loading of neurotransmitters, docking and priming at the neuronal membrane, fusion with the membrane to release neurotransmitters, and recycling back to "reserve" pools so they can be used for the next cycle (Fig. 1.2). At some points of this process there exist intricate protein machineries such as the well-studied SNARE proteins that mediate synaptic vesicle fusion,[30] and much has been revealed about the neurotransmitter release process upon calcium stimulation.[31,32] Here it suffices to say that while the big picture sequence of steps is established, the molecular complexity of specific steps is relatively unknown — for instance, the identity and mechanism of the protein matrix that holds synaptic vesicles together in pooled states remain unclear.[33] The mechanism for activation and mobilization of synaptic vesicles from pools is another important question. Moreover, how the vesicles recluster and get recruited back to the reserve pools continue to puzzle the research community.[34] The synaptic vesicles are composed of a diverse mixture of embedded membrane proteins and phospholipids; the lipid composition from mass spectrometric analysis is shown in Fig. 1.2.[35]

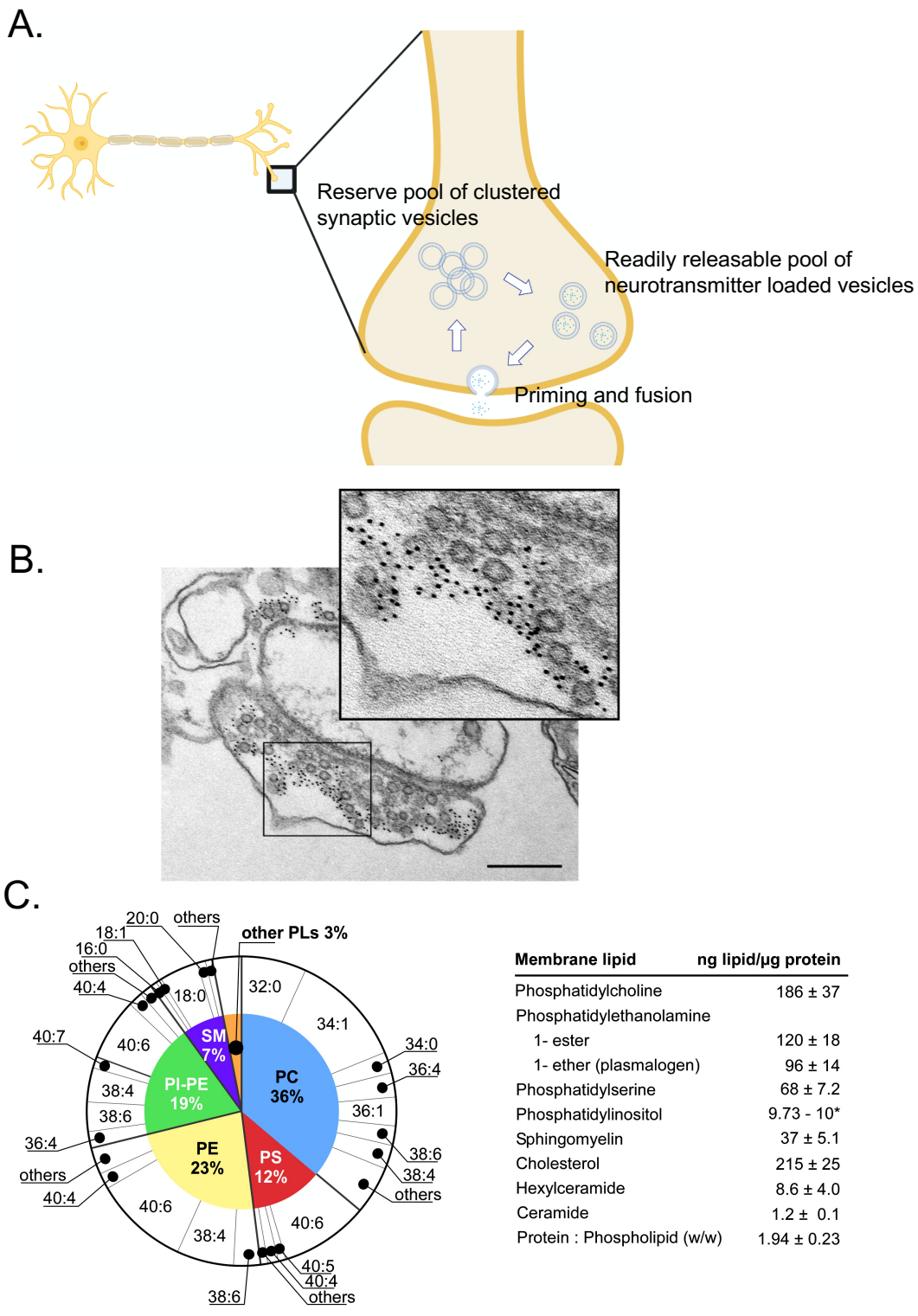

Membrane lipid	ng lipid/µg protein
Phosphatidylcholine	186 ± 37
Phosphatidylethanolamine	
1- ester	120 ± 18
1- ether (plasmalogen)	96 ± 14
Phosphatidylserine	68 ± 7.2
Phosphatidylinositol	9.73 - 10*
Sphingomyelin	37 ± 5.1
Cholesterol	215 ± 25
Hexylceramide	8.6 ± 4.0
Ceramide	1.2 ± 0.1
Protein : Phospholipid (w/w)	1.94 ± 0.23

Fig. 1.2. Clues to αS native function: synaptic vesicles and their regulation. (A). Simplified schematic of the synaptic vesicle cycle showing the trafficking of vesicles. They are initially condensed in clusters called "reserve pool" and upon neurotransmitter loading, segregate to a "readily releasable pool." Then they are actively transported to the

Fig. 1.2. Clues to αS native function: synaptic vesicles and their regulation (cont'd).
neuronal membrane, where they undergo "priming" to initiate and execute fusion, releasing the transmitters.
(B). The putative function of αS is its interaction with synaptic vesicles. An electron micrograph showing the localization of immunogold-labeled αS with synaptic vesicles. Scale bar: 500 nm. Adapted from ref. (28).
(C). The lipid composition of purified synaptic vesicles showing a diverse mixture of phospholipids. Adapted from ref. (35).

Possible association of αS with other presynaptic proteins has received frequent attention: SNARE involved protein synaptobrevin-2,[14] in a way that αS promotes SNARE activity; synapsin III,[36] which is a protein regulator of dopamine release; tyrosine hydroxylase,[37] which regulates dopamine synthesis; G-protein Rab3,[38] which regulates Ca^{++} triggered release; and several dopamine and serotonin transporters.[39–41] Adding to the complexity is the presence of β- and γ-Synuclein that show considerable sequence similarity (55-62 % sequence similarity) especially in the N-terminal domain (~80% similarity), that may have compensatory functions in the event of αS downregulation.[12,13] β-Synuclein, which does not have the NAC region, has been shown to inhibit αS from self-association[42] and γ-Synuclein when oxidized has been shown to seed the aggregation of αS.[43] All of these findings point to the overall dynamic binding of αS to multiple partners.

1.5. Biophysics of αS interactions with the lipid membrane

In the lipid biophysics community, the interest in αS was driven by the protein's ability to "sense" a key physical property of the lipid membrane: membrane curvature. Generally, cells and organelles vary greatly in size and shape, and subsequently in their local and global curvature. Electron microscopy over the past few decades has revealed all sorts of diverse membrane morphologies and curvatures, ranging from the multiply

folded mitochondrial membrane to the highly curved membrane surface of a synaptic vesicle whose average diameter is 40 nm and is recognized to have the most highly curved subcellular membrane curvature.[31,34] Of course, the curvature depends on the molecular constituents of the lipid membrane, which are phospholipids and membrane proteins embedded in the lipid bilayer; the lateral packing of these contents is responsible for physicochemical properties of the membrane. In the last decade, however, it has been recognized that membrane curvature is more than simply a result of its contents or of protein binding that deforms membrane geometry; curvature is now increasingly considered as a guide and effector of biochemical processes in the cell.[44] This means, for example, that some proteins are able to "sense" membrane curvature and selectively interact with regions of specific curvature. As another example, curvature can "organize" specific chemical reactions spatiotemporally in vesicular trafficking and fusion.

Numerous model membrane binding experiments have shown smaller average diameter of vesicles (i.e. higher membrane curvature) dramatically increased αS binding affinity.[44–46] This is consistent with the amphipathic character of the helices and positioning of cationic residues when αS interacts with the membrane. As the lateral packing is disrupted on a highly curved membrane, the hydrophobic tails of the lipids are more exposed to solvent, and amphipathic helices like ones found in αS can effectively embed into the tail region (Fig. 1.3).[47] However, it must be noted that conventional vesicles used for biophysical experiments do not quite recapitulate the monodisperse curvature of synaptic vesicles (40 nm diameter, reported to "swell" up to 60 nm upon neurotransmitter loading[48]) so a better biophysical mimic of synaptic vesicles can be envisioned — this the subject of Chapter 2. The elucidation of how αS binding responds

to very small changes in curvature (40-60 nm in diameter) of synaptic vesicles, would be important to our understanding of the nature of αS binding to membranes.

In addition to curvature, higher binding affinity has been correlated with (1) increased anionic lipids in the vesicle composition[49]; (2) Increased conical lipids in the vesicle composition (meaning that their headgroup area is small with higher exposure of the hydrophobic tails to the solvent)[49]; (3) Increased levels of lipid unsaturation[50]; and (4) Vesicles in the low-temperature gel phase, in which the lipids have significantly reduced mobility and cannot seal the local voids and holes in the bilayer.[51] All of these observations point to the fact that αS binds more strongly to membranes with a higher density of *packing defects*, the general parameter that governs αS membrane binding (Fig. 1.3). In all conditions listed above, the lateral lipid packing is disrupted by inclusion of lipids with small head groups, or with higher degree of tail unsaturation, or via external conditions that introduce packing defects for αS to "sense" and peripherally interact with the membrane.

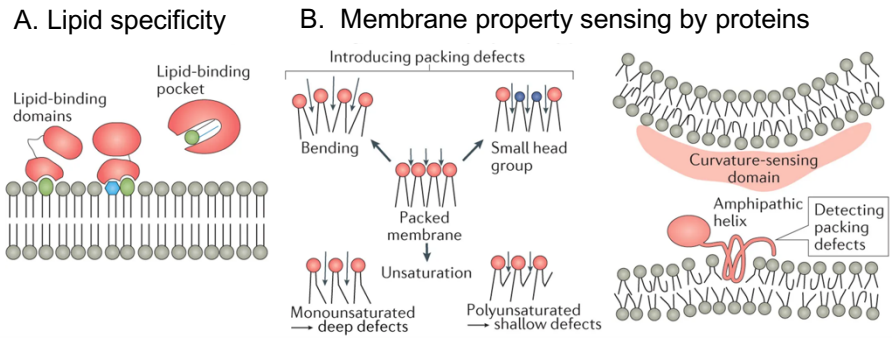

Fig. 1.3. Peripheral binding proteins such as αS can sense membrane properties.
(A). Protein recognition of specific lipids by binding domains or pockets on the protein. (B). Recognition of curvature and packing defects imparted by the composition and geometry of lipids. Adapted from ref. (47).

Upon membrane binding, different membrane-bound conformations of αS have been reported (Fig. 1.4). One continuous amphipathic helix that spans the first 95 residues, through an unusual 11/3 periodicity (11 residues forming 3 helical turns), may lie linearly on the membrane — this is known as the "extended-helix" conformation.[7] Alternatively, two broken helices connected by a region of residues 39-45 that remain non-helical can also exist — a "broken helix" conformation. The broken helix conformation is interesting because it has been proposed to "bridge" two membrane surfaces that is especially relevant in clustering of synaptic vesicles and as a prelude to a fusion event.[7,52] In light of this knowledge, some have hypothesized that the modulation between the extended helix and broken helix conformations via protein-protein interactions and/or post-translational modifications can define αS physiological contexts and activities, but this conformational switch is still unclear.

The possibility of αS bridging apposing membrane surfaces is noteworthy because synaptic vesicles exist in dense clusters and membrane-less "pools" within the neuron. In fact, this observation has led to biologists even classifying two major clusters of synaptic vesicles: one being the reserve pool, which stores neurotransmitter-unloaded vesicles that have to be activated/loaded, and another being the readily releasable pool, which stores neurotransmitter-loaded vesicles that are readily recruited to the sites of fusion for transmission activity.[31,33] It would be an exciting discovery if the dynamic binding of αS (possibly through conformational switches) happens to play an active role in the clustering and de-clustering of synaptic vesicles — the subject of Chapters 3 and 4.

Lastly, the way in which αS selectively binds to certain synaptic vesicle population[53] is a continuing question that relates to the role αS plays in the regulation of

vesicles. Whether this is just a characteristic of its low affinity and being intrinsically disordered, or its binding is biologically or biophysically modulated — is a question currently being explored in our laboratory (Chapter 5).

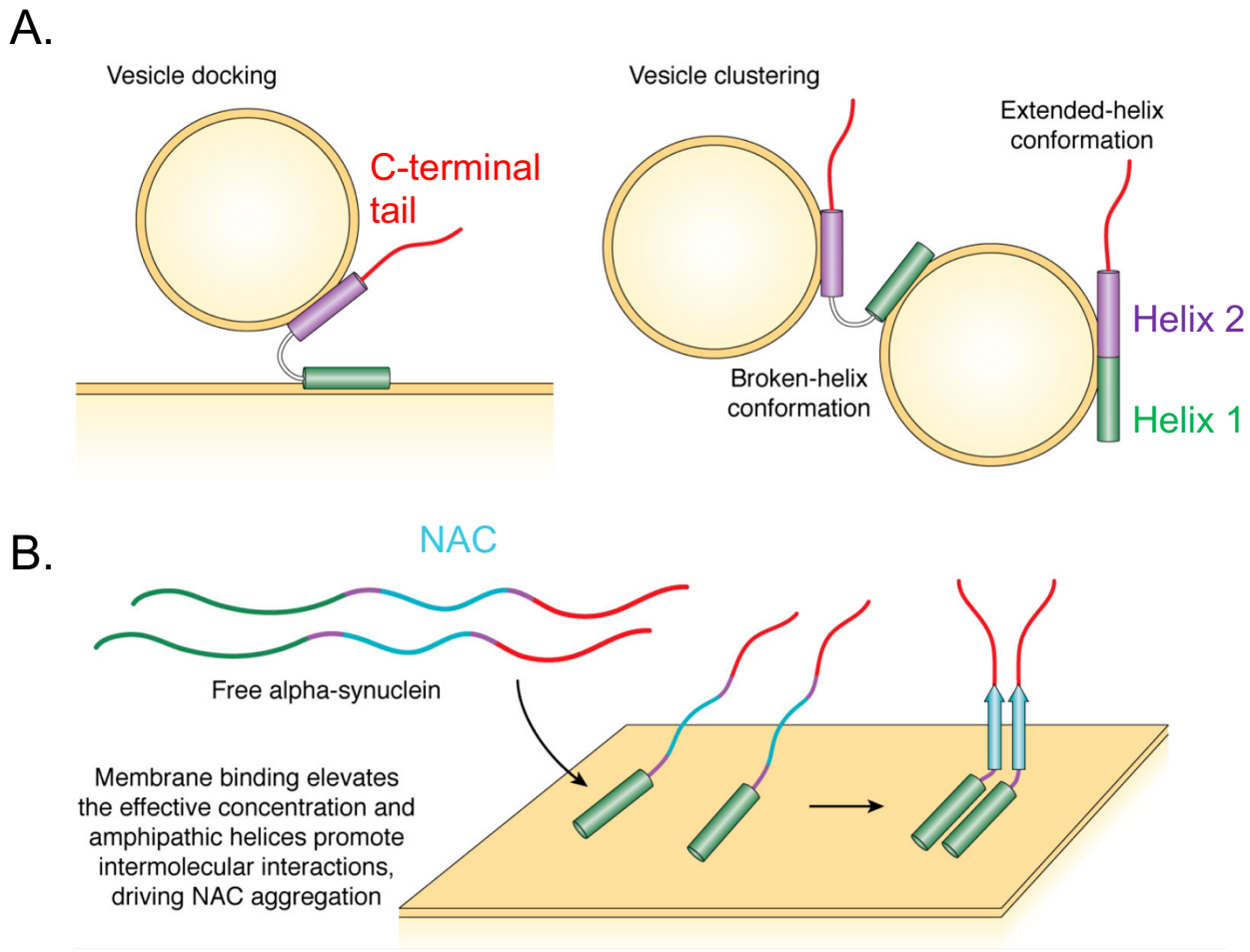

Fig. 1.4. Conformational plasticity of αS in the context of possible membrane-bound structures.
(A). The two helices of αS have shown distinct conformations, fully extended or broken-helix. The broken-helix conformation is thought to bridge two membrane surfaces by docking the vesicle to adjacent membrane or cluster two vesicles together.
(B). There is evidence for αS association and/or multimerization on the membrane surface. Adapted from ref. (7).

1.6. Specific aims and organization of the thesis

The thesis is organized in accordance with the questions hinted and directly raised in the preceding sections.

- Could we create and employ a model membrane system that mimics key biophysical properties of synaptic vesicles — i.e., membrane curvature and anionic charge content?
- Could we better understand the functional significance of the partially folded structure of αS on lipid membrane surfaces?
- How might αS biophysically modify membrane-membrane interactions and modulate the dense clustering (or de-clustering) of synaptic vesicles?
- What is the role of each functional domain of αS in its normal functioning?
- How does αS sense which vesicle surface to bind?
- Could we hypothesize what role αS plays in the synaptic vesicle cycle?

Keeping with these questions, the organization of the dissertation is as follows: the design and development of spherical silica nanoparticle supported lipid bilayers as a biophysical probe (Chapter 2); the steric stabilization of membrane surfaces conferred by αS binding (Chapter 3); the structure-property relationships behind steric stabilization (Chapter 4); the membrane selectivity of αS in the context of steric stabilization (Chapter 5), and conclusions and outlook (Chapter 6). This arrangement of chapters is roughly in the chronological order of how I carried out this project.

1.7. List of publications

Sachan, A. K.; Choi, S. Q.; Kim, K. H.; Tang, Q.; Hwang, L.; Lee, K. Y. C.; Squires, T. M.; Zasadzinski, J.A. Interfacial rheology of coexisting solid and fluid monolayers. *Soft Matter* 2017, *13* (7), 1481–1492.

Gong, Z.; Kerr, D.; Hwang, H. L.; Henderson, J. M.; Suwatthee, T.; Slaw, B. R.; Cao, K. D.; Lin, B.; Bu, W.; Lee, K. Y. C. Quantitative analysis of total reflection X-ray fluorescence from finely layered structures using XeRay. *Rev. Sci. Instrum.* 2017, *88* (3), 033112.

Chung, P. J.; Hwang, H. L.; Dasbiswas, K.; Leong, A.; Lee, K. Y. C. Osmotic shock-triggered assembly of highly charged, nanoparticle-supported membranes. *Langmuir* 2018, *34* (43), 13000-13005.

Chung, P. J.; Zhang, Q.; Hwang, H.L.; Leong, A.; Dufresne, E.; Narayanan, S.; Adams, E.J.; Lee, K. Y. C. α-sterically stabilizes spherical nanoparticle supported lipid bilayers. *ACS Appl. Bio Mater.* 2019, *2* (4), 1413-1419.

Chung, P. J.; Hwang H. L.; Slaw, B. R.; Leong, A.; Adams, E. J.; Lee, K. Y. C. The C-terminal domain is the predominant contributor of steric stabilization conferred by a-Synuclein on synaptic vesicle-like surfaces." *Adv. Mater. Interfaces,* 2020, *Accepted.*

Hwang, H.L., et al. "Chemical and physical determinants of α-Synuclein binding to osmotically stressed model membranes" In preparation, 2020

1.8. References

(1) Wong, Y. C.; Krainc, D. α-Synuclein Toxicity in Neurodegeneration: Mechanism and Therapeutic Strategies. *Nat. Med.* **2017**, *23*, 1–13. https://doi.org/10.1038/nm.4269.

(2) Lashuel, H. A.; Overk, C. R.; Oueslati, A.; Masliah, E. The Many Faces of α-Synuclein: From Structure and Toxicity to Therapeutic Target. *Nat. Rev. Neurosci.* **2013**, *14*, 38–48. https://doi.org/10.1038/nrn3406.

(3) Goedert, M. Alpha-Synuclein and Neurodegenerative Diseases. *Nat. Rev. Neurosci.* **2001**, *2*, 492–501. https://doi.org/10.1038/35081564.

(4) Spillantini, M. G.; Schmidt, M. L.; Lee, V. M. Y.; Trojanowski, J. Q.; Jakes, R.; Goedert, M. α-Synuclein in Lewy Bodies. *Nature* **1997**, *388* (6645), 839–840. https://doi.org/10.1038/42166.

(5) Burré, J. The Synaptic Function of α-Synuclein. *J. Parkinsons. Dis.* **2015**, *5* (4), 699–713. https://doi.org/10.3233/JPD-150642.

(6) Iwai, A.; Masliah, E.; Yoshimoto, M.; Ge, N.; Fianagan, L.; Rohan De Silva, H. A.; Kittei, A.; Saitoh, T. The Precursor Protein of Non-Ab Component of Alzheimer's Disease Amyloid Is a Presynaptic Protein of the Central Nervous System. *Neuron* **1995**, *14*, 467–475.

(7) Snead, D.; Eliezer, D. Intrinsically Disordered Proteins in Synaptic Vesicle Trafficking and Release. *J. Biol. Chem.* **2019**, *294* (10), 3325–3342. https://doi.org/10.1074/jbc.REV118.006493.

(8) Bodles, A. M.; Guthrie, D. J. S.; Greer, B.; Brent Irvine, G. Identification of the Region of Non-Aβ Component (NAC) of Alzheimer's Disease Amyloid Responsible for Its Aggregation and Toxicity. *J. Neurochem.* **2001**, *78* (2), 384–395. https://doi.org/10.1046/j.1471-4159.2001.00408.x.

(9) Guerrero-Ferreira, R.; Taylor, N. M. I.; Mona, D.; Ringler, P.; Lauer, M. E.; Riek, R.; Britschgi, M.; Stahlberg, H. Cryo-EM Structure of Alpha-Synuclein Fibrils. *Elife* **2018**, *7*. https://doi.org/10.7554/eLife.36402.

(10) Li, Y.; Zhao, C.; Luo, F.; Liu, Z.; Gui, X.; Luo, Z.; Zhang, X.; Li, D.; Liu, C.; Li, X. Amyloid Fibril Structure of α-Synuclein Determined by Cryo-Electron Microscopy. *Cell Res.* **2018**, *28* (9), 897–903. https://doi.org/10.1038/s41422-018-0075-x.

(11) Li, B.; Ge, P.; Murray, K. A.; Sheth, P.; Zhang, M.; Nair, G.; Sawaya, M. R.; Shin, W. S.; Boyer, D. R.; Ye, S.; et al. Cryo-EM of Full-Length α-Synuclein Reveals Fibril Polymorphs with a Common Structural Kernel. *Nat. Commun.* **2018**, *9* (1), 1–10. https://doi.org/10.1038/s41467-018-05971-2.

(12) Chandra, S.; Fornai, F.; Kwon, H. B.; Yazdani, U.; Atasoy, D.; Liu, X.; Hammer, R. E.; Battaglia, G.; German, D. C.; Castillo, P. E.; et al. Double-Knockout Mice for α- and β-Synucleins: Effect on Synaptic Functions. *Proc. Natl. Acad. Sci. U. S. A.* **2004**, *101* (41), 14966–14971. https://doi.org/10.1073/pnas.0406283101.

(13) Greten-Harrison, B.; Polydoro, M.; Morimoto-Tomita, M.; Diao, L.; Williams, A. M.; Nie, E. H.; Makani, S.; Tian, N.; Castillo, P. E.; Buchman, V. L.; et al. Aβγ-Synuclein Triple Knockout Mice Revealage-Dependent Neuronal Dysfunction. *Proc. Natl. Acad. Sci. U. S. A.* **2010**, *107* (45), 19573–19578. https://doi.org/10.1073/pnas.1005005107.

(14) Burré, J.; Sharma, M.; Tsetsenis, T.; Buchman, V.; Etherton, M. R.; Südhof, T. C. Alpha-Synuclein Promotes SNARE-Complex Assembly in Vivo and in Vitro. *Science* **2010**, *329* (5999), 1663–1667. https://doi.org/10.1126/science.1195227.

(15) Watson, J. B.; Hatami, A.; David, H.; Masliah, E.; Roberts, K.; Evans, C. E.; Levine, M. S. Alterations in Corticostriatal Synaptic Plasticity in Mice Overexpressing Human α-Synuclein. *Neuroscience* **2009**, *159* (2), 501–513. https://doi.org/10.1016/j.neuroscience.2009.01.021.

(16) Liu, S.; Ninan, I.; Antonova, I.; Battaglia, F.; Trinchese, F.; Narasanna, A.; Kolodilov, N.; Dauer, W.; Hawkins, R. D.; Arancio, O. α-Synuclein Produces a Long-Lasting Increase in Neurotransmitter Release. *EMBO J.* **2004**, *23* (22), 4506–4516. https://doi.org/10.1038/sj.emboj.7600451.

(17) Gureviciene, I.; Gurevicius, K.; Tanila, H. Role of α-Synuclein in Synaptic Glutamate Release. *Neurobiol. Dis.* **2007**, *28* (1), 83–89. https://doi.org/10.1016/j.nbd.2007.06.016.

(18) Gureviciene, I.; Gurevicius, K.; Tanila, H. Aging and α-Synuclein Affect Synaptic Plasticity in the Dentate Gyrus. *J. Neural Transm.* **2009**, *116* (1), 13–22. https://doi.org/10.1007/s00702-008-0149-x.

(19) Nemani, V. M.; Lu, W.; Berge, V.; Nakamura, K.; Onoa, B.; Lee, M. K.; Chaudhry, F. A.; Nicoll, R. A.; Edwards, R. H. Increased Expression of α-Synuclein Reduces Neurotransmitter Release by Inhibiting Synaptic Vesicle Reclustering after Endocytosis. *Neuron* **2010**, *65* (1), 66–79. https://doi.org/10.1016/j.neuron.2009.12.023.

(20) Wu, N.; Joshi, P. R.; Cepeda, C.; Masliah, E.; Levine, M. S. Alpha-Synuclein Overexpression in Mice Alters Synaptic Communication in the Corticostriatal Pathway. *J. Neurosci. Res.* **2010**, *88* (8), 1764–1776. https://doi.org/10.1002/jnr.22327.

(21) Larsen, K. E.; Schmitz, Y.; Troyer, M. D.; Mosharov, E.; Dietrich, P.; Quazi, A. Z.; Savalle, M.; Nemani, V.; Chaudhry, F. A.; Edwards, R. H.; et al. α-Synuclein Overexpression in PC12 and Chromaffin Cells Impairs Catecholamine Release by

Interfering with a Late Step in Exocytosis. *J. Neurosci.* **2006**, *26* (46), 11915–11922. https://doi.org/10.1523/JNEUROSCI.3821-06.2006.

(22) Cabin, D. E.; Shimazu, K.; Murphy, D.; Cole, N. B.; Gottschalk, W.; McIlwain, K. L.; Orrison, B.; Chen, A.; Ellis, C. E.; Paylor, R.; et al. Synaptic Vesicle Depletion Correlates with Attenuated Synaptic Responses to Prolonged Repetitive Stimulation in Mice Lacking α-Synuclein. *J. Neurosci.* **2002**, *22* (20), 8797–8807. https://doi.org/10.1523/jneurosci.22-20-08797.2002.

(23) Abeliovich, A.; Schmitz, Y.; Fariñas, I.; Choi-Lundberg, D.; Ho, W. H.; Castillo, P. E.; Shinsky, N.; Garcia Verdugo, J. M.; Armanini, M.; Ryan, A.; et al. Mice Lacking α-Synuclein Display Functional Deficits in the Nigrostriatal Dopamine System. *Neuron* **2000**, *25* (1), 239–252. https://doi.org/10.1016/S0896-6273(00)80886-7.

(24) Murphy, D. D.; Rueter, S. M.; Trojanowski, J. Q.; Lee, V. M. Y. Synucleins Are Developmentally Expressed, and α-Synuclein Regulates the Size of the Presynaptic Vesicular Pool in Primary Hippocampal Neurons. *J. Neurosci.* **2000**, *20* (9), 3214–3220. https://doi.org/10.1523/jneurosci.20-09-03214.2000.

(25) Gaugler, M. N.; Genc, O.; Bobela, W.; Mohanna, S.; Ardah, M. T.; El-Agnaf, O. M.; Cantoni, M.; Bensadoun, J. C.; Schneggenburger, R.; Knott, G. W.; et al. Nigrostriatal Overabundance of α-Synuclein Leads to Decreased Vesicle Density and Deficits in Dopamine Release That Correlate with Reduced Motor Activity. *Acta Neuropathol.* **2012**, *123* (5), 653–669. https://doi.org/10.1007/s00401-012-0963-y.

(26) Lundblad, M.; Decressac, M.; Mattsson, B.; Björklund, A. Impaired Neurotransmission Caused by Overexpression of α-Synuclein in Nigral Dopamine Neurons. *Proc. Natl. Acad. Sci. U. S. A.* **2012**, *109* (9), 3213–3219. https://doi.org/10.1073/pnas.1200575109.

(27) Vargas, K. J.; Schrod, N.; Davis, T.; Fernandez-Busnadiego, R.; Taguchi, Y. V.; Laugks, U.; Lucic, V.; Chandra, S. S. Synucleins Have Multiple Effects on Presynaptic Architecture. *Cell Rep.* **2017**, *18* (1), 161–173. https://doi.org/10.1016/j.celrep.2016.12.023.

(28) Clayton, D. F.; George, J. M. Synucleins in Synaptic Plasticity and Neurodegenerative Disorders. *J. Neurosci. Res.* **1999**, *58* (1), 120–129. https://doi.org/10.1002/(SICI)1097-4547(19991001)58:1<120::AID-JNR12>3.0.CO;2-E.

(29) Mehra, S.; Sahay, S.; Maji, S. K. α-Synuclein Misfolding and Aggregation: Implications in Parkinson's Disease Pathogenesis. *Biochim. Biophys. Acta - Proteins Proteomics* **2019**, *1867* (10), 890–908. https://doi.org/10.1016/j.bbapap.2019.03.001.

(30) Rizo, J.; Rosenmund, C. Synaptic Vesicle Fusion. *Nat. Struct. Mol. Biol.* **2008**, *15* (7), 665–674. https://doi.org/10.1038/nsmb.1450.

(31) Südhof, T. C. The Synaptic Vesicle Cycle. *Annu. Rev. Neurosci.* **2004**, *27* (1), 509–547. https://doi.org/10.1146/annurev.neuro.26.041002.131412.

(32) Südhof, T. C. The Presynaptic Active Zone. *Neuron* **2012**, *75* (1), 11–25. https://doi.org/10.1016/j.neuron.2012.06.012.

(33) Denker, A.; Rizzoli, S. O. Synaptic Vesicle Pools: An Update. *Front. Synaptic Neurosci.* 2010, 2, 135. https://doi.org/10.3389/fnsyn.2010.00135.

(34) Chanaday, N. L.; Cousin, M. A.; Milosevic, I.; Watanabe, S.; Morgan, J. R. The Synaptic Vesicle Cycle Revisited: New Insights into the Modes and Mechanisms. In *Journal of Neuroscience*; Society for Neuroscience, 2019; Vol. 39, pp 8209–8216. https://doi.org/10.1523/JNEUROSCI.1158-19.2019.

(35) Takamori, S.; Holt, M.; Stenius, K.; Lemke, E. A.; Grønborg, M.; Riedel, D.; Urlaub, H.; Schenck, S.; Brügger, B.; Ringler, P.; et al. Molecular Anatomy of a Trafficking Organelle. *Cell* **2006**, *127* (4), 831–846. https://doi.org/10.1016/j.cell.2006.10.030.

(36) Zaltieri, M.; Grigoletto, J.; Longhena, F.; Navarria, L.; Favero, G.; Castrezzati, S.; Colivicchi, M. A.; Corte, L. Della; Rezzani, R.; Pizzi, M.; et al. α-Synuclein and Synapsin III Cooperatively Regulate Synaptic Function in Dopamine Neurons. *J. Cell Sci.* **2015**, *128* (13), 2231–2243. https://doi.org/10.1242/jcs.157867.

(37) Yu, S.; Zuo, X.; Li, Y.; Zhang, C.; Zhou, M.; Zhang, Y. A.; Uéda, K.; Chan, P. Inhibition of Tyrosine Hydroxylase Expression in α-Synuclein- Transfected Dopaminergic Neuronal Cells. *Neurosci. Lett.* **2004**, *367* (1), 34–39. https://doi.org/10.1016/j.neulet.2004.05.118.

(38) Chen, R. H. C.; Wislet-Gendebien, S.; Samuel, F.; Visanji, N. P.; Zhang, G.; Marsilio, D.; Langman, T.; Fraser, P. E.; Tandon, A. α-Synuclein Membrane Association Is Regulated by the Rab3a Recycling Machinery and Presynaptic Activity. *J. Biol. Chem.* **2013**, *288* (11), 7438–7449. https://doi.org/10.1074/jbc.M112.439497.

(39) Swant, J.; Goodwin, J. S.; North, A.; Ali, A. A.; Gamble-George, J.; Chirwa, S.; Khoshbouei, H. α-Synuclein Stimulates a Dopamine Transporter-Dependent Chloride Current and Modulates the Activity of the Transporter. *J. Biol. Chem.* **2011**, *286* (51), 43933–43943. https://doi.org/10.1074/jbc.M111.241232.

(40) Butler, B.; Saha, K.; Rana, T.; Becker, J. P.; Sambo, D.; Davari, P.; Goodwin, J. S.; Khoshbouei, H. Dopamine Transporter Activity Is Modulated by α-Synuclein. *J. Biol. Chem.* **2015**, *290* (49), 29542–29554. https://doi.org/10.1074/jbc.M115.691592.

(41) Wersinger, C.; Rusnak, M.; Sidhu, A. Modulation of the Trafficking of the Human Serotonin Transporter by Human Alpha-Synuclein. *Eur. J. Neurosci.* **2006**, *24* (1), 55–64. https://doi.org/10.1111/j.1460-9568.2006.04900.x.

(42) Williams, J. K.; Yang, X.; Baum, J. Interactions between the Intrinsically Disordered Proteins β-Synuclein and α-Synuclein. *Proteomics* **2018**, *18* (21–22), 1800109. https://doi.org/10.1002/pmic.201800109.

(43) Surgucheva, I.; Sharov, V. S.; Surguchov, A. γ-Synuclein: Seeding of α-Synuclein Aggregation and Transmission between Cells. *Biochemistry* **2012**, *51* (23), 4743–4754. https://doi.org/10.1021/bi300478w.

(44) Antonny, B. Mechanisms of Membrane Curvature Sensing. *Annu. Rev. Biochem.* **2011**, *80* (1), 101–123. https://doi.org/10.1146/annurev-biochem-052809-155121.

(45) Middleton, E. R.; Rhoades, E. Effects of Curvature and Composition on α-Synuclein Binding to Lipid Vesicles. *Biophys. J.* **2010**, *99* (7), 2279–2288. https://doi.org/10.1016/j.bpj.2010.07.056.

(46) Pranke, I. M.; Morello, V.; Bigay, J.; Gibson, K.; Verbavatz, J. M.; Antonny, B.; Jackson, C. L. α-Synuclein and ALPS Motifs Are Membrane Curvature Sensors Whose Contrasting Chemistry Mediates Selective Vesicle Binding. *J. Cell Biol.* **2011**, *194* (1), 89–103. https://doi.org/10.1083/jcb.201011118.

(47) Harayama, T.; Riezman, H. Understanding the Diversity of Membrane Lipid Composition. *Nat. Rev. Mol. Cell Biol.* **2018**, *19*, 281–296. https://doi.org/10.1038/nrm.2017.138.

(48) Budzinski, K. L.; Allen, R. W.; Fujimoto, B. S.; Kensel-Hammes, P.; Belnap, D. M.; Bajjalieh, S. M.; Chiu, D. T. Large Structural Change in Isolated Synaptic Vesicles upon Loading with Neurotransmitter. *Biophys. J.* **2009**. https://doi.org/10.1016/j.bpj.2009.08.032.

(49) Jo, E.; McLaurin, J. A.; Yip, C. M.; St. George-Hyslop, P.; Fraser, P. E. α-Synuclein Membrane Interactions and Lipid Specificity. *J. Biol. Chem.* **2000**, *275* (44), 34328–34334. https://doi.org/10.1074/jbc.M004345200.

(50) Hellstrand, E.; Grey, M.; Ainalem, M.-L.; Ankner, J.; Forsyth, V. T.; Fragneto, G.; Haertlein, M.; Dauvergne, M.-T.; Nilsson, H.; Brundin, P.; et al. Adsorption of α-Synuclein to Supported Lipid Bilayers: Positioning and Role of Electrostatics. *ACS Chem. Neurosci.* **2013**, *4* (10), 1339–1351. https://doi.org/10.1021/cn400066t.

(51) O'Leary, E. I.; Jiang, Z.; Strub, M. P.; Lee, J. C. Effects of Phosphatidylcholine Membrane Fluidity on the Conformation and Aggregation of N-Terminally Acetylated α-Synuclein. *J. Biol. Chem.* **2018**, *293* (28), 11195–11205. https://doi.org/10.1074/jbc.RA118.002780.

(52) Fusco, G.; De Simone, A.; Gopinath, T.; Vostrikov, V.; Vendruscolo, M.; Dobson, C. M.; Veglia, G. Direct Observation of the Three Regions in α-Synuclein That Determine Its Membrane-Bound Behaviour. *Nat. Commun.* **2014**, *5* (1), 1–8. https://doi.org/10.1038/ncomms4827.

(53) Lee, S. J.; Jeon, H.; Kandror, K. V. α-Synuclein Is Localized in a Subpopulation of Rat Brain Synaptic Vesicles. *Acta Neurobiol. Exp. (Wars).* **2008**, *68* (4), 509–515.

CHAPTER 2.

DEVELOPMENT AND APPLICATION OF A NOVEL BIOPHYSICAL PLATFORM TO PROBE MEMBRANE BINDING OF α-SYNUCLEIN: SPHERICAL SILICA NANOPARTICLE-SUPPORTED LIPID BILAYERS (SSLBs)

2.1. Overview: SSLBs as a membrane curvature-enforced model membrane system to examine α-Synuclein binding

The overall motivation behind the design and development of spherical silica nanoparticle-supported lipid bilayers (SSLBs) for αS-membrane interactions was two-fold: (1) probing high-resolution details of αS membrane binding as a function of curvature and composition could uncover new insights into the membrane selectivity of αS, an important question from a membrane biophysics point of view, and (2) examining how αS membrane adsorption modifies colloidal interactions *between* 3-D membrane surfaces — which would normally be a difficult measurement for conventionally prepared LUVs, as explained in this section — could offer clues as to how membrane bound αS mediate attraction or repulsion of apposing membrane surfaces, in order to initiate useful biological function. Understanding the sensitive biophysical parameters for αS interactions with the membrane and its modification of membrane-membrane interactions can help reveal its physiological function associated with synaptic vesicles condensation, release from the pools, fusion with the neuronal membrane, and recycling back to the pools.[1–4]

The first objective mentioned above, αS membrane binding as a function of curvature, cannot be accomplished using unilamellar vesicles in a 10 – 100 nm diameter regime; the reason being that the polydispersity in size (and also in shape) below 100 nm is an inherent feature of vesicles resulting from their “soft” nature and the conventional

freeze-thaw-extrusion method that cannot tightly control for membrane curvature. Fig. 2.1 shows an example of typical LUV preparation that produced vesicles with an average diameter of 120 nm and a polydispersity index of 9%, corresponding to a standard deviation of ~36 nm assuming a Gaussian distribution.[5] It follows that for independently prepared LUV populations whose average diameter values differ by only tens of nanometers, their diameter distributions would significantly overlap and as a consequence, such size polydispersity prohibits measurements that *precisely* distinguish binding affinities resulting from small differences in membrane curvature — e.g., a difference of 20 – 30 nm in average LUV diameter which can still result in a considerable change in αS binding affinity.[6]

Beyond the issue of polydispersity (and thus controlling for their curvature) conventional LUVs are subject to limited characterization when it comes to probing membrane-membrane interactions. Addressing the question of intermembrane interactions is important for αS in the biological context of how it might regulate clustering of synaptic vesicles and/or affect the fusion of synaptic vesicles in concert with the SNARE complex[1] as referenced in the previous chapter. Measuring the interaction potential of one membrane with another is generally difficult due to the low electronic contrast of LUVs and necessitates the use of extraneous fluorescent probes, spin labeling, NMR or neutron techniques. SSLBs are by definition a supported lipid bilayer model system coated on silica nanoparticles, and owing to the nanoparticle core of SSLBs, their monodispersity, and the increased X-ray scattering cross section of the membranes, SSLBs enable small angle X-ray scattering experiments previously unrealizable with LUVs. With the use of SSLBs, the experiments that probe the forces involved in αS

mediated membrane-membrane interactions, and detailed structure-property relationships are made possible, as explained in chapters 3 and 4.

Therefore, SSLBs have been deliberately designed and created as a novel model system to characterize and gain new insights into αS-membrane interactions, but the development of this system to be as robust and tunable as possible presented a scientific problem in and of itself.

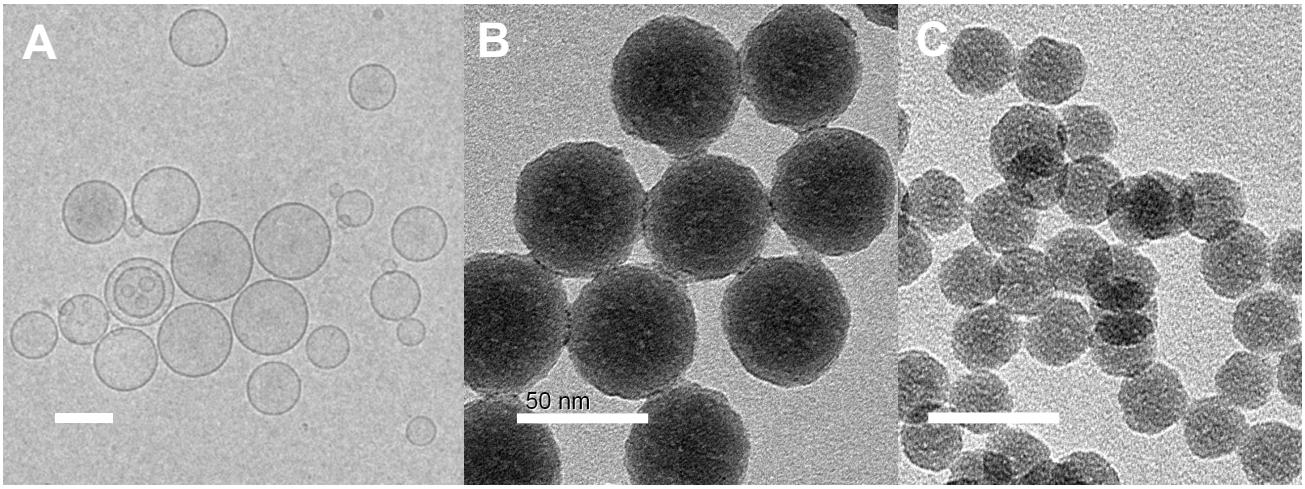

Fig. 2.1. Self-assembled lipid vesicles, unlike chemically synthesized nanoparticles, cannot be well-controlled for curvature.
(A). Polydisperse nature of LUVs with DLS-reported <diameter> = 120 nm and PDI = 0.09, as revealed by cryo-electron micrograph. PDI of 10-20% is typical for extruded LUVs. Note the inhomogeneity in both size and shape. Adapted from ref. (5).
(B-C). On the other hand, silica nanoparticles imaged under TEM are much more monodisperse; shown are 50 nm spherical silica nanoparticles (B), and 25 nm particles (C) obtained from HiQ-Nano (Arnesano, Lecce, Italy) and imaged in-house. Scale bar: 50 nm.

2.1.1. Supported lipid bilayer model system on three-dimensional nanoparticle substrates: current challenges and applications

We first addressed the problem of LUV polydispersity by considering silica nanoparticles, which are compatible with lipid adsorption, and with polydispersity that can be much more precisely tuned. Modern synthetic nanoparticle chemistry permits PDI

for silica nanoparticles to be as low as 1%,[7–10] and if lipid membranes can be forced to assemble as a single lipid bilayer on nanoparticle substrates, we would have a three-dimensional SLB model system that is receptive to ensemble binding measurements (Fig. 2.2).

The membrane biophysics field has found widespread use in two-dimensional SLB as a model system, mimicking the phospholipid bilayer and essentially immobilizing a membrane on a surface, making possible a wide array of optical, fluorescence, atomic force microscopies and spectroscopic techniques such as surface plasmon resonance to monitor protein binding.[11,12] Making a 2-D SLB system is typically achieved by spontaneously rupturing LUVs on the substrate of interest, which is easily done if the surface is sufficiently hydrophilic and readily interacts with the lipid membrane. When the adhesion energy between LUVs and flat substrate surface is sufficient[13] (on the order of 1 mJ/m^2), such interaction favors LUVs to make as much surface contact as possible and eventually rupture on the substrate forming bilayer "patches," or in the case of sufficient vesicle coverage, a fully covered single lipid bilayer. In the limit of weak surface interaction, the LUVs do not adhere to the substrate at all, while at the intermediate interaction regime, LUVs adsorb but not rupture, forming deflated yet intact lipid vesicles on the surface — a morphology that prohibits meaningful protein-lipid experiments.

As opposed to their 2-D counterparts, SLBs on *three-dimensional* substrates have not gained much interest, due in part to the challenges associated with forming a single lipid bilayer on highly curved substrates. A series of first studies to create and characterize 3-D SLBs by Bayerl et al. in the 1990's focused on forming a single DMPC bilayer on spherical glass beads with diameters between 0.3 and 10 μm.[14] These samples were prepared from a direct incubation of sonicated SUVs with the cleaned glass beads at

~60 °C. Notably, proton NMR measurements suggested a single lipid bilayer that makes contact with the bead across an interstitial water layer calculated to be 17 ± 5 Å thick.[14] The evidence for a single lipid bilayer assembly and existence of a water layer suggested that SLBs on glass beads can be used as a model system to examine the structure and dynamics of lipids forced on a curved substrate, and in addition, prompted further studies that examined the parameter space of possible lipid compositions and substrate curvatures for SLB on 3-D substrates.

Because the importance of membrane curvature and topology has been implicated in many membrane-related biological processes (vesicle fusion, endo-/exocytosis, protein localization, trafficking, signaling), the 3-D SLBs have been viewed as a promising tool for examining curvature sensing protein-lipid interactions. DMPC SSLBs were validated as a tool to calculate insertion depths of bacterial SpoVM peptide as a function of membrane curvature, using NMR techniques.[15] However, not many studies have documented the use of SSLBs for protein/peptide experiments, as there has been a clear limitation in compositions possible for SSLBs.

The most difficult challenge to SLB formation for many lipid compositions turned out to be the energy barrier required to sufficiently *bend* the lipid vesicles adsorbed on curved surface so that they rupture and form a contiguous single lipid bilayer. For instance, the cryo-TEM imaging of SSLBs on ~100 nm silica nanoparticles showed that lipid compositions that included > 20 mol% anionic lipids did not create a single lipid bilayer morphology but resulted in unruptured vesicles adhered on nanoparticles.[16] Expanding the possible substrate curvature and lipid compositions can drastically increase the potential of SSLBs for applications spanning protein-lipid interactions and drug delivery. This is important for αS experiments since the protein interacts with

synaptic vesicles which are highly curved (40 nm in average diameter) and whose composition possibly includes > 30 mol% anionic lipids.[17]

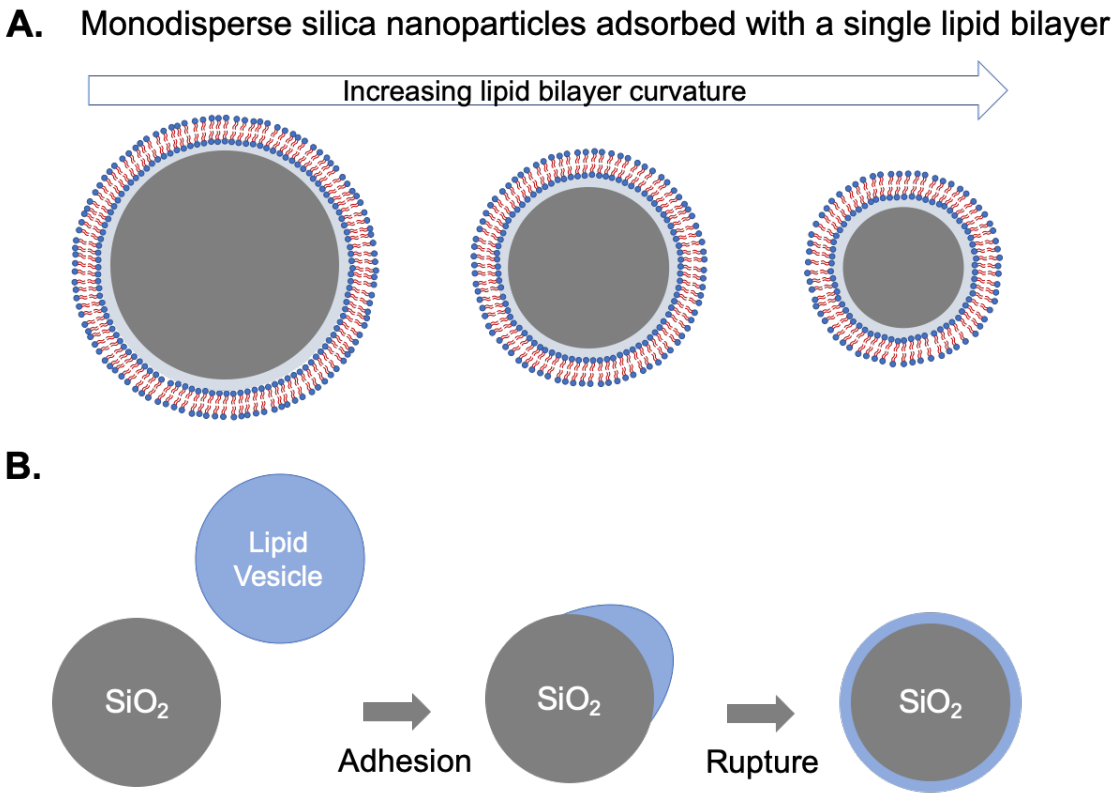

Fig. 2.2. The design and development of spherical silica nanoparticle-supported lipid bilayer (SSLB) model system.
(A). A schematic of membrane curvature-enforced model system that can be created when lipids are able to adsorb and assemble as a single lipid bilayer on SiO_2 particles of multiple curvatures. A 1-2 nm interstitial water layer exists between the inner membrane leaflet nanoparticle surface.[14,15]
(B). Any robust strategy to creating SSLBs must take into account both adhesion and rupture steps of particle-vesicle interaction. We modify nanoparticle surface chemistry and accumulation of internal osmotic pressure within particle-adsorbed vesicles to promote SSLB formation.

Its application to study protein-lipid interactions counts as just one of the important potential applications of SSLB development. From a nanomedicine and drug delivery perspective, the development of SSLBs offers distinct advantages associated with

biocompatibility and cell uptake. The lipid-coated nanoparticle presents a biocompatible surface that can be easily taken up by natural endocytic mechanisms if the particle is small enough,[18,19] while nanoparticles can be loaded with drugs and/or molecules of interest that need cell internalization.[20] The lipids coated around nanoparticles can be conjugated with specific biochemical entities that can direct lipid-particle-drug complex to certain cells.[20,21] If small nanoparticles can load highly charged lipid compositions, it would serve to increase drug delivery efficiency, reducing the barrier of SSLB usage in biotechnological applications. But again, the development of SSLBs as complex delivery vehicles is predicated on being able to form the very sample with suitable lipids and particles.

2.1.2. Development of a simple and effective method for SSLB formation using an osmotic pressure approach

The general approach described in this chapter resolves the issues described above. We first considered the two-step physical mechanism by which a lipid bilayer forms on nanoparticle substrates: vesicle adsorption and rupture (Fig. 2.2). Such mechanism has been well-documented and studied for 2-D surfaces. The mechanism essentially implicates an energetic balance between attractive particle-vesicle adhesion and unfavorable vesicle bending associated with deflation and eventual rupture on high-curvature substrates.[13]

The first mechanistic step can be straightforwardly tuned with surface chemistry and electrostatics, as oppositely charged vesicles and particles experience greater adhesion. The wetting properties of the surface cannot be altered unless particle identity is changed. Controlling the second step required more thought; the vesicle upon

nanoparticle adsorption experiences a buildup of some internal osmotic pressure due to a loss of volume from contact with the particle. If the pressure buildup reaches some critical threshold the rupture can possibly occur. We then considered the question of how the internal pressure buildup can be experimentally amplified. Work has to be externally applied to all vesicles in a consistent and controlled manner that does not drastically compromise vesicle integrity. The physically motivated approach we chose was that: p-V work can be applied from a concentration difference of solutes inside and outside of the vesicle. If within the vesicle lumen there are trapped osmolytes, there would be a net influx of water (transmembrane permeability of water is on the order of seconds) and the pressure would drive defect formation and rupture of adhered vesicles.

Of course, there may be more chemically driven approaches to SSLB formation, using "solvent-assisted" approaches where organic solvent solubilizing lipids is progressively replaced with aqueous media[22,23] or chemically linking the inner leaflet to the substrate surface; however, forming the vesicles first in an aqueous environ and self-assembling them on substrate may give the closest mimic of a phospholipid bilayer.

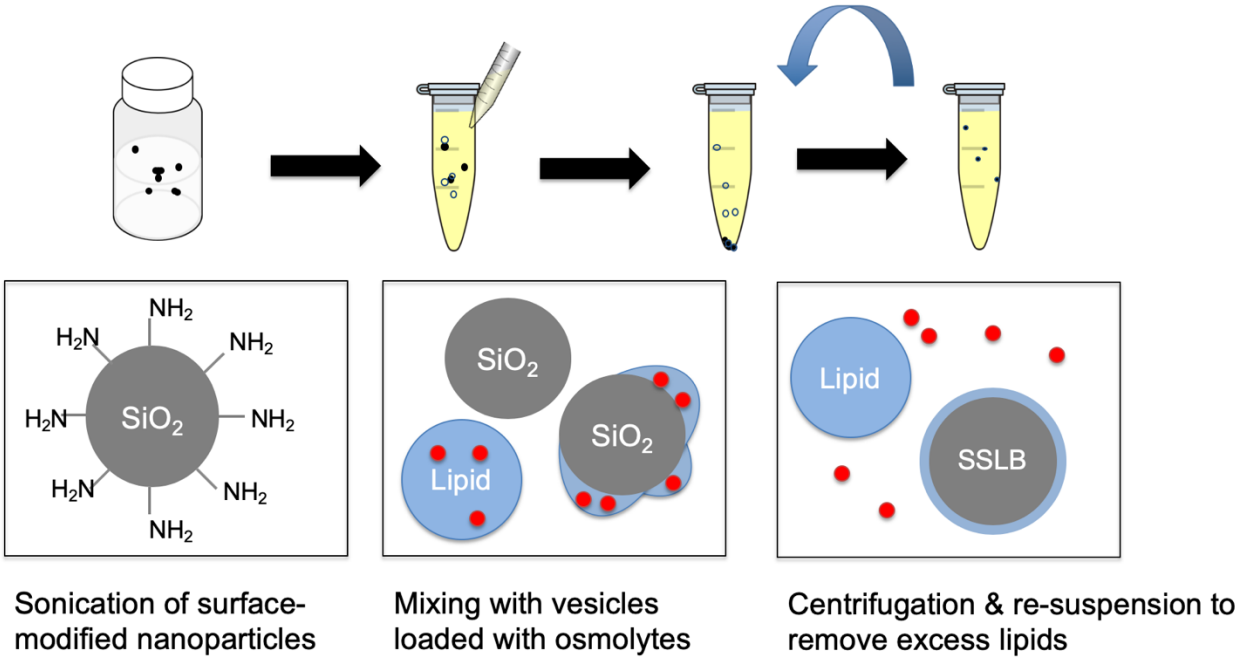

Fig. 2.3. The experimental steps of SSLB formation that results from driven adhesion and rupture of vesicles on nanoparticle substrates.
First we alter the nanoparticle surface chemistry such that nanoparticles and vesicles have oppositely charged surfaces, *e.g.* modifying the particle surface with positively charged amine groups to enhance surface contact with negatively charged vesicles with high DOPA or DOPS content. Then we load the vesicles with some amount of osmolyte (sucrose or glycerol) such that when mixed with nanoparticle solution with lower osmolarity, vesicles experience transmembrane hypoosmotic gradient, effectively lowering the bending modulus of vesicles to engulf the adsorbed nanoparticle. Excess lipids and osmolytes can be washed out by centrifugation-resuspension cycles. SSLB production is straightforward once optimal buffer conditions are met, easily scalable, and buffer exchangeable – enabling new ensemble measurements for protein-lipid interactions.

2.2. Materials and methods

2.2.1. Materials

All lipids were purchased in highest purity available powder form from Avanti Polar Lipids (Alabaster, AL, USA). The lipids used for this dissertation work were: DOPC, DOPA, DOPS, DOTAP, DOPE, and Chol (derived from ovine wool, with > 98% reported purity as confirmed by thin layer chromatography, HPLC, and mass spectrometry). HPLC-grade chloroform, methanol, and denatured ethanol solutions, needed for lipid

solubilization and preparation, were purchased from Fisher Scientific (Hampton, NH, USA).

The following aqueous buffer components were purchased from MilliporeSigma (Burlington, MA, USA): HEPES, HEPES sodium salt, citric acid, sodium citrate dihydrate, sodium chloride, glycerol, and sucrose. Concentrated stock solutions of 10X "HB7" buffer (100 mM HEPES, 1000 mM NaCl dissolved in MilliQ water, adjusted to pH 7.0) and 5X "CBS" buffer (50 mM citrate, 750 mM NaCl at pH 6.0) were prepared and diluted and/or mixed as necessary for SSLB experiments. In addition, 2 M stock solutions of glycerol and sucrose were separately prepared and mixed with stock salt solutions as necessary.

Monodisperse spherical silica nanoparticles with either silanol or amine functionalized surface were purchased from two sources: HiQ-Nano (Arnesano, Lecce, Italy) for 40 nm and 50 nm-diameter particles and Nanocomposix (San Diego, CA, USA) for 60 nm-diameter particles. Silica nanoparticles with silanol surface were purchased in ultrapure water, while amine-modified surface nanoparticles were purchased and stored in ethanol, in order to prevent amine groups from slowly deprotonating in water — and thereby preventing change in the overall surface charge. Dialysis cassettes (3.5k MWCO Slide-A-Lyzer) were purchased from Fisher Scientific in order to dialyze out ethanol into MilliQ water for the amine-modified nanoparticles. The particles were typically purchased at a concentration of ~10 mg/mL, whose exact value was reported by the manufacturer via gravimetric analysis.

2.2.2. Preparation of large unilamellar vesicles (LUVs) via freeze-thaw extrusion

For all LUV preparations, the conventional freeze-thaw extrusion method was used, employing a Lipex extruder purchased from Evonik Transferra Nanosciences (Burnaby, BC, Canada). Lipids in suitable molar ratios were first solubilized in chloroform in a glass vial, after which the chloroform was completely evaporated by ultra-high-purity N_2 flow and the glass vial was vacuum dried overnight to remove all residual solvent. The pre-weighed glass vial containing dried lipids was weighed again to confirm lipid mass that had been calculated based on concentrations and volumes used to make the mixture. Lipid mixture was then hydrated in an aqueous buffer, 1X CBS added with some concentration of glycerol or sucrose depending on the lipid composition, as laid out in Tables 2.1–2.3. The glass vial was gently vortexed for 1 hour at 40°C to form multilamellar vesicles resulting from swelling and self-assembling of lipids in an aqueous medium. Five freeze-thaw cycles — done with dry ice-denatured ethanol bath and 40°C water bath, respectively — were applied to the glass vial in order to form unilamellar vesicles. The resulting unilamellar vesicles, polydisperse in size, were first extruded once through two 400 nm Whatman Nucleopore membranes at 50 psi of Ar and again extruded 15 times through two 80 nm membranes at 250 psi to produce LUVs with an average diameter of 83 nm. To produce LUVs with a 65 nm average diameter, a different combination of membranes and Ar pressure was used; polydisperse vesicles were first extruded once through two 200 nm membranes at 50 psi and then again extruded 15 times through two 50 nm membranes. Vesicle sizing was done through DLS with Malvern Zetasizer (Malvern, UK).

2.2.3. SSLB formation via a general osmotic stress method

SSLB formation occurred via spontaneous adsorption and rupture of large unilamellar vesicles on silica nanoparticle substrates. While the experimental process of making SSLBs was relatively simple, the buffer and salt conditions in which the LUVs and nanoparticles were mixed had a drastic impact on the resulting morphology of SSLBs. The preparation of SSLBs was done in three general steps outlined as follows:

a. Dialysis and dilution of concentrated nanoparticles

The silanol nanoparticles were obtained in ultrapure water, but the amine-modified silica nanoparticles were obtained in ethanol — for which the ethanol had to be first exchanged out to MilliQ water, as ethanol would solubilize lipids upon contact. Nanoparticle dialysis was performed in 1 L of MilliQ water at room temperature in a dialysis cassette for 14 hours. The 1 L water bath was replaced after 1 and 2 hours into dialysis. The nanoparticles in MilliQ water was diluted to 2 mg/mL particle concentration into 1X CBS buffer solution. The particles were subsequently bath sonicated for 15 minutes prior to mixing with LUVs.

b. Reaction of nanoparticles and LUVs

The aqueous nanoparticle solution in 1X CBS was mixed well with LUVs formed in 1X CBS with some amount of glycerol or sucrose, the exact amount of which is outlined in Tables 2.1–2.3. For a given particle curvature and lipid composition, the optimal glycerol or sucrose concentration that yields SSLBs was determined empirically. The concentration of LUVs was calculated such that the reaction between nanoparticles and LUVs occurs at a 3 vesicles-to-1 nanoparticle ratio. For instance, to create DOPC:DOPA (1:1 molar ratio) SSLBs on 60 nm nanoparticle substrates, LUVs of this specific

composition were formed at a concentration of 4.78 mM total lipid, in 1X CBS, 650 mM sucrose buffer. Equal volumes of 60 nm nanoparticle solution at 2 mg/mL and LUVs were mixed by pipetting them in an Eppendorf tube and incubated at 40°C for 1 hour to speed up the reaction between nanoparticles and LUVs. For 50 and 40 nm particles, lipid concentrations used were 8.75 mM, and 11.75 mM total lipid, respectively.

c. Purification of SSLBs via centrifugation and resuspension

Because the reaction between particles and LUVs took place in excess lipids, remaining lipids that did not adsorb on nanoparticles had to be removed from solution. Since SSLBs have a dense nanoparticle core and LUVs do not, the two can be separated by a simple centrifugation-resuspension protocol. The reaction mixture, after 1 hour of incubation, was centrifuged at 1700 *g* for 10 minutes, after which the supernatant was carefully removed and replaced with HB7 buffer. Pelleted SSLBs were resuspended in solution after a thorough mixing. Three cycles of centrifugation-resuspension were performed to remove as much excess lipids as possible. A total of three cycles were optimal as applying more cycles incurred more sample loss.

2.2.4. Negative-stain and cryo-electron microscopy

The morphology of SSLBs were first characterized by negative-stain TEM in order to visually confirm a single lipid bilayer surrounding nanoparticle core and verify full surface coverage. A 1-2 μL of SSLB sample at 2 mg/mL silica concentration was deposited on plasma treated TEM grid coated with formvar/carbon film (Electron Microscopy Sciences, Hatfield, PA, USA). Sample was allowed to deposit on the grid for one minute, after which the sample droplet was wicked away with a filter paper. The grid was

subsequently negative stained with 2 μL of 1.66 wt/vol % ammonium molybdate solution for 30 seconds before wicking it away and fully drying the grid in air. The SSLB electron micrographs were taken using 120 kV FEI Spirit microscope.

For cryogenic TEM, the SSLB sample at 1 mg/mL silica concentration was plunge frozen in liquid ethane, using FEI Vitrobot. The frozen sample was stored in liquid nitrogen for two days to remove solid ethane that deposited on the grid. The cryo-electron micrographs were taken using 200 kV FEI Talos microscope. All TEM imaging was carried out at the Advanced Electron Microscopy facility at the University of Chicago.

2.2.5. Phosphate analysis

The exact concentration of lipids in each SSLB sample was assayed using a standard colorimetric phosphate analysis technique. A 10 μL of SSLB sample (at 2 mg/mL silica concentration) in a test tube was first digested in 10% (v/v) trace metal grade H_2SO_4 solution at 200°C for 1 hour. After all of the water evaporated, 20 μL of 30% (w/w) H_2O_2 solution was added, and the reaction was left to continue for another 40 minutes to fully oxidize all phosphorus atoms to PO_4^{3-}. Ammonium molybdate dissolved in aqueous ascorbic acid solution was added to form $PMo_{12}O_{40}^{7-}$ ions whose absorbance was measured at 820 nm. Measured absorbance was converted to concentration of phosphate using a linear standard curve made from 0.65 mM phosphorus standard solution (Sigma Aldrich). The absorbance measurements were made using Cary 5000 spectrophotometer at the University of Chicago MRSEC Material Properties Measurement Laboratory facility.

2.2.6. Colloidal characterization of LUVs and SSLBs

Dynamic light scattering and ζ-potential measurements were performed on a Malvern Zetasizer NanoZS at 1:50 (v:v) sample dilution in buffer or MilliQ water in disposable plastic cuvettes. The Zetasizer calculation settings were appropriately made to correct for solvent viscosity of buffers containing sucrose or glycerol since particle diffusion depends on the medium.

2.2.7. Expression and purification of αS

The physiologically found αS is the N-terminally acetylated form, which was purified and used for all binding experiments. The protocol was largely based on that reported,[24] and αS plasmid was the gracious gift of Tim Bartels (University College London). *Escherichia coli* BL21 cells were first transformed to include the pNatB plasmid encoding for an N-α-acetyltransferase. Then αS encoded onto a pET-21a backbone was transformed into BL21 cells. Cells were incubated in LB media at 37° C until optical density reached (OD_{600} = 0.6), and induced with 1 μM of isopropyl β-D-1-thiogalactopyranoside (IPTG) and then left to incubate for an additional 4 hours. Pelleted cells were resuspended in 25 mM Tris, 20 mM NaCl at pH 8.0 and lysed using a high-pressure homogenizer and subsequently boiled for 5 minutes. After pelleting cellular debris, supernatant was loaded into a 5 mL HiTrap Q FF column (GE Healthcare Lifesciences, Pittsburgh, PA, USA) and eluted by gradient to 1M NaCl using with 25 mM Tris, pH 8.0, 1M NaCl. Fractions containing N-terminal acetylated αS were pooled and concentrated using Amico Ultra-15 (Millipore-Sigma) concentrators and further purified

through a Superdex 200 10/300 column (GE Healthcare Lifesciences), with protein eluting at 14.5 mL in HB7 buffer. Protein concentration was measured via NanoDrop (Thermofisher Scientific) at predicted absorbance (A_{280} coefficient = 5960), aliquoted into one-use vials, and frozen by liquid nitrogen until further use.

2.2.8. Isothermal titration calorimetry (ITC)

The cell and syringe were washed for three times with built-in wash modules, and the reference cell was filled with MilliQ water. First, MilliQ water in syringe was titrated into the sample cell of MillQ water to check cleanliness of system and stability of baseline; water titrated into water should result in negligible exothermic heat across all titrations and the baseline heat supply should stay constant. For the actual experiment, the 200 μL sample cell was filled with SSLBs in HB7, typically containing 3 – 4 mM of lipids. The 40 μL syringe was filled with αS in HB7 at a concentration of ~100 μM which depended on the production batch. The reference cell was filled with MilliQ water. One pre-injection of 0.4 μL and 19 injections of 2 μL SSLBs were made. The raw heat data were analyzed on the MicroCal ITC-Origin analysis software using “one-site” model to calculate binding parameters. All ITC measurements were made using MicroCal ITC 200 (GE Healthcare; Little Chalfont, Buckinghamshire, UK) at the Biophysics Core facility at the University of Chicago.

2.3. Osmotic loading of lipid vesicles drives SSLB formation for highly charged lipid compositions

Following our hypothesis of osmotic stress driven rupture of lipid vesicles on nanoparticles, we examined SSLB formation as a function of applied stress and particle curvature, for a range of lipid compositions previously thought to be unrealizable for creating SSLBs. Equimolar mixture of DOPC:DOPA (1:1), where the charge of DOPA molecule is close to –1.2 in pH 7,[25] was investigated as a first test to push the compositional boundary for highly anionic lipid mixture. After the vesicles were formed in 1X CBS buffer and mixed with 60 nm silanol-surface nanoparticles, and the resulting morphology was imaged under TEM, we found that vesicles barely adhered to nanoparticles irrespective of vesicle-to-particle ratio; the low amount of adhesion is attributable to charge-charge repulsion of particle and vesicle surfaces as silanol surface is slightly negatively charged in neutral pH.[13] On the other hand, the particles with amine-modified groups, which are positively charged and therefore attract the anionic vesicle surface, indeed increased adhesion but did not yield a single lipid bilayer morphology; intact vesicles were observed adhered to the surface, which highlighted the importance of driving rupture as highly charged membranes are more difficult to bend than zwitterionic ones.[26]

When we induced a hypoosmotic gradient to vesicles by simply mismatching the osmolyte concentration in buffers suspending vesicles and particles, we found a significantly different result. When vesicles were produced in 1X CBS and 650 mM sucrose, whose membrane permeability (~10^{-12} cm/s) is negligible on the timescale of experiment, and they were mixed in equal volume with particles suspended in 1X CBS solution without sucrose, the sucrose concentration within the vesicles presumably

remained at 650 mM, while its concentration outside of vesicles was roughly halved due to dilution — incurring a transmembrane mismatch of sucrose concentration and therefore subjecting the vesicles to hypoosmotic stress. With this protocol, we saw a near complete coverage of nanoparticles with a single lipid bilayer of DOPC:DOPA (1:1) under TEM (Fig. 2.4). Clearly a much different morphology resulted by a simple addition of sucrose in vesicle suspension buffer. When the number of lipids was quantitated in this sample by phosphate analysis, the experimentally obtained coverage was 83.1 ± 11% (average ± standard deviation from five independently prepared samples) of the expected number, showing a good agreement between experimental and expected values. The "expected" number is calculated by estimating a single lipid headgroup surface area to be 59 $Å^2$,[27] an aqueous layer between the nanoparticle surface and lipid bilayer to be 1 nm thick, and lipids to be close packed on a spherical shell, yielding 51,000 lipids for one 60 nm nanoparticle. The negative deviation from 100% coverage is likely due to some sample loss during the washing process and the back-of-the-envelope estimation of above physical parameters, but the visual evidence for complete coverage was clear with TEM images.

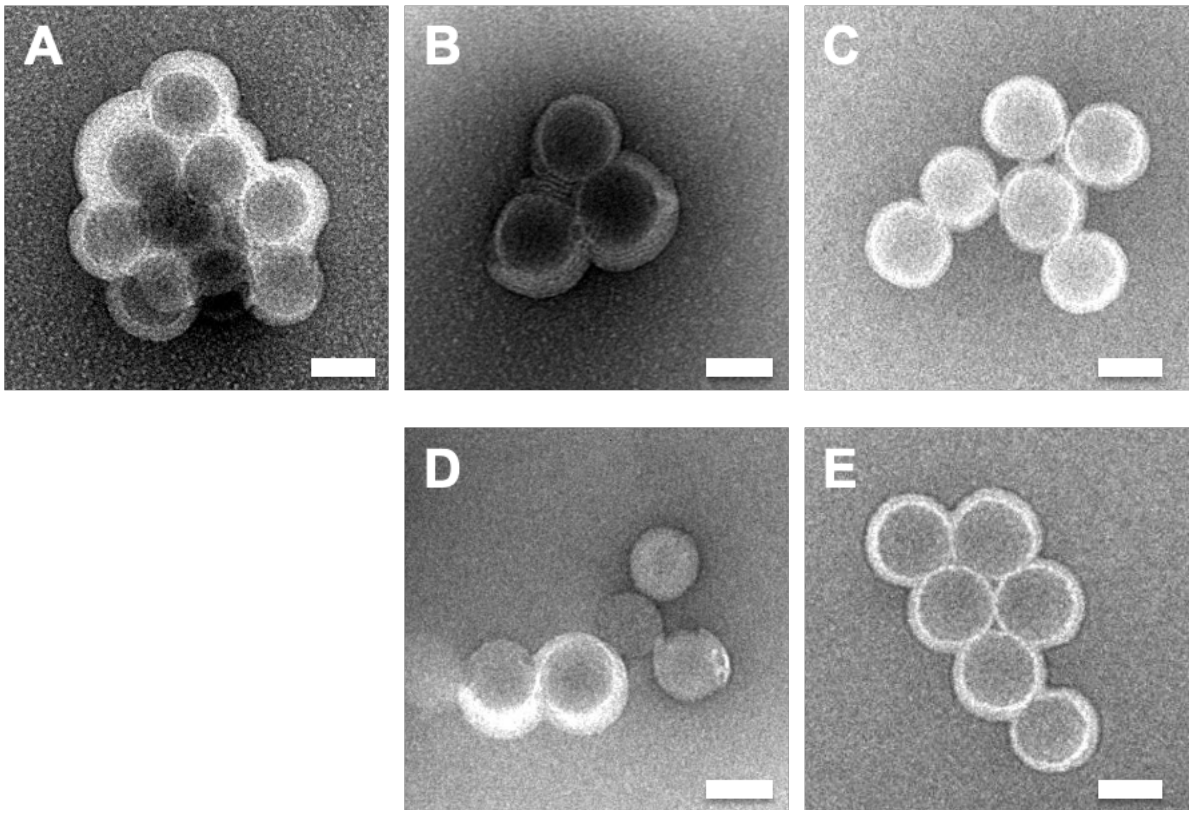

Fig. 2.4. Transmission electron microscopy reveals SSLB formation via an increase in osmotic pressure of highly-charged vesicles mixed with silica nanoparticles.
(A-C). Highly-charged SSLB formation was verified under TEM after incubating 60 nm amine-functionalized silica nanoparticles in CBS buffer (10 mM citrate pH 6.0, 150 mM NaCl) with highly-charged DOPC:DOPA (1:1, mol:mol) vesicles suspended in CBS (A), CBS and increasing sucrose concentrations, $\Delta C_{Sucrose}$ = 250 mM (B) and $\Delta C_{Sucrose}$ = 325 mM (C).
(D-E). To verify that SSLB formation was mediated via an osmotic gradient and not sucrose-specific effect, SSLB preparation was performed as before but with vesicles suspended in CBS and increasing glycerol concentrations, $\Delta C_{Glycerol}$ = 300 mM (D) and $\Delta C_{Glycerol}$ = 400 mM (E). Scale bar: 50 nm. Reproduced and caption adapted from ref. (28).

Further important details emerged about this process that reinforced the osmotic stress-driven formation hypothesis. First, when a different osmolyte glycerol was used, we saw an analogous result to addition of sucrose; at $\Delta C_{glycerol}$ = 300 mM, the desired SSLB formation occurred (Fig. 2.4D and 2.4E), showing that this formation occurred independently of the osmolyte identity. NaCl was also used as an osmolyte and gave a

similar result (data not shown here), but inclusion of high salts accelerated nonspecific colloidal aggregation of nanoparticles, an undesirable effect that discouraged the further use of salts as an osmolyte. Second, low concentrations of sucrose (or glycerol) did not yield SSLBs with good lipid coverage (Fig. 2.4B and 2.4D), which empirically depended on the concentration of osmolyte, or the degree of hypoosmotic stress subjected to vesicles. In other words, coverage of particles progressively increased with higher osmolyte concentration. Third, compared to the DOPC:DOPA (1:1) composition, the optimal osmolyte concentration for complete SSLB formation was similar for DOPC:DOPS (1:1), and also for DOPC:DOTAP (1:1), where DOPS carries a net negative charge and DOTAP carries a net positive charge, at neutral pH (Table 2.3). For these compositions, independent of charged lipid identity, the osmolyte induced SSLB formation happened at similar osmolyte concentrations, suggesting that membrane charge density is a primary determinant of the degree of hypoosmotic stress required to induce SSLB formation. Lastly, the optimal osmolyte concentration increased for higher particle curvature, which we interpret as greater stress is required to bend and rupture vesicles on higher curvature.

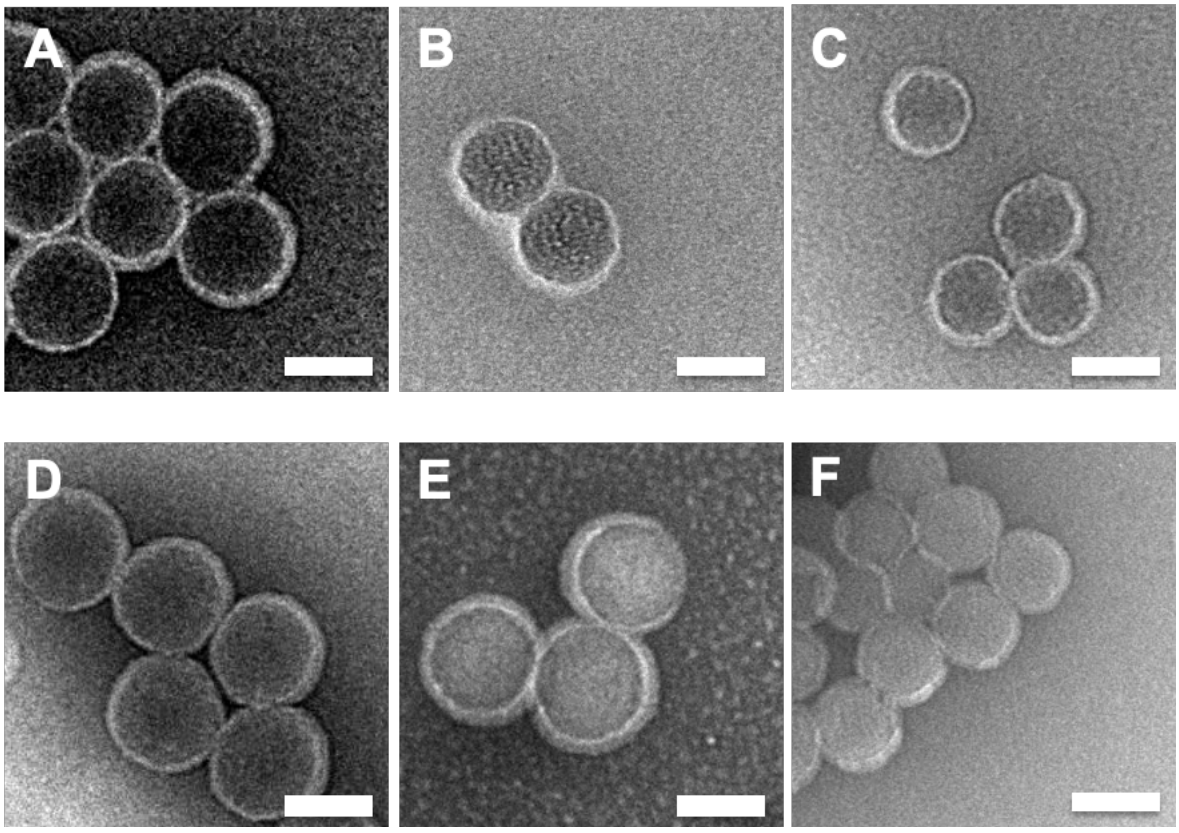

Fig. 2.5. SSLBs of various sizes can be obtained by modulating the osmotic gradient across donor vesicle membranes.
(A-C). Mixing highly-charged DOPC:DOPA (1:1) vesicles with 60 (A), 50 (B), and 40 nm (C) amine-functionalized silica nanoparticles yields SSLBs at optimal osmotic pressures (Table 2.2).
(D-F). replacing DOPA with another physiological anionic lipid, DOPS, also yields SSLBs when mixed with 60 (D), 50 (E), and 40 nm (F) amine-functionalized silica nanoparticles, suggesting that the SSLB formation via transmembrane osmotic gradient is independent of lipid identity. Scale Bar: 50 nm. Reproduced and caption adapted from ref (28).

The empirical findings explained above largely followed our intuition of osmolyte-induced, hypoosmotic stress driven rupture and formation of SSLBs. In particular, we note that an overall increase in vesicle charge — and therefore an increased electrostatic interaction between vesicle and particle surfaces — did *not* promote SSLB formation. This observation pointed to the high energy expenditure for rupture of highly charged membranes, and to the importance of considering a key membrane property, membrane

bending rigidity, rather than the strength of surface adhesion, for SSLB formation. In fact, when we included 14 mol% of 1-octanol in DOPC:DOPA lipid mixture, a cosurfactant well known to thin a lipid membrane and reduce its rigidity, the optimal concentration of sucrose needed decreased by more than three-fold (Fig. 2.6). This experiment further confirmed the importance of membrane bending rigidity for SSLB formation.

Finally, the validation needed to show that a *single* lipid bilayer had indeed formed on nanoparticles required using a technique that preserved the native structure of lipid membrane adsorbed on nanoparticle. The conventional negative-stain TEM requires that a sample be completely dried on TEM grid substrate prior to imaging it in the vacuum of an electron microscope, which can introduce difficult-to-interpret imaging artifacts for SSLB samples; for instance, one can expect that in the course of sample preparation the lipids possibly detach from nanoparticle substrate and dehydrate on the grid resulting in a significant perturbation of membrane morphology obfuscating the view of the membrane. By using cryo-TEM and freezing the sample in liquid ethane, we imaged the SSLBs in their solution state, a definitive high-resolution verification that the lipid morphology was indeed what we had looked for: a single lipid bilayer (Fig. 2.7). We thus confirmed that cryo-TEM images validated what we saw on negative stained images.

Overall, by introducing a transmembrane hypoosmotic stress resulting from a simple change in buffer conditions of vesicles, we were able to expand the parameter space of possible SSLB formation, corroborating the existing framework of chemical and physical principles involved in nanoparticle-vesicle interactions.

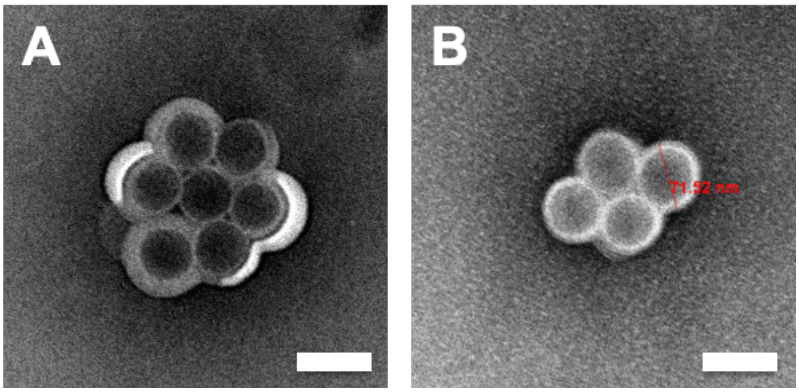

Fig. 2.6. Membrane softening through the addition of cosurfactants lowers the threshold for osmotic-shock driven SSLB formation.
As a validation of vesicle deformation being the primary driver behind SSLB formation, the transmembrane osmotic pressure required for vesicles containing at molar ratio 43:43:14 (DOPC:DOPA:1-octanol) was examined. (a), In the absence of a transmembrane osmotic gradient, DOPC:DOPA:1-octanol vesicles adhered to oppositely-charged amine-functionalized 60 nm nanoparticles without rupturing. (b). However, compared to the osmotic gradient required for DOPC:DOPA (1:1) SSLBs ($\Delta C_{sucrose}$ = 325 mM), complete SSLB formation is observed with DOPC:DOPA:1-octanol vesicles at a much lower osmotic pressure ($\Delta C_{Sucrose}$ = 100 mM). Scale bar: 50 nm. Reproduced and caption adapted from ref (28).

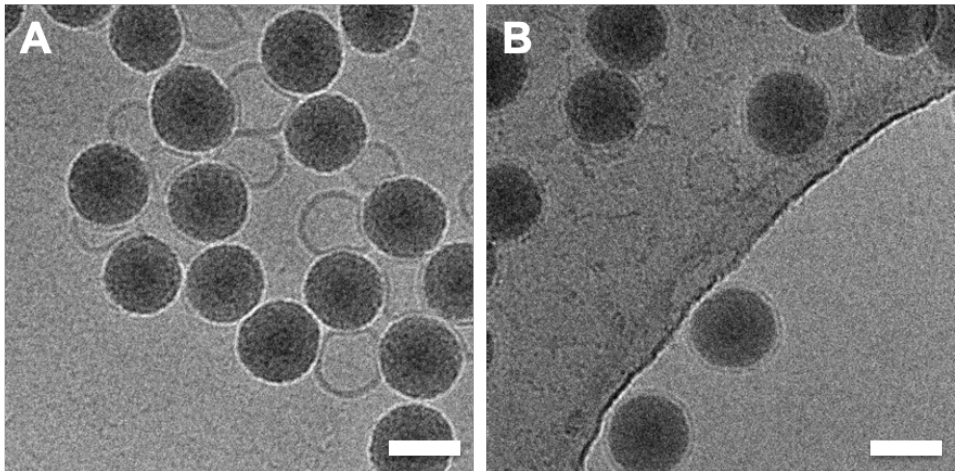

Fig. 2.7. Highly-charged SSLBs were confirmed via cryo-TEM.
To rule out artifacts from negative stain TEM, cryo-TEM was used to validate solution structures.
(A). Without osmotic gradient, highly-charged DOPC:DOPA (1:1) vesicles adhered to oppositely-charged particles without rupturing.
(B). In the presence of osmotic gradient ($\Delta C_{Sucrose}$ = 325 mM), SSLBs were formed with contiguous (i.e. defect-free) supported lipid bilayers around 60 nm amine-functionalized nanoparticles. Scale bar: 50 nm. Adapted from ref. (28).

Table 2.1. Osmolyte concentration required for DOPC/charged lipid SSLB formation with vesicles extruded through 80 nm pores and 60 nm spherical-nanoparticles (amine-functionalized for DOPA and DOPS samples; silanol-functionalized for DOTAP samples). Table and caption adapted from ref. (28).

Charged Lipid (Charge)	Charged Lipid [%]	$\Delta C_{Sucrose}$ [mM]	ζ-potential [mV]
DOPA (-1)	10	200	-16.7 ± .611
DOPS (-1)	10	200	-26.0 ± 1.79
DOTAP (+1)	10	200	+24.6 ± .924
DOPA	25	200	-20.8 ± .800
DOPS	25	200	-39.4 ± 4.34
DOTAP	25	200	+29.1 ± 1.15
DOPA	50	325	-45.1 ± 1.45
DOPS	50	300	-48.0 ± 1.88
DOTAP	50	300	+32.6 ± 1.27
DOPA	60	350	-51.4 ± 1.61

Table 2.2. Osmolyte Concentration required for 50% Charged Lipid/50% DOPC SSLB formation on amine-functionalized spherical-nanoparticles Table and caption adapted from ref.(28).

Charged Lipid	Nanoparticle Diameter [nm]	Osmolyte	$\Delta C_{Osmolyte}$ [mM]	Pore Size [nm]
DOPA	40	Sucrose	400	50
DOPA	50	Sucrose	350	80
DOPA	60	Sucrose	325	80
DOPA	60	Glycerol	400	80
DOPS	40	Sucrose	400	50
DOPS	50	Sucrose	350	80
DOPS	60	Sucrose	300	80

Table 2.3. Osmolyte Concentration required for Charged Lipid/DOPC SSLB formation with vesicles extruded through 80 nm pores and 60 nm spherical-nanoparticles (amine-functionalized for DOPA and DOPS samples; hydroxyl-functionalized for DOTAP samples) Table and caption adapted from ref. (28).

Charged Lipid (Charge)	Charged Lipid [%]	$\Delta C_{Sucrose}$ [mM]	ζ-potential [mV]	DLS Z-Avg. Diameter [nm][a]	DLS Number-Avg. Diameter [nm][a]
DOPA (-1)	10	200	-16.7 ± .611	203.3	133.3
DOPS (-1)	10	200	-26.0 ± 1.79	105.6	76.13
DOTAP (+1)	10	200	+24.6 ± .924	128.4	88.47
DOPA	25	200	-20.8 ± .800	194.2	131.6
DOPS	25	200	-39.4 ± 4.34	136.4	87.18
DOTAP	25	200	+29.1 ± 1.15	148.9	93.66
DOPA	50	325	-45.1 ± 1.45	181.1	115.3
DOPS	50	300	-48.0 ± 1.88	215.0	107.2
DOTAP	50	300	+32.6 ± 1.27	181.4	115.4
DOPA	60	350	-51.4 ± 1.61	159.3	96.25

[a]Discrepancies between DLS Z-average size/number-average size measurements with electron microscopy data is most likely due to nanoparticle size distributions (and thus, SSLB size distributions) not precisely following a normal distribution, with DLS Z-Avg. size overemphasizing scattering from larger particles (SSLBs) (See *e.g.*, ref. 29). As expected, the DLS Number-Avg. size is closer to the expected SSLB size from TEM measures (~70 nm).

2.4. Limitations in composition and colloidal stability of the SSLB model system

As with any model membrane system, SSLBs present several technical limitations to their tunability, which was explored to the extent we were satisfied with, but by no means to completion.

Since they can be re-suspended in any buffer of choice, SSLB membrane integrity was examined under TEM for a wide range of buffer conditions. The integrity was preserved in both high (up to 1 M NaCl) and no salt (MilliQ water) conditions and also through 40˚C overnight incubation, which indicated the lipids were quite stable once they assembled on the substrate. pH conditions, though not systematically tested, did affect

membrane integrity at the lower end of pH of 2-4, but did not disrupt it at experimental conditions of pH 6-8. It appeared that as long as the conditions do not severely affect chemical integrity of lipids or the inner leaflet adhesion to the substrate, the membrane remains remarkably stable.

Most SSLB experiments in this work were carried out using a combination of zwitterionic and charged lipids, but biological membranes such as the synaptic vesicle membrane contain sterol species as well as phospholipids with intrinsic curvature; for instance, those with a phosphoethanolamine (PE) headgroup have a much smaller headgroup area compared to the cross-sectional area of their tails. The resulting, so called "cone-shaped" geometry is a feature of the PE lipids that thermodynamically favors self-assembled structures deviating from spherical, vesicular structures.[30] The threshold PE composition that produced single lipid bilayer morphology was investigated, for the reason that an abundant portion (close to 30 mol% by some estimates) of synaptic vesicles phospholipids have the ethanolamine headgroup.[17] It was found that 30 mol% of DOPE in the DOPC:DOPS:DOPE (20:50:30) mixture presented a tubular "bridging" morphology that bridged one SSLB membrane to another (Fig. 2.8). This morphology, previously unobserved in binary mixtures of PC and charged lipid, is entirely possible for high PE containing mixtures when SSLBs are forced to contact one another during centrifugation or via aggregation.

Another key challenge was the colloidal stability of SSLBs in physiologic salt conditions. The high amount of salt (> 100 mM NaCl) screens charged colloids and promotes their aggregation, which typically happened over two days and so the sample had to be used fresh for binding and X-ray experiments. SSLBs as probed by dynamic light scattering were not perfectly monodisperse upon fresh preparation because the

centrifugation process involved in SSLB purification probably forced some population of SSLBs to aggregated states. Surprisingly, the more highly charged SSLBs were found to have a greater average hydrodynamic diameter than zwitterionic SSLBs (Table 2.3). This result was counter-intuitive considering more surface charge would confer better colloidal stability due to surface charge-charge repulsion. The origin of the highly charged SSLB aggregation is an open avenue for investigation.

Moreover, SSLBs with < 50 nm diameter did not prove to be colloidally stable in aqueous conditions for experiments. These small colloids aggregated over hours, although excellent lipid coverage was observed under TEM. SSLBs when aggregated cannot have the desired curvature of individual SSLBs, which reduced their potential to be used as a model system to investigate binding as a function of small changes in curvature – which was one of the original intents of creating this platform. Nonetheless they served a good model system for comparison with LUVs, and intermembrane force response experiments as detailed in chapter 4.

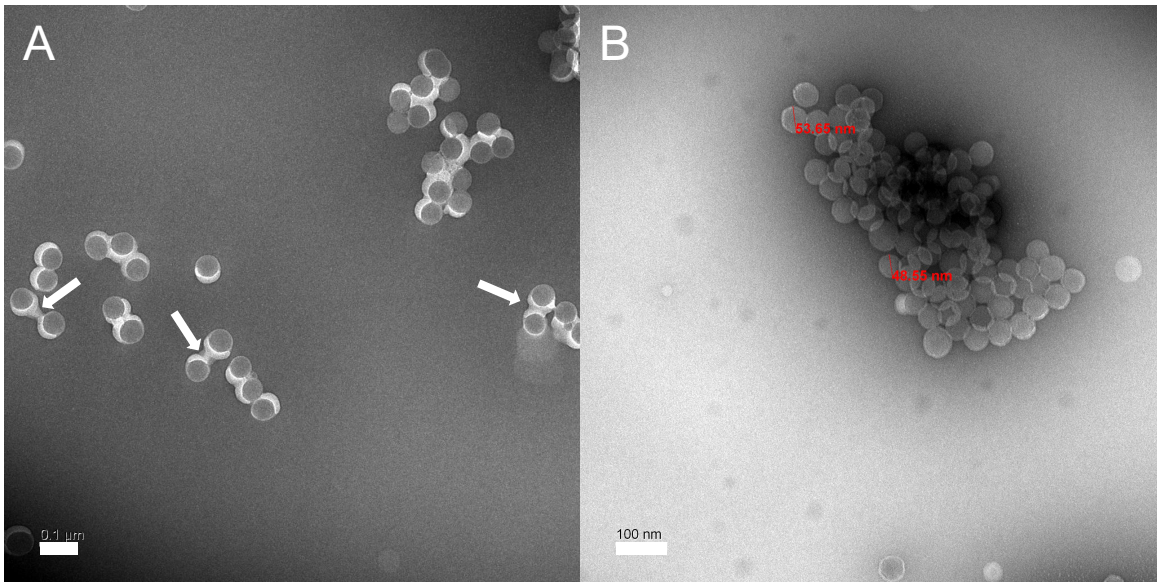

Fig. 2.8. Examples of limitations to SSLBs in their compositional tractability and colloidal stability.
(A). TEM image of SSLBs containing 30 mol% DOPE (here, the exact composition is DOPC:DOPS:DOPE, 20:50:30 mol%) shows evidence for lipid bridging morphology, pointed out with white arrows, that is unobserved in lower PE% mixtures.
(B). DOPC:DOPS (1:1) SSLBs formed on 40 nm nanoparticles were found in aggregated clusters under TEM; DLS corroborated populations whose average size exceeded 500 nm. (DLS data not shown). Scale bar: 100 nm.

2.5. Comparison of αS binding of SSLBs against vesicles

The improved SSLB model system allowed for the possibility of examining substrate-enforced curvature effects on αS membrane binding — that is, ensemble binding experiments comparing SSLBs to LUV across multiple curvatures. However, directly comparing αS binding to SSLBs across 60, 50 and 40 nm particle diameters was difficult due to the abovementioned issue of colloidal stability for smaller 50 and 40 nm particles.

For preliminary binding experiments, DOPC:DOPA (1:1) SSLBs on either 60, 50, or 40 nm particles were bulk produced and designated as titrand, while αS was loaded in the syringe as titrant of the ITC instrument. After confirming SSLB membrane integrity

upon addition of αS via TEM (Fig. 2.9A and 2.9B) — in order to rule out possible heat evolution from lipid remodeling — we monitored the exothermic heat of reaction throughout a series of titrations and fit the raw heat data using the well-established independent binding sites model whose binding equations are detailed in chapter 5 (Fig. 2.9D). Binding affinity in terms of K_d and binding stoichiometry in terms of lipids per bound protein were extracted from the fit and plotted, as a function of curvature, defined here as inverse diameter (Fig. 2.9E and 2.9F). In general, SSLBs compared to LUVs increased both the binding affinity and stoichiometry of αS on membrane surface, which suggested that forcing a specific curvature leads to a presentation of more lipid packing defects, promoting αS membrane binding. This view of defect driven αS binding is consistent with multiple lines of evidence in literature, e.g., an increase in binding affinity from (1) gel phase vesicles,[31] (2) greater inclusion of PE,[32] and (3) more unsaturation in lipid tails.[33]

With that said, the thermodynamic binding parameters were in line with previously reported measurements for αS binding to similar compositions,[34,35] suggesting that the SSLBs can indeed be used as a viable platform for binding experiments. Ultimately, however, the problem associated with colloidally stabilizing SSLBs was too difficult of a challenge for quantitating membrane curvature effects on binding. Solving this problem could dramatically increase their utility as a probe for curvature dependent binding.

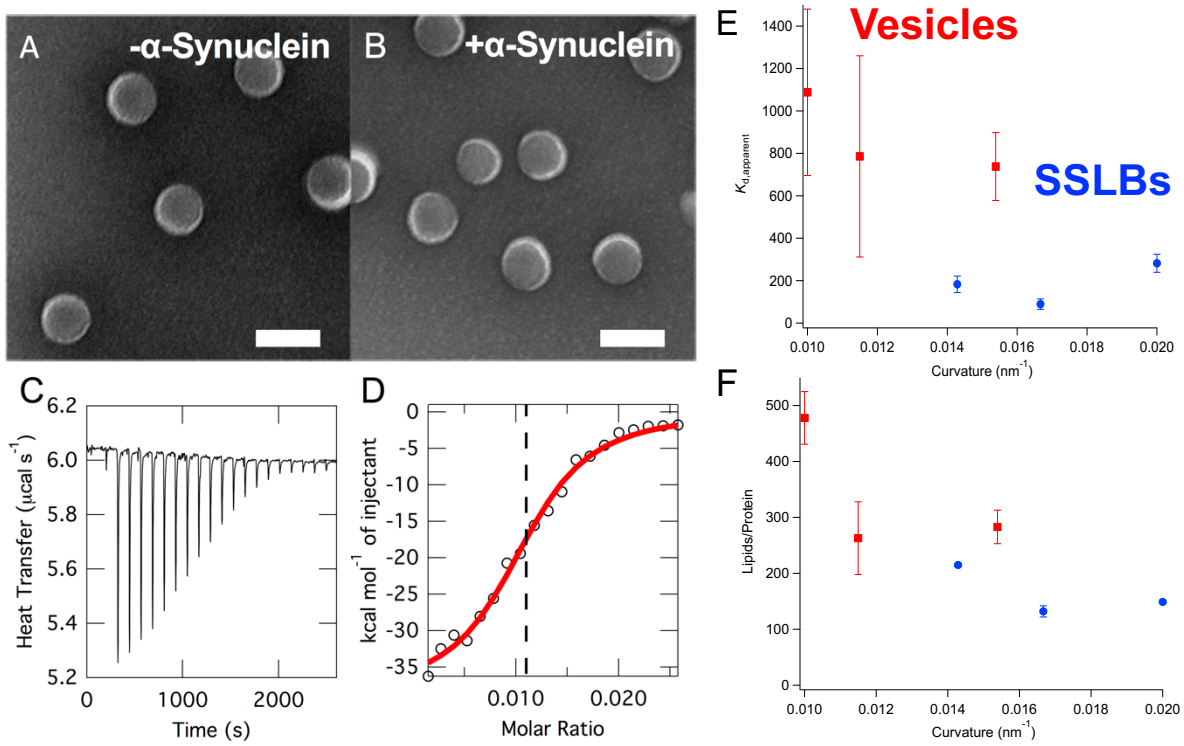

Fig. 2.9. The use of SSLBs for ensemble binding experiments.
SSLBs compared to LUVs increased both binding affinity and binding stoichiometry between αS and lipids.
(A-B). The addition of high concentration of αS (at protein-to-outer lipid ratio of 1/40) does not appear to disrupt membrane integrity of DOPC:DOPA (1:1) SSLBs formed on 60 nm nanoparticles, as shown by TEM images. SSLBs without αS (A) and with the addition of αS (B) show a 5 nm thick membrane coated around all nanoparticles. Scale bar: 100 nm.
(C). However, ITC measurements of αS injections into a solution of SSLBs in HB7 buffer at 37°C show heat released from the expected binding of αS.
(D). The binding isotherm reveals an affinity of k_D of ~200 uM^{-1} and binding stoichiometry of one protein per every ~100 outer lipids.
(E-F). Both binding affinity (E) and binding stoichiometry (F) increased from using the SSLBs rather than LUVs of same composition.

2.6. References

(1) Snead, D.; Eliezer, D. Intrinsically Disordered Proteins in Synaptic Vesicle Trafficking and Release. *J. Biol. Chem.* **2019**, *294* (10), 3325–3342. https://doi.org/10.1074/jbc.REV118.006493.

(2) Rizo, J.; Rosenmund, C. Synaptic Vesicle Fusion. *Nat. Struct. Mol. Biol.* **2008**, *15* (7), 665–674. https://doi.org/10.1038/nsmb.1450.

(3) Rizo, J.; Xu, J. The Synaptic Vesicle Release Machinery. *Annu. Rev. Biophys.* **2015**, *44* (1), 339–367. https://doi.org/10.1146/annurev-biophys-060414-034057.

(4) Chung, P. J.; Zhang, Q.; Hwang, H. L.; Leong, A.; Maj, P.; Szczygiel, R.; Dufresne, E. M.; Narayanan, S.; Adams, E. J.; Lee, K. Y. C. α-Synuclein Sterically Stabilizes Spherical Nanoparticle-Supported Lipid Bilayers. *ACS Appl. Bio Mater.* **2019**, *2* (4), 1413–1419. https://doi.org/10.1021/acsabm.8b00774.

(5) Wytrwal, M.; Bednar, J.; Nowakowska, M.; Wydro, P.; Kepczynski, M. Interactions of Serum with Polyelectrolyte-Stabilized Liposomes: Cryo-TEM Studies. *Colloids Surfaces B Biointerfaces* **2014**, *120*, 152–159. https://doi.org/10.1016/j.colsurfb.2014.02.040.

(6) Antonny, B. Mechanisms of Membrane Curvature Sensing. *Annu. Rev. Biochem.* **2011**, *80* (1), 101–123. https://doi.org/10.1146/annurev-biochem-052809-155121.

(7) Lindberg, R.; Sjöblom, J.; Sundholm, G. Preparation of Silica Particles Utilizing the Sol-Gel and the Emulsion-Gel Processes. *Colloids Surfaces A Physicochem. Eng. Asp.* **1995**, *99* (1), 79–88. https://doi.org/10.1016/0927-7757(95)03117-V.

(8) Guo, J.; Liu, X.; Cheng, Y.; Li, Y.; Xu, G.; Cui, P. Size-Controllable Synthesis of Monodispersed Colloidal Silica Nanoparticles via Hydrolysis of Elemental Silicon. *J. Colloid Interface Sci.* **2008**, *326* (1), 138–142. https://doi.org/10.1016/j.jcis.2008.07.020.

(9) Wang, X.; Li, Y. Monodisperse Nanocrystals: General Synthesis, Assembly, and Their Applications. *Chemical Communications*. **2007**, pp 2901–2910. https://doi.org/10.1039/b700183e.

(10) Stöber, W.; Fink, A.; Bohn, E. Controlled Growth of Monodisperse Silica Spheres in the Micron Size Range. *J. Colloid Interface Sci.* **1968**, *26* (1), 62–69. https://doi.org/10.1016/0021-9797(68)90272-5.

(11) Chan, Y. H. M.; Boxer, S. G. Model Membrane Systems and Their Applications. *Curr. Opin. Chem Biol.* **2007**, *11* (6), 581–587. https://doi.org/10.1016/j.cbpa.2007.09.020.

(12) Castellana, E. T.; Cremer, P. S. Solid Supported Lipid Bilayers: From Biophysical

Studies to Sensor Design. *Surf. Sci. Rep.* **2006**, *61* (10) 429–444. https://doi.org/10.1016/j.surfrep.2006.06.001.

(13) Anderson, T. H.; Min, Y.; Weirich, K. L.; Zeng, H.; Fygenson, D.; Israelachvili, J. N. Formation of Supported Bilayers on Silica Substrates. *Langmuir* **2009**, *25* (12), 6997–7005. https://doi.org/10.1021/la900181c.

(14) Bayerl, T. M.; Bloom, M. Physical Properties of Single Phospholipid Bilayers Adsorbed to Micro Glass Beads. A New Vesicular Model System Studied by 2H-Nuclear Magnetic Resonance. *Biophys. J.* **1990**, *58* (2), 357–362. https://doi.org/10.1016/S0006-3495(90)82382-1.

(15) Fu, R.; Gill, R. L.; Kim, E. Y.; Briley, N. E.; Tyndall, E. R.; Xu, J.; Li, C.; Ramamurthi, K. S.; Flanagan, J. M.; Tian, F. Spherical Nanoparticle Supported Lipid Bilayers for the Structural Study of Membrane Geometry-Sensitive Molecules. *J. Am. Chem. Soc.* **2015**, *137* (44), 14031–14034. https://doi.org/10.1021/jacs.5b08303.

(16) Mornet, S.; Lambert, O.; Duguet, E.; Brisson, A. The Formation of Supported Lipid Bilayers on Silica Nanoparticles Revealed by Cryoelectron Microscopy. *Nano Lett.* **2005**, *5* (2), 281–285. https://doi.org/10.1021/nl048153y.

(17) Takamori, S.; Holt, M.; Stenius, K.; Lemke, E. A.; Grønborg, M.; Riedel, D.; Urlaub, H.; Schenck, S.; Brügger, B.; Ringler, P.; et al. Molecular Anatomy of a Trafficking Organelle. *Cell* **2006**, *127* (4), 831–846. https://doi.org/10.1016/j.cell.2006.10.030.

(18) Zhang, S.; Li, J.; Lykotrafitis, G.; Bao, G.; Suresh, S. Size-Dependent Endocytosis of Nanoparticles. *Adv. Mater.* **2009**, *21* (4), 419–424. https://doi.org/10.1002/adma.200801393.

(19) Jiang, W.; Kim, B. Y. S.; Rutka, J. T.; Chan, W. C. W. Nanoparticle-Mediated Cellular Response Is Size-Dependent. *Nat. Nanotechnol.* **2008**, *3* (3), 145–150. https://doi.org/10.1038/nnano.2008.30.

(20) Ashley, C. E.; Carnes, E. C.; Phillips, G. K.; Padilla, D.; Durfee, P. N.; Brown, P. A.; Hanna, T. N.; Liu, J.; Phillips, B.; Carter, M. B.; et al. The Targeted Delivery of Multicomponent Cargos to Cancer Cells by Nanoporous Particle-Supported Lipid Bilayers. *Nat. Mater.* **2011**, *10* (5), 389–397. https://doi.org/10.1038/nmat2992.

(21) Liu, X.; Situ, A.; Kang, Y.; Villabroza, K. R.; Liao, Y.; Chang, C. H.; Donahue, T.; Nel, A. E.; Meng, H. Irinotecan Delivery by Lipid-Coated Mesoporous Silica Nanoparticles Shows Improved Efficacy and Safety over Liposomes for Pancreatic Cancer. *ACS Nano* **2016**, *10* (2), 2702–2715. https://doi.org/10.1021/acsnano.5b07781.

(22) Ferhan, A. R.; Yoon, B. K.; Park, S.; Sut, T. N.; Chin, H.; Park, J. H.; Jackman, J. A.; Cho, N. J. Solvent-Assisted Preparation of Supported Lipid Bilayers. *Nat. Protoc.*

2019, *14* (7), 2091–2118. https://doi.org/10.1038/s41596-019-0174-2.

(23) Tabaei, S. R.; Choi, J. H.; Haw Zan, G.; Zhdanov, V. P.; Cho, N. J. Solvent-Assisted Lipid Bilayer Formation on Silicon Dioxide and Gold. *Langmuir* **2014**, *30* (34), 10363–10373. https://doi.org/10.1021/la501534f.

(24) Bartels, T.; Kim, N. C.; Luth, E. S.; Selkoe, D. J. N-Alpha-Acetylation of α-Synuclein Increases Its Helical Folding Propensity, GM1 Binding Specificity and Resistance to Aggregation. *PLoS One* **2014**, *9* (7). https://doi.org/10.1371/journal.pone.0103727.

(25) Tsui, F. C.; Ojcius, D. M.; Hubbell, W. L. The Intrinsic PKa Values for Phosphatidylserine and Phosphatidylethanolamine in Phosphatidylcholine Host Bilayers. *Biophys. J.* **1986**, *49* (2), 459–468. https://doi.org/10.1016/S0006-3495(86)83655-4.

(26) Faizi, H. A.; Frey, S. L.; Steinkühler, J.; Dimova, R.; Vlahovska, P. M. Bending Rigidity of Charged Lipid Bilayer Membranes. *Soft Matter* **2019**, *15* (29), 6006–6013. https://doi.org/10.1039/c9sm00772e.

(27) Marsh, D. *Handbook of Lipid Bilayers,* 2nd Ed.

(28) Chung, P. J.; Hwang, H. L.; Dasbiswas, K.; Leong, A.; Lee, K. Y. C. Osmotic Shock-Triggered Assembly of Highly Charged, Nanoparticle-Supported Membranes. *Langmuir* **2018**, *34* (43), 13000–13005. https://doi.org/10.1021/acs.langmuir.8b03026.

(29) Souza, T. G. F.; Ciminelli, V. S. T.; Mohallem, N. D. S. A Comparison of TEM and DLS Methods to Characterize Size Distribution of Ceramic Nanoparticles. In *Journal of Physics: Conference Series*; Institute of Physics Publishing, 2016; Vol. 733. https://doi.org/10.1088/1742-6596/733/1/012039.

(30) Rappolt, M.; Hickel, A.; Bringezu, F.; Lohner, K. Mechanism of the Lamellar/Inverse Hexagonal Phase Transition Examined by High Resolution x-Ray Diffraction. *Biophys. J.* **2003**, *84* (5), 3111–3122. https://doi.org/10.1016/S0006-3495(03)70036-8.

(31) O'Leary, E. I.; Jiang, Z.; Strub, M. P.; Lee, J. C. Effects of Phosphatidylcholine Membrane Fluidity on the Conformation and Aggregation of N-Terminally Acetylated α-Synuclein. *J. Biol. Chem.* **2018**, *293* (28), 11195–11205. https://doi.org/10.1074/jbc.RA118.002780.

(32) Jo, E.; McLaurin, J. A.; Yip, C. M.; St. George-Hyslop, P.; Fraser, P. E. α-Synuclein Membrane Interactions and Lipid Specificity. *J. Biol. Chem.* **2000**, *275* (44), 34328–34334. https://doi.org/10.1074/jbc.M004345200.

(33) Hellstrand, E.; Grey, M.; Ainalem, M.-L.; Ankner, J.; Forsyth, V. T.; Fragneto, G.; Haertlein, M.; Dauvergne, M.-T.; Nilsson, H.; Brundin, P.; et al. Adsorption of α-

Synuclein to Supported Lipid Bilayers: Positioning and Role of Electrostatics. *ACS Chem. Neurosci.* **2013**, *4* (10), 1339–1351. https://doi.org/10.1021/cn400066t.

(34) Middleton, E. R.; Rhoades, E. Effects of Curvature and Composition on α-Synuclein Binding to Lipid Vesicles. *Biophys. J.* **2010**, *99* (7), 2279–2288. https://doi.org/10.1016/j.bpj.2010.07.056.

(35) Eliezer, D.; Kutluay, E.; Bussell, R.; Browne, G. Conformational Properties of α-Synuclein in Its Free and Lipid-Associated States. *J. Mol. Biol.* **2001**, *307* (4), 1061–1073. https://doi.org/10.1006/jmbi.2001.4538.

CHAPTER 3.

MEMBRANE BINDING of α-SYNUCLEIN CONFERS STERIC STABILIZATION OF SSLBs

3.1. Overview: αS adsorption disrupts colloidal aggregates of SSLBs

The conformational plasticity of membrane bound αS,[1–3] and in particular the possibility of a conformation "bridging" two membrane surfaces via its two alpha helices (Fig. 1.4), motivated the studies in this chapter. They are essentially aimed at the question – how does αS, once membrane bound, mediate interactions of apposing membrane surfaces? From a polymer physics view, the complex of αS and the membrane looks a lot like physisorbed polymer,[4] on a curved nanoparticle surface in a good solvent (Fig. 1.4), where polymer chains projecting away from the surface can adopt compact or fully extended phases that have a remarkable bearing on how two membrane surfaces "see" each other (Fig. 3.1). This physical, reductionist perspective allowed us to see this problem as a version of polymer graft-mediated interactions between spherical colloids. On the other hand, the biological implications hanging over this colloids problem manifest in numerous diagrams depicting colloidal behavior of synaptic vesicles[5,6] – which have been shown to exist in multiple liquid-liquid phases[7] and can cluster or de-cluster to biological signals (Fig. 1.2). We hypothesized this protein can possibly modify interactions of membrane surfaces depending on its membrane surface density and polymer conformation. The much-needed polymer physics insights can help address the gap between synaptic vesicles biochemistry (binding reactions involved throughout neurotransmission) and their biophysics (colloidal behavior) and enrich our overall understanding of αS physiology.

The SSLBs developed in the previous chapter are uniquely designed to perform colloids measurements via X-ray scattering, which can capture both their structure (SAXS) and dynamics (XPCS) in solution. The spherical colloids (SSLB-αS complexes) can be probed for their time-averaged snapshot of their interaction state (attractive aggregation versus repulsive stabilization) and for their average diffusivity resulting from their interaction potential using SAXS and XPCS respectively.

The X-ray scattering measurements presented in this and the following chapter revealed that membrane bound αS confers a repulsive interaction potential between the SSLB colloids, implicating αS role in *steric stabilization* of synaptic vesicles and binding induced release from condensed pools. Some background and physics involved in polymer grafted colloids and X-ray scattering are addressed below.

3.1.1. Steric repulsive forces between polymer grafted surfaces

The general potential energy-distance curve for two membrane surfaces separated by some distance is shown qualitatively in Fig. 3.1. As the interaction is multimodal (and it should also be noted that actual biomembranes are far from equilibrium), individual force contributions are difficult to assess experimentally. It has well been known, however, that two polymer coated surfaces experience a significant repulsive force when the surfaces are forced to approach each other to a distance below a few R_g and coated polymers of apposing surfaces begin to overlap.[9,10] The unfavorable entropic decrease associated with overlapping polymer chains drives the steric repulsion of two surfaces. This general phenomenon is called *steric stabilization* in polymer literature.

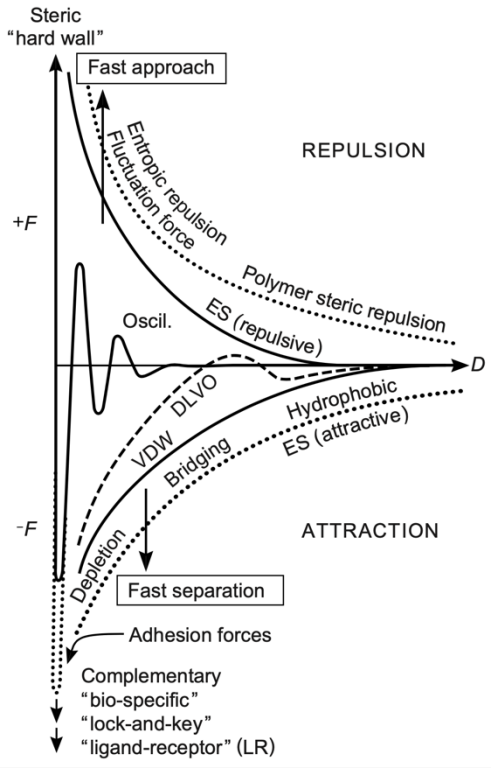

Fig. 3.1. A diagram of generic interaction potentials between two colloids or membrane surfaces.
The intermembrane forces are generally complex and multifactorial. One of the simplest models (*Derjaguin—Landau—Verwey—Overbeek* or "DLVO" theory shown on figure) constructs a potential as a sum of repulsive double-layer electrostatics and attractive van der Waals forces. Biomolecular self-assembled structures are not at equilibrium which makes it challenging to calculate interaction potentials. Adapted from ref. (8).

There have been a large number of theories and experiments to quantitate the intersurface repulsive forces as a function of coated polymer concentration, identity, solvent, and more. The steric interaction theories are complex[9,11–13] and are not reviewed here but in many cases can be essentially reduced to fit experimental data, *e.g.* surface force apparatus measurements shown in Fig. 3.2, a result of one of the earliest lipid membrane experiments where covalently grafted PEG-DSPE lipid membranes were forced to approach each other in three different coverage regimes: "non-interacting", "weakly overlapping", and "strongly overlapping".[10] Here, the electrostatic and steric

repulsive interactions overall dominate the attractive van der Waals forces; specifically, the long-range electrostatics force is responsible for repulsion at a larger separation distance, and the short-range steric force dominates at smaller distances. Notably, theoretical models of intersurface repulsive force[9,11,12] – accounting for distance apart, surface coverage, R_g, thickness of brush, osmotic repulsion between the coils, and energetic cost of stretching polymer chains — were able to explain the force-distance profiles for all three coverage regimes, conveying an overall agreement between theory and experiment in ethylene oxide grafted lipid membranes.

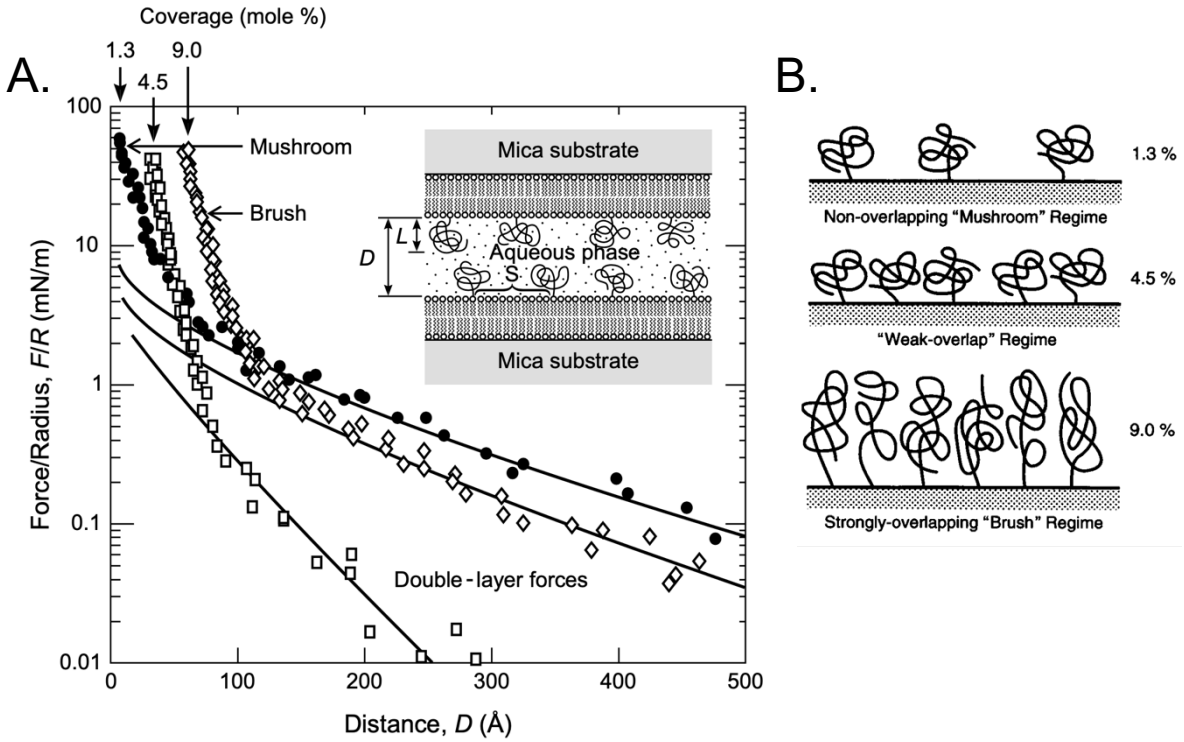

Fig. 3.2. Forces between two lipid membranes grafted with polyethylene glycol polymer chains as measured by surface force apparatus.
(A). Surface force apparatus measurements performed with DSPE-ethylene oxide$_{45}$ in KNO_3 solutions at 21 °C where the polymer chains have a Flory radius of 35 Å.[10] For all three different surface coverage conditions, repulsive forces at large *D* can be explained by double-layer forces because the Debye lengths much are longer than decay lengths of steric forces. (The shown fit to the data is theoretical double-layer repulsion at constant charge and surface potential.) At small *D*, chain-chain interactions drastically increase measured repulsive forces depending on surface coverage. Mushroom regime data were

fit to the Edwards model[12] and brush regime data was fit to the de Gennes model[9] which quantitatively explained the force profiles (these fits are not shown here).
(B). Schematic showing different coverage regimes that markedly affect inter-surface repulsion. Adapted from refs. (8,10).

Covalently grafted chains on 2-D membrane surfaces, as exemplified in Fig. 3.2, have been well characterized up to date and are now pretty well understood with theoretical models accounting for different interaction regimes, but for *weakly* surface bound polymers that can be highly dynamic, such as peripherally associating membrane proteins, it is difficult to form general models.

Measuring interaction forces between 3-D colloids can be done by applying depletion force with well-characterized polymeric agent and analyzing their spatial correlation via SAXS. While these force experiments are covered in detail in Chapter 4, the results that definitively point to αS steric stabilization are described in this chapter.

3.1.2. Small angle X-ray scattering (SAXS) of spherical scatterers

We employed SAXS to probe the liquid "structure" of SSLBs. As explained in the previous chapter, because of the highly electron-dense silica core, SSLBs scatter X-rays much more intensely than vesicles allowing for X-ray experiments. In addition, due to their monodispersity, they can be treated as isotropic, spherical scatterers. The colloidal structure of SSLBs, as a function of αS coverage, was probed via SAXS where the scattering of particles can be taken as a proxy for their position in solution. The general schematic of a SAXS measurement and where we carried out most of these measurements are shown in Fig 3.3. The SAXS of spherical objects in dilute (noninteracting) conditions can be derived as follows.[14]

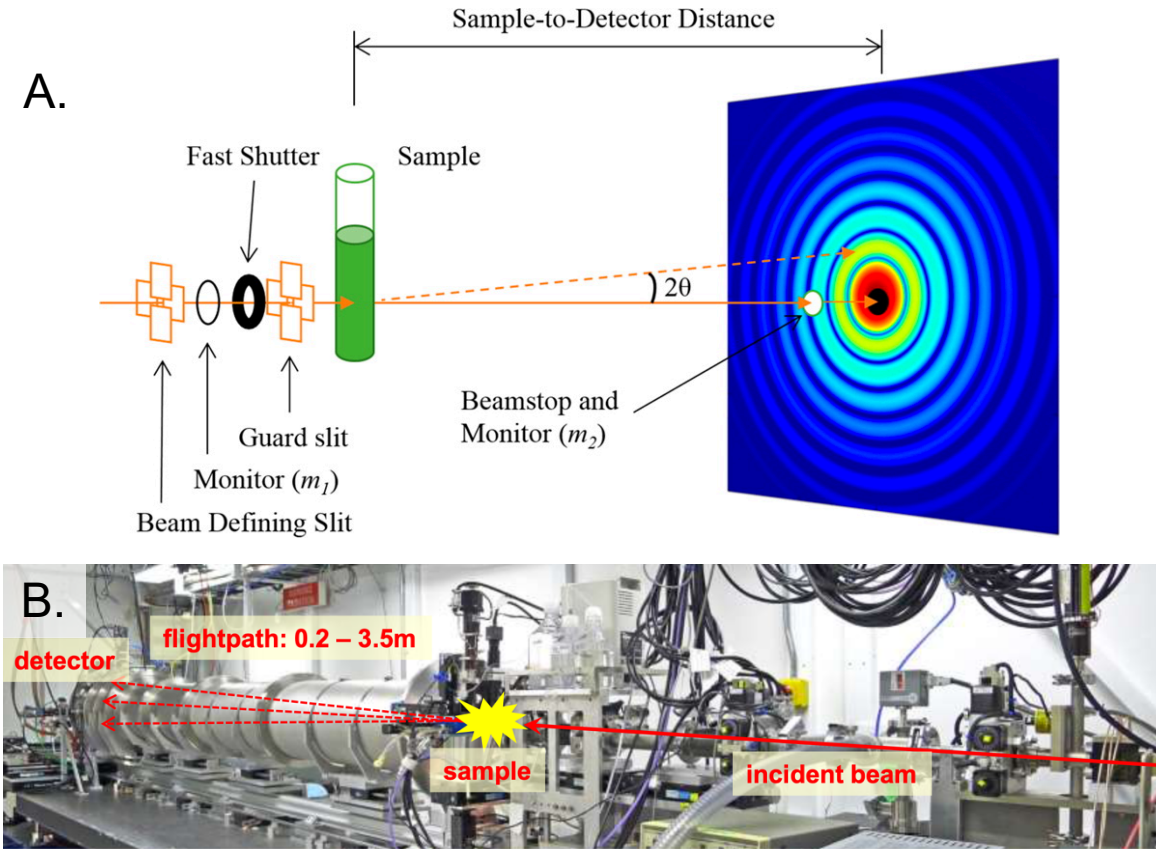

Fig. 3.3. General schematic of a SAXS measurement and the experimental setup at Stanford Synchrotron Radiation Lightsource (SSRL).
(A). A monochromatic X-ray beam transmits through sample in a glass capillary and resulting scattering is recorded by two-dimensional, position sensitive detector. Scattered intensities can be azimuthally averaged (i.e. along the scattering "rings") to produce a plot of intensity vs. scattered wavevector. Adapted from ref. (15).
(B). Photograph of the hutch at beamline 4-2 at SSRL where most of the SAXS data was acquired. Adapted from ref. (16).

We begin with the general scattering equation, where the obtained intensity is the square of the amplitude, which is the scattered density at position r multiplied by the phase factor summed over all space.

$$I_{SAXS}(\vec{q}) = |A(\vec{q})|^2 = \left| \int_V \rho(\vec{r}) \exp(i\vec{q} \bullet \vec{r})\, d^3r \right|^2 \qquad (3.1)$$

where the variables as would be normally defined are: the wavevector transfer, $\vec{q} = \frac{4\pi}{\lambda}\sin\theta$, the scattering angle, θ, and the scattering length density at position r, $\rho(\vec{r})$. If we consider scattering from a single particle, and assume that the scattering length density of every particle is uniform, Equation (3.1) can be then written for a single particle as,

$$I(\vec{q})_{single\ particle} = \left|\rho_{single\ particle} - \rho_{solvent}\right|^2 \left|\int_{V_P} \exp(i\vec{q}\bullet\vec{r})\, dV_P\right|^2$$

$$= |\Delta\rho|^2 \left|\int_{V_P} \exp(i\vec{q}\bullet\vec{r})\, dV_P\right|^2 = |\Delta\rho|^2 {V_p}^2\, |F(\vec{q})|^2$$

where $F(\vec{q})$, the single particle form factor, is defined as

$$F(\vec{q}) = \frac{1}{V_P}\int_{V_P} \exp(i\vec{q}\bullet\vec{r})\, dV_P \qquad (3.2)$$

Here, the subscript p simply refers to single particle. This form factor integral depends on the size and shape of the particle. Equation (3.2) can be evaluated analytically for a perfect sphere, adopting spherical coordinates.

$$F(q) = \frac{1}{V_P}\int_0^R r^2 \int_0^{2\pi} exp(iqrcos\theta) \int_0^R \sin\theta\, d\theta d\phi dr$$

$$F(q) = \frac{1}{V_P}\int_0^R 4\pi r^2 \frac{\sin(qr)}{qr}\, dr$$

$$= 3\left(\frac{\sin(qr) - qrcos(qr)}{q^3 r^3}\right) = \frac{3J_1(qr)}{qr}$$

where $\boldsymbol{J_1}$ is the Bessel function of the first kind. Then we can evaluate the scattering from a single particle,

$$\boxed{I(q)_{single\ particle} = |\Delta\rho|^2 {V_p}^2 \, |F(\vec{q})|^2 = |\Delta\rho|^2 {V_p}^2 \left|\frac{3J_1(qr)}{qr}\right|^2} \quad (3.3)$$

The argument of the Bessel function indicates that the period of oscillations in the SAXS profile is inversely proportional to the sphere radius. An example of SAXS profile of silica nanoparticles that we obtained is shown in Fig. 3.4. Given here is the scattering for spherical particles, but one can similarly evaluate form factors for differently shaped particles (cylindrical rod, ellipsoid, flat disk, etc.).

In the presence of interparticle correlations, Equation (3.3) can be modified by introducing an appropriate structure factor $S(\vec{q})$ as shown.

$$\boxed{I_{SAXS}(\vec{q}) = |\Delta\rho|^2 {V_p}^2 \, |F(\vec{q})|^2 S(\vec{q})} \quad (3.4)$$

Interparticle correlations can emerge from the increased volume fraction of particles in solution. As the particle volume fraction increases and the individual particles begin to feel their neighbors, a broad "correlation peak" begins to appear at ~$\frac{2\pi}{d}$ where *d* is roughly the interparticle distance (Fig. 3.5). At and above 20% volume fraction of particles in solution, the interparticle correlation begins to appear. As detailed in Section 3.3, our interpretation of what αS adsorption does to SSLB colloidal structure hinges on the presence of SSLB interparticle correlation peak.

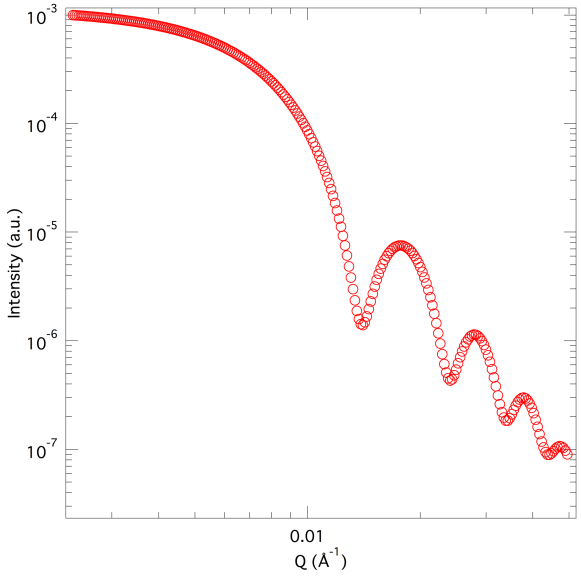

Fig. 3.4. SAXS of 60 nm amine-functionalized silica nanoparticles in ethanol shows expected profile consistent with spherical particles.
The azimuthally averaged SAXS data is consistent with the Bessel function-like profile expected of spherical scatterers (Equation 3.3). The deviation from exact shape of Bessel function results from imperfect sphericity and monodispersity.

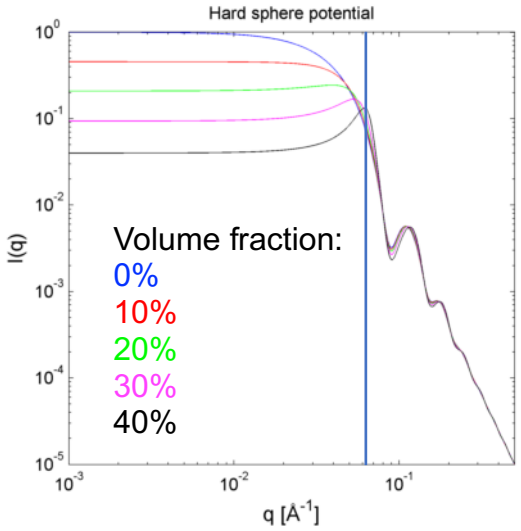

Fig. 3.5. One effect of interparticle correlations: Increase in particle volume fractions gives rise to a correlation peak that approximately indicates nearest neighbor particle distance.
The simulated SAXS profiles for 10 nm spherical particles with differing volume fractions. An interparticle correlation peak, indicated by vertical blue line, emerges at $q = \frac{2\pi}{d} = \frac{2\pi}{10\ nm} = 0.063$ Å^{-1}. Adapted from ref. (17).

3.1.3. X-ray photon correlation spectroscopy (XPCS) of nanoscopic objects

XPCS has traditionally been used to study complex fluids of polymer mixtures, colloids, and surfactants with complicated phase and rheological behavior. XPCS, which is the X-ray analog of DLS, can provide information at smaller length scales inaccessible to optical measurements. Dynamics measurements are made possible with highly coherent synchrotron X-rays and fast detectors to record scattering at high frequencies — which have been recently developed for this technique.[18]

Our interest in XPCS began when we observed a cloudy aggregate of SSLB-αS-PEG mixture in a glass capillary (more on this observation in Chapter 4) and wanted to extract the diffusion of αS-bound SSLBs in this complex mixture. With XPCS data, we were able to calculate the average diffusivity of SSLBs in solution as a function of αS concentration, corroborating the time-averaged structural information obtained from SAXS.

The theory behind XPCS is explained concisely below.[18] The coherent X-ray beam impinging through a sample results in a speckled scattering pattern whose temporal evolution can be tracked by a high-speed detector (Fig. 3.6). The time dependent speckle patterns can be evaluated by intensity-time autocorrelation function for a given $\vec{q}$, at a detector pixel (i, j) (Equation 3.5).

$$\Delta g_2(\vec{q}, t) = \frac{\langle I_{i,j}(\vec{q}, t') \cdot I_{i,j}(\vec{q}, t' + t) \rangle}{\langle I_{i,j}(\vec{q}, t') \rangle^2} \quad (3.5)$$

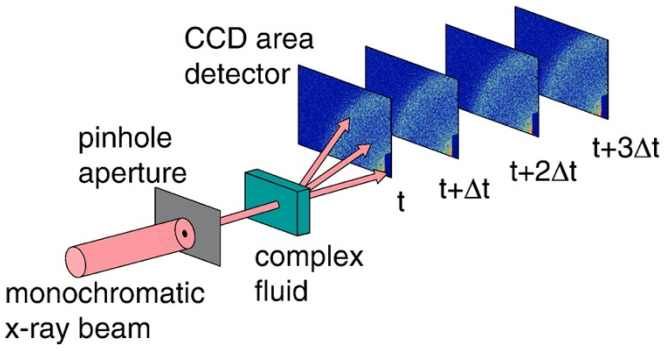

Fig. 3.6. Schematic of an XPCS measurement in SAXS geometry.
A sample of complex fluid scatters coherent synchrotron X-ray beam to generate speckle patterns over time. At multiple scattering wavevectors, intensity-time autocorrelation functions (Equation 3.5) are constructed, whose decay can be analyzed to yield dynamical information. Adapted from ref. (18).

For monodisperse and non-interacting spheres, the solution to the diffusion equation under normal boundary conditions reveals diffusivity D is proportional to mean square displacement (and hence, inversely proportional to q^2). In this simplified case, the $\Delta g_2(\vec{q}, t)$ can be fit to an exponential decay,

$$\Delta g_2(q, t) = be^{-2(t/\tau(q))} \quad (3.6)$$

where b is the Siegert factor (an instrumental factor ranging from 0 to 1 that accounts for beam coherence and detector characteristics [18]), and $\tau(q)$ is the relaxation time constant that relates to diffusivity, $\tau(q) = \frac{1}{Dq^2}$.

In the case of abnormal diffusion (*e.g.* polydispersed population) where a simple exponential decay cannot fit the Δg_2, a stretched exponential decay is most commonly used to fit the data, using an expression where β is the stretched exponential argument.

$$\Delta g_2(q, t) = be^{-2(t/\tau_{SE}(q))^{\beta}} \quad (3.7)$$

Here, the subscript "SE" refers to "stretched exponential" and $\beta = 1$ indicates normal diffusion, $\beta < 1$ indicates subdiffusion, and $\beta > 1$ indicates superdiffusion.

3.2. Materials and methods

3.2.1. Materials

Materials including DOPC, DOPA, aqueous buffer components, and amine-functionalized 60 nm silica nanoparticles were purchased and N-terminally acetylated αS was expressed and purified as detailed in Chapter 2.2.

3.2.2. Sample preparation for SAXS and XPCS

SAXS and XPCS samples were prepared by mixing: DOPC:DOPA (1:1, mol%) SSLBs (refer to Chapter 2.2 for their preparation) suspended in HB7 (10 mM HEPES, 100 mM NaCl at pH 7.0) buffer at a nominal silica concentration of 4 mg/mL; concentrated αS stock solution at ~100 μM; and extra HB7 such that the final concentration of SSLB was 1.6 mg/mL of silica at the desired protein to outer lipid ratio. Final sample volume was 50 μL. Each sample was loaded into a thin capillary and incubated in 37° C oven for equilibration, and subsequently measured via SAXS or XPCS.

3.2.3. SAXS and XPCS protocol

SAXS measurements were performed at beamline 4-2 at the Stanford Synchrotron Radiation Lightsource, SLAC National Accelerator Laboratory at 9 KeV with a Si(111) monochromator. Scattering data were taken with a 2D area detector (MarUSA, Evanston, Illinois) with a sample-to-detector distance of 3.5 m. Beampath length and detector were calibrated with a silver behenate control, with beam size approximately 150 μm (vertical) x 200 μm (horizontal) and photon flux of 3×10^{12} photons/second.

XPCS measurements were performed at station 8-ID-I of the Advanced Photon Source, Argonne National Laboratory at 10.91 keV with a Ge(111) monochromator.

Scattering data were taken with a custom 2D area detector capable of operating continuously at a 50 kHz frame rate, with a sample-to-detector distance of 4 m. Beam path length and detector were calibrated with a silver behenate control. The nominal x-ray beam size on the sample was 4 μm (vertical) x 15 μm (horizontal) with x-ray photon flux of 4 x 10^{10} photons/second. Each dataset was taken by exposing a fresh part of the sample for 4 seconds and autocorrelations from 300 such acquisitions on fresh parts of the sample were averaged together to yield the final autocorrelation function. Radiation damage test was carried out by verifying that both the structure and the dynamics remain unchanged during each acquisition.

3.3. αS above a critical surface density disrupts SSLB aggregates

Curvature enforced and highly charged DOPC:DOPA (1:1) SSLBs on nanoparticles (obtained from a lot whose average particle diameter was 58 nm), mimicking the two biophysical characteristics of synaptic vesicles, were used as a model system to investigate the effect of αS binding on intermembrane interactions. In physiological HB7 buffer absent αS, the scattering of SSLBs showed direct evidence for a spherical form factor with some interparticle correlation (see black curve on Fig. 3.5) reminiscent of scattering from particles existing in a high volume fraction shown in Fig. 3.3. The interparticle correlation peak occurred at the value of $q \sim 0.0095$ Å^{-1} corresponding to a real space distance of ~66 nm, approximately the distance expected of two SSLBs making nearest-neighbor contact in solution. The SAXS data were unsurprising for the fact that we knew SSLBs in salty buffer (> 100 mM salt) are in some aggregated state (see Table 2.3).

However, a different scattering profile was obtained when αS was titrated into solution. As a function of increasing protein-to-lipid ratio, the correlation peak was suppressed and entirely disappeared at and above 1 protein to 107 outer leaflet lipids (Φ = 1/107) (Fig. 3.5) while the spherical form factor remained consistent. This suggested that for sufficient surface density the membrane bound αS entirely disrupted the attractive inter-SSLB attraction.

This initial result subsequently prompted efforts in two directions: (1) SSLB dynamics as a function of αS (Chapter 3.4), (2) depletion force response experiments to quantitate intermembrane force in presence of αS (Chapter 4).

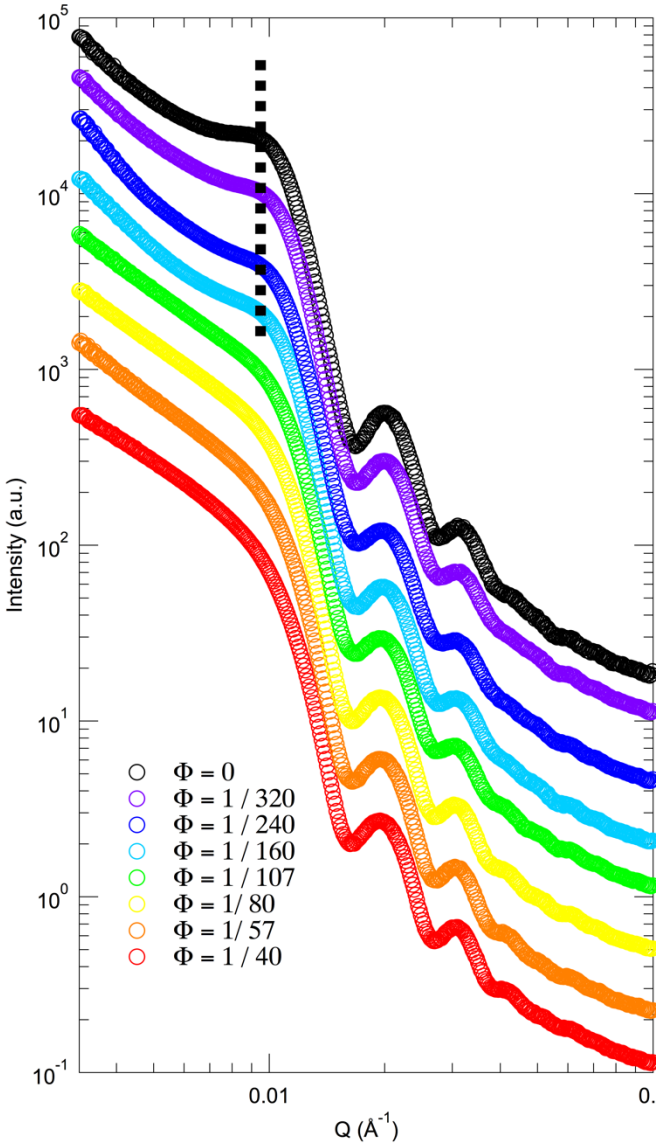

Fig. 3.7. αS above a critical surface density disrupts SSLB aggregates. Azimuthally-averaged SAXS data reveals that without αS or at low concentration of αS (protein to outer lipid ratio Φ = 1/320, 1/240, 1/160), SSLBs show a correlation peak (top line profile) at low scattered wavevector Q (~ 0.0095 Å^{-1}) consistent with nearest-neighbor spacing of SSLBs. However, upon the addition of increasing protein this correlation peak is suppressed, suggesting that αS disrupts interactions between the spatially-correlated SSLBs. Reproduced from ref. (19).

3.4. Increased SSLB diffusivity upon adsorption corroborates αS induced SSLB steric stabilization

The fact that αS disrupted SSLB aggregates suggests that colloidal diffusion of the sample should also markedly change as a function of protein titration. We used XPCS to investigate these nanoscopic dynamics.

The autocorrelation curves $\Delta g_2(\vec{q}, t)$ were obtained for αS-SSLB complexes in HB7 solutions at multiple protein-to-outer lipid ratios – the same ratios used for SAXS experiments. Remarkably, at all wavevectors examined, the overlay of Δg_2 showed a continuous leftward shift of the curve with increasing addition of αS, up to Φ = 1 protein/107 outer lipids; at and above this ratio, the curves converged (Fig. 3.6).

Having observed the leftward shift indicating a faster diffusivity of SSLBs, we proceeded to calculate SSLB diffusivity and stretched exponential argument for every protein-lipid ratio, and compare them to the expected values for noninteracting spheres (Fig. 3.9). Analysis revealed that the diffusivity approaches the value expected for 70 nm diameter spherical colloids as a function of protein added and the stretched exponential argument approached 1, which would be expected of Brownian motion of SSLBs.

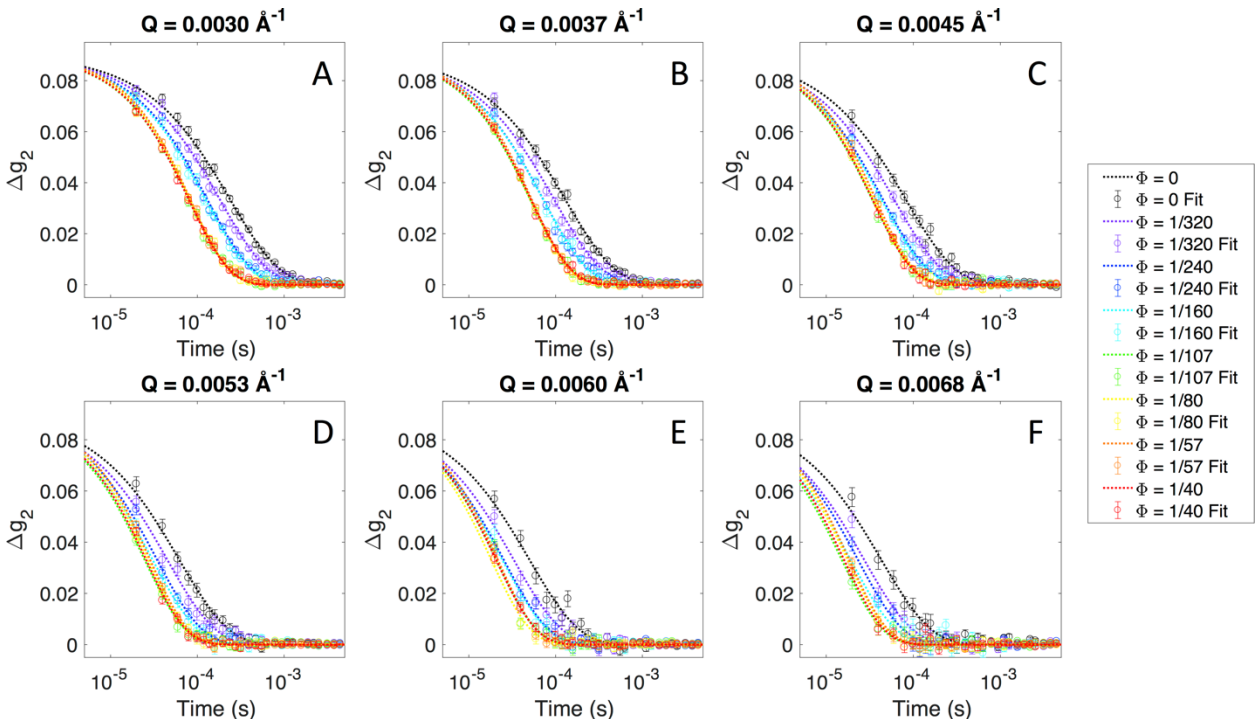

Fig. 3.8. XPCS reveals increasing diffusivity of SSLBs as a function of αS-lipid ratio at all wavevectors examined.
A consistent trend of leftward shift of normalized intensity vs. time autocorrelation functions is observed, as a function of αS surface density. The leftward shift indicates increased SSLB diffusivity conferred by protein binding. The curves collapse at Φ = 1/107 and higher ratios at all examined wavevectors: (*A*) Q = 0.0030 Å^{-1}, (*B*) Q = 0.0037 Å^{-1}, (*C*) Q = 0.0045 Å^{-1}, (*D*) Q = 0.0053 Å^{-1}, (*E*) Q = 0.0060 Å^{-1}, and (*F*) Q = 0.0070 Å^{-1}. The consistency in behavior at all wavevectors indicates αS induced increase in diffusivity is not an artifact of a chosen length scale. Adapted from ref. (19).

Importantly, the change in diffusivity corroborates the SAXS data that showed interparticle correlation disappeared at and above Φ = 1/107 ratio. Moreover, the binding data from ITC revealed a saturating surface density of 1 protein per 91 outer leaflet lipids, which is a good agreement with the critical protein-lipid ratio found with SAXS and XPCS measurements, and a further validation that the steric stabilization effect is due to the bound protein.

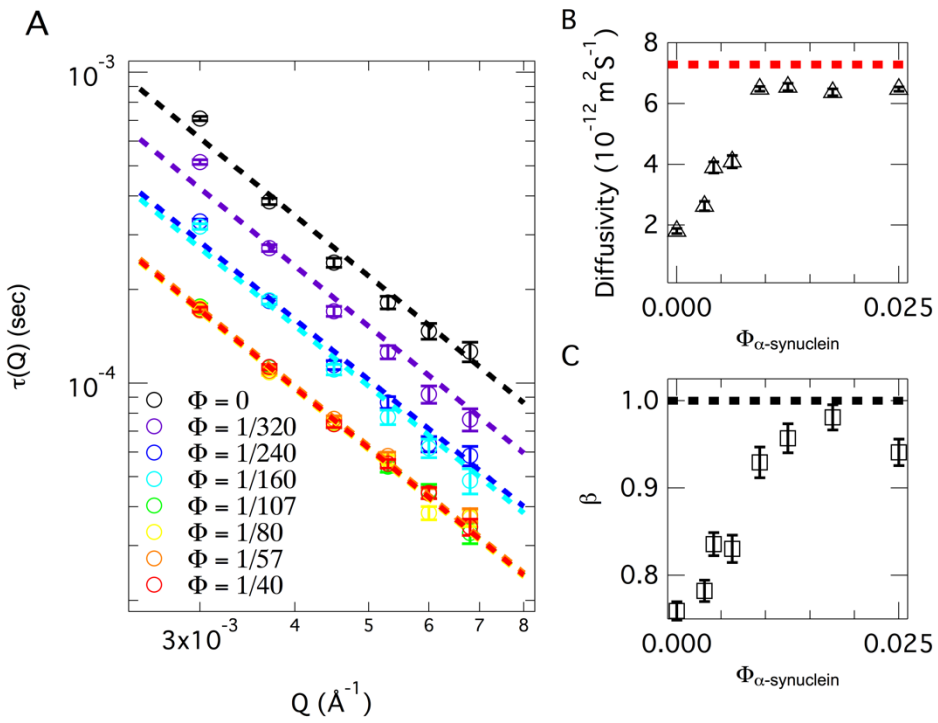

Fig. 3.9. Analysis of XPCS data reveals αS restores expected Brownian diffusion of SSLBs.
(A) Relaxation time plotted as a function of scattered wavevector indicates an expected power law decay (~q^{-2}) for all added concentrations of αS with expected collapse at protein to outer leaflet lipid ratio Φ = 1/107.
(B) The diffusivity of our SSLBs plotted at a function of increasing Φ approaches the expected Brownian diffusivity of a 70-nm diameter spherical colloid (red-dashed line for reference).
(C) The stretch parameter β approaches Brownian diffusive behavior ($\beta = 1$, black-dashed line) with increasing Φ, implying that increasing α-Synuclein coverage inhibits sub-diffusive motion of weakly-correlated "naked" SSLBs. Reproduced from ref. (19).

3.5. A globular protein of similar size does not show the same stabilization behavior

We wondered whether the steric stabilization behavior was a unique result coming from the supposed polymeric properties of αS and not just a generic effect coming from a lipid binding protein of similar size. We used lysozyme, a small (14.4 kDa), cationic and well-folded globular protein that is known to bind lipids. Similar to how we proceeded with αS experiments, we first confirmed lysozyme does not affect the membrane integrity of SSLBs (Fig. 3.10A) and examined the SAXS of lysozyme-SSLB complexes at a high, surface saturating concentration of protein (1 lysozyme to 80 outer leaflet lipids).

The TEM and SAXS results were in direct contrast to what we observed with αS. Lysozyme noticeably aggregated DOPC:DOPA (1:1) SSLBs, showing a pronounced correlation peak at nearest-neighbor distance (Fig. 3.10B). This result implied that the globular nature of lysozyme does not confer steric stabilization of SSLBs and the lysozyme's positively charged residues probably attracted the SSLBs. The structural properties of αS (partially disordered polymeric structure of membrane bound αS) indeed account for the colloid stabilizing behavior as detailed in the next chapter where structure-specific nature of this stabilization is studied.

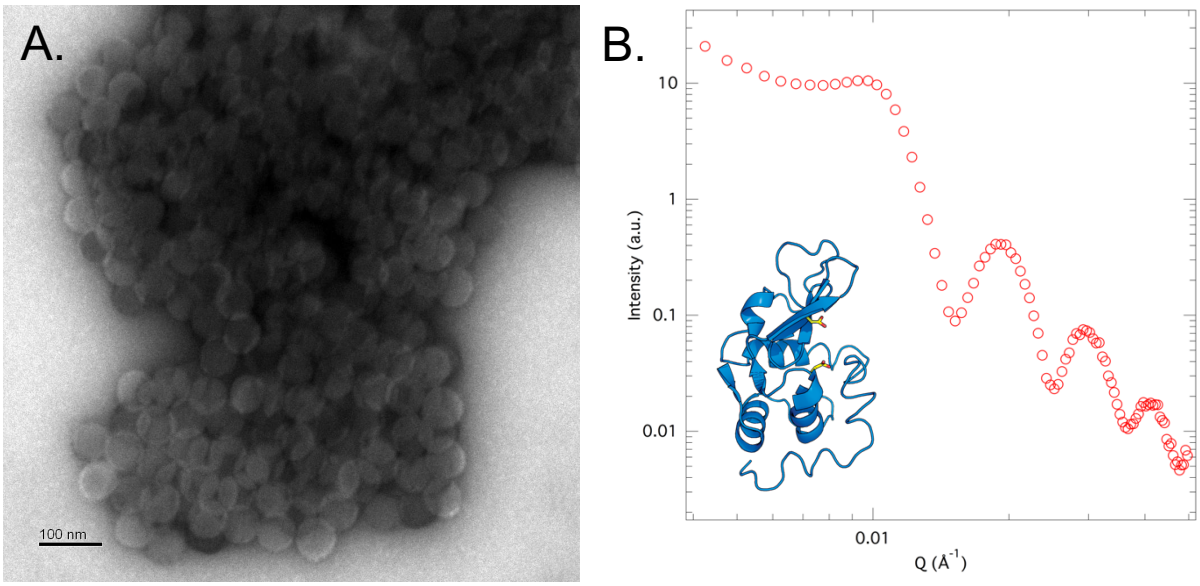

Fig. 3.10. Lysozyme aggregates the SSLBs.
(A). Under whole-mount transmission electron microscopy, it is readily apparent that lysozyme, a cationic protein with similar mass (MW = 14.4 kDa) to αS aggregates SSLBs while keeping the lipid bilayer (the bright concentric rings around each nanoparticle) intact. Scale bar: 100 nm.
(B). SAXS reveals that addition of lysozyme to SSLB solutions does not suppress the correlation peak. Azimuthally-averaged SAXS data reveals that in adding lysozyme (at similar concentrations to αS, protein to outer lipid ratio Φ = 1/80) to SSLB solutions does not suppress the correlation peak at low scattered wavevector Q (~ 0.0092 Å^{-1}) consistent with nearest-neighbor spacing of SSLBs. Inset is a 3-D PyMol rendered structure of lysozyme. Adapted from ref. (19).

3.6. The biological contextualization of αS induced steric stabilization

We return to the question of possible biological context for steric stabilization of synaptic vesicles via αS adsorption. Synaptic vesicles both directly and indirectly interact with other membrane surfaces to effect their biological function. Within the neuron they remain in clustered pools within some protein scaffold and must be released from the pools to fuse to the neuronal membrane.[5,6] If binding density to synaptic vesicles residing in pools were precisely controlled in some way, the αS binding-induced steric stabilization may detach the vesicles from the pools and mobilize them to the site of synaptic vesicle fusion. Could it be that *selective* αS membrane binding is a way for neurons to regulate

synaptic vesicle release? This hypothesis is supported by both *in vivo* findings involving synuclein knockout or overexpression mice and *in vitro* biophysical findings. In synucleins-knockout mice, an increase in synaptic vesicle clustering was shown by imaging the ultrastructure of the presynaptic terminal.[20] This suggests that without αS bound on synaptic vesicles, the active release (or declustering) of vesicles may be reduced. In the opposite limit, the overexpression of αS in mice inhibited synaptic vesicle re-clustering after endocytosis and reduced neurotransmitter release.[21] Put another way, high surface density of αS may prevent the colloidally stabilized vesicles from being cycled back to clustered pools. In an *in vitro* system of SUVs and SNARE protein machinery, SUV fusion mediated by SNARE was inhibited by a high binding density of αS.[22] The sterically repulsive tails may prevent the approach of membrane surfaces or correct positioning of SNARE complex to carry out its function. These lines of evidence point to a larger role of αS binding and in particular the disordered C-terminal domain in the overall regulation of synaptic vesicles.

Because the surface *density* of αS on vesicle dictates the degree of steric stabilization, it would be important to know this number and distribution in the actual physiological setting. The general difficulty in obtaining this data lies in the purification protocol of synaptic vesicles – whereby harsh solution conditions likely remove the bound αS from the surface – but one study found out that the most probable value is 70 αS per a synaptic vesicle.[23] However as shown in Fig. 3.11 this value has a fairly large distribution going up to > 300 per vesicle, suggesting that αS surface density is inherently inhomogeneous and this number may indicate the concomitant functional state of the synaptic vesicle — neurotransmitter unloaded vs. readily releasable vs. released.

Moreover, the number of 70 αS per vesicle significantly exceeds the density of other synaptic proteins found on the surface, for whom the typical copy number is 1-10 per vesicle.[23] This suggests that the predominant contribution for steric stabilization of synaptic vesicles indeed results from the density of αS, rather than other surface bound proteins. Possible reasons for binding inhomogeneity are explored in Chapter 5.

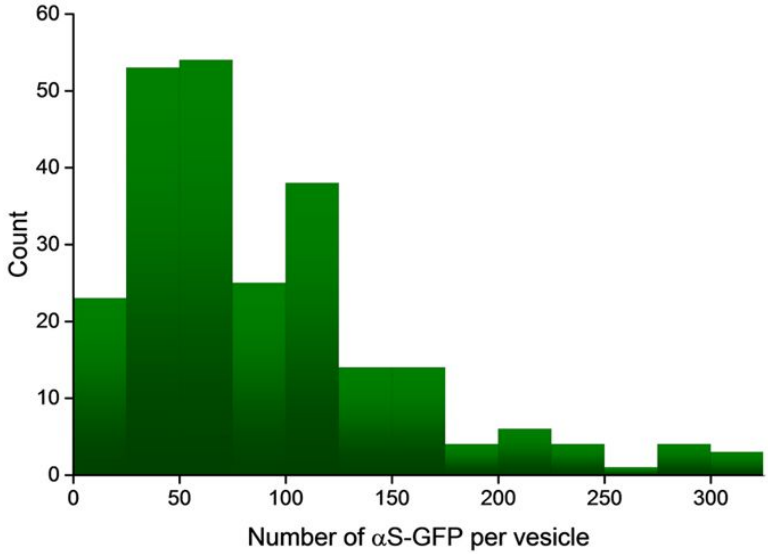

Fig. 3.11. The distribution of αS-GFP per vesicle quantitated through single molecule fluorescence.
Single molecule imaging and photobleaching experiments using confocal microscopy in differentiated SH-SY5y cell line revealed that the most frequent number of GFP tagged αS per synaptic vesicle is 70 (proteins are approximately ~10 nm apart), which corresponds to a molar ratio of 250 total lipids per protein. This value is close to the critical density needed for steric stabilization that we obtained in our experiments: 107 outer lipids per protein. Adapted from ref. (23).

3.7. References

(1) Snead, D.; Eliezer, D. Intrinsically Disordered Proteins in Synaptic Vesicle Trafficking and Release. *J. Biol. Chem.* **2019**, *294* (10), 3325–3342. https://doi.org/10.1074/jbc.REV118.006493.

(2) Lashuel, H. A.; Overk, C. R.; Oueslati, A.; Masliah, E. The Many Faces of α-Synuclein: From Structure and Toxicity to Therapeutic Target. *Nat. Rev. Neurosci.* **2013**, *14*, 38–48. https://doi.org/10.1038/nrn3406.

(3) Deleersnijder, A.; Gerard, M.; Debyser, Z.; Baekelandt, V. The Remarkable Conformational Plasticity of Alpha-Synuclein: Blessing or Curse? *Trends Mol. Med.* **2013**, *19* (6), 368–377. https://doi.org/10.1016/j.molmed.2013.04.002.

(4) Fusco, G.; De Simone, A.; Gopinath, T.; Vostrikov, V.; Vendruscolo, M.; Dobson, C. M.; Veglia, G. Direct Observation of the Three Regions in α-Synuclein That Determine Its Membrane-Bound Behaviour. *Nat. Commun.* **2014**, *5* (1), 1–8. https://doi.org/10.1038/ncomms4827.

(5) Rizo, J.; Rosenmund, C. Synaptic Vesicle Fusion. *Nat. Struct. Mol. Biol.* **2008**, *15* (7), 665–674. https://doi.org/10.1038/nsmb.1450.

(6) Rizo, J.; Xu, J. The Synaptic Vesicle Release Machinery. *Annu. Rev. Biophys.* **2015**, *44* (1), 339–367. https://doi.org/10.1146/annurev-biophys-060414-034057.

(7) Milovanovic, D.; Wu, Y.; Bian, X.; De Camilli, P. A Liquid Phase of Synapsin and Lipid Vesicles. *Science* **2018**, *361* (6402), 604–607. https://doi.org/10.1126/science.aat5671.

(8) Israelachvili, J. *Intermolecular and Surface Forces*; Elsevier Inc., 2011. https://doi.org/10.1016/C2009-0-21560-1.

(9) de Gennes, P. G. Polymers at an Interface; a Simplified View. *Advances in Colloid and Interface Science*. Elsevier July 1, **1987**, pp 189–209. https://doi.org/10.1016/0001-8686(87)85003-0.

(10) Kuhl, T. L.; Leckband, D. E.; Lasic, D. D.; Israelachvili, J. N. Modulation of Interaction Forces Between Bilayers Exposing Short-Chained Ethylene Oxide Headgroups. *Biophys. J.* **1994**, *66*, 1479–1488. https://doi.org/10.1016/S0006-3495(94)80938-5.

(11) de Gennes, P. G. Polymer Solutions near an Interface. 1. Adsorption and Depletion Layers. *Macromolecules* **1981**, *14* (6), 1637–1644. https://doi.org/10.1021/ma50007a007.

(12) Dolan, A. K.; Edwards, S. F. Theory of the Stabilization of Colloids by Adsorbed Polymer. *Proc. R. Soc. A Math. Phys. Eng. Sci.* **1974**, *337* (1611), 509–516.

https://doi.org/10.1098/rspa.1974.0063.

(13) Klein, J.; Luckham, P. Forces between Two Adsorbed Polyethylene Oxide Layers Immersed in a Good Aqueous Solvent. *Nature* **1982**, *300* (5891), 429–431. https://doi.org/10.1038/300429a0.

(14) Als-Nielsen, J.; McMorrow, D. *Elements of Modern X-Ray Physics: Second Edition*; John Wiley and Sons: Hoboken, NJ, USA, 2011. https://doi.org/10.1002/9781119998365.

(15) Li, T.; Senesi, A. J.; Lee, B. Small Angle X-Ray Scattering for Nanoparticle Research. *Chemical Reviews*. American Chemical Society September 28, **2016**, pp 11128–11180. https://doi.org/10.1021/acs.chemrev.5b00690.

(16) Weiss, T. Workshop Presentations | Small Angle X-ray Scattering/Diffraction https://www-ssrl.slac.stanford.edu/smb-saxs/content/workshop-presentations (accessed Feb 11, 2020).

(17) Lee, B. SAXS/GISAXS principles https://sites.google.com/site/byeongdu/saxs-principles (accessed Feb 11, 2020).

(18) Leheny, R. L. XPCS: Nanoscale Motion and Rheology. *Current Opinion in Colloid and Interface Science*. February **2012**, pp 3–12. https://doi.org/10.1016/j.cocis.2011.11.002.

(19) Chung, P. J.; Zhang, Q.; Hwang, H. L.; Leong, A.; Maj, P.; Szczygiel, R.; Dufresne, E. M.; Narayanan, S.; Adams, E. J.; Lee, K. Y. C. α-Synuclein Sterically Stabilizes Spherical Nanoparticle-Supported Lipid Bilayers. *ACS Appl. Bio Mater*. **2019**, *2* (4), 1413–1419. https://doi.org/10.1021/acsabm.8b00774.

(20) Vargas, K. J.; Schrod, N.; Davis, T.; Fernandez-Busnadiego, R.; Taguchi, Y. V.; Laugks, U.; Lucic, V.; Chandra, S. S. Synucleins Have Multiple Effects on Presynaptic Architecture. *Cell Rep*. **2017**. https://doi.org/10.1016/j.celrep.2016.12.023.

(21) Nemani, V. M.; Lu, W.; Berge, V.; Nakamura, K.; Onoa, B.; Lee, M. K.; Chaudhry, F. A.; Nicoll, R. A.; Edwards, R. H. Increased Expression of α-Synuclein Reduces Neurotransmitter Release by Inhibiting Synaptic Vesicle Reclustering after Endocytosis. *Neuron* **2010**, *65* (1), 66–79. https://doi.org/10.1016/j.neuron.2009.12.023.

(22) Dewitt, D. C.; Rhoades, E. α-Synuclein Can Inhibit SNARE-Mediated Vesicle Fusion Through Direct Interactions with Lipid Bilayers. *Biochemistry* **2013**, *52* (14), 2385–2387. https://doi.org/10.1021/bi4002369.

(23) Fakhree, M. A. A.; Zijlstra, N.; Raiss, C. C.; Siero, C. J.; Grabmayr, H.; Bausch, A. R.; Blum, C.; Claessens, M. M. A. E. The Number of α-Synuclein Proteins per Vesicle

Gives Insights into Its Physiological Function. *Sci. Rep.* **2016**. https://doi.org/10.1038/srep30658.

CHAPTER 4.

THE STRUCTURAL ORIGIN OF α-SYNUCLEIN INDUCED STERIC STABILIZATION: THE ROLE OF THE DISORDERED C-TERMINAL DOMAIN

4.1. Overview: Probing the depletion force response of αS bound SSLBs revealed an important structure-property relationship

The question posed in the preceding chapter — how does αS, once membrane bound, mediate interactions of apposing membrane surfaces? — was addressed initially by showing that membrane adsorption of αS disrupted interparticle SSLB attraction above a critical surface density.[1] But to what extent, and how its membrane bound structure leads to observed steric stabilization remains unanswered. These questions are pursued in this chapter by quantitating the intermembrane repulsive force and resolving the role of disordered domain in this phenomenon, accomplished via depletion force response experiments.

Here we focus our attention on the last 40 residues — the disordered C-terminal domain. Order parameters from independent NMR experiments have definitively shown that this domain remains disordered even upon membrane binding.[2–4] In Chapter 3, one important but overlooked property of the C-terminal domain was its highly acidic nature. Of the last 40 residues of αS (amino acid sequence 101-140: GKNEEGAPQEGIL EDMPVDPDNEAYEMPSEEGYQDYEPEA), 14 are either aspartic acid or glutamic acid, both of which carries a –1 charge at pH 7. The density of anionic residues suggests that, in addition to the polymeric nature, charge-charge repulsion between C-terminal chains may have to do with steric stabilization. It also follows that the highly acidic polymeric tail may be remarkably sensitive to the amount of salt and divalent ions in solution, modulating the apposing membrane interactions. The combination of SAXS

measurements here, spanning the parameter space of depletion force, salt, and reversibility, examines membrane-bound αS as charged polymer projecting from the membrane surface and establishes the polyelectrolytic behavior of the C-terminal domain on membrane. Measurements of truncated protein (αSΔCTD), missing the residues 102 through 140, are presented as confirmatory evidence that this domain is primarily responsible for steric stabilization of membrane surfaces. The significance of persisting disorder of αS even upon membrane binding is placed in the context of the disease state of the protein which is truncated and found in Lewy bodies. Moreover, the sensitivity of the domain to Ca^{2+} ions, which can increase to hundreds of μM in presynaptic terminals,[5,6] suggests finely tuned and dynamically regulated αS-stabilization effect and synaptic vesicle homeostasis in the neuron. The implications of C-terminal domain mediated steric stabilization are contextualized with the recent *in vitro* and *in vivo* data that explore the effects of C-terminus truncation.[7,8]

4.2. Materials and Methods

4.2.1. Materials

Materials including DOPC, DOPA, aqueous buffer components, and amine-functionalized 60 nm silica nanoparticles were purchased and used for preparation of DOPC:DOPA (1:1, mol%) SSLBs. N-terminally acetylated αS was expressed and purified as detailed in Chapter 2.2. PEG with an average molecular weight of 10,000 g/mol (PEG10k) was purchased from Sigma Aldrich.

4.2.2. C-terminal domain truncated αS (αSΔCTD) purification

In this work, the truncated protein αSΔCTD retains residues 1 to 101 of the full length αS. Following the bacterial expression and cell lysis steps detailed in Chapter 3.2, acid precipitation was used for purification. By addition of 10 M HCl, pH of the lysate was adjusted to 3.5 and sample was centrifuged at 20,000*g* for 20 minutes. After re-adjusting the pH of the supernatant to 7.0, ammonium sulfate precipitation was induced by adding the salt to 50 wt./vol %. The sample was centrifuged again at 20,000*g* for 20 minutes. The lysate was run through a HiTrap Q FF anion exchange column (GE Healthcare Lifesciences). αSΔCTD was captured in the flow due to its highly cationic nature. αSΔCTD was then filtered and run through a Superdex 200 10/300 column (GE Healthcare Lifesciences), eluting at 14.5 mL into sample buffer, HB7. Protein concentration was measured on NanoDrop (Thermofisher Scientific) at predicted absorbance (A_{280} - coefficient = 1490), aliquoted, and frozen in liquid nitrogen until further use.

4.2.3. PEG induced depletion for force response experiments

The premise of force response experiments is that protein-bound SSLBs, which are sterically stabilized by the presence of protein, are forced to approach each other via increasing depletion force to the point of inducing "structure" or nearest-neighbor SSLB interaction (Fig. 4.1). The critical depletion force (or osmotic pressure) required to carry out this transition is calculated for a variety of protein, SSLB, and solution states, allowing us to tease out the important parameters involved in SSLB clustering. This kind of depletion force response experiments, first demonstrated with DNA double helices to measure their intermolecular force,[9] allows for an application of force via straightforward addition of depletant and measurement of accompanying structural changes via SAXS.

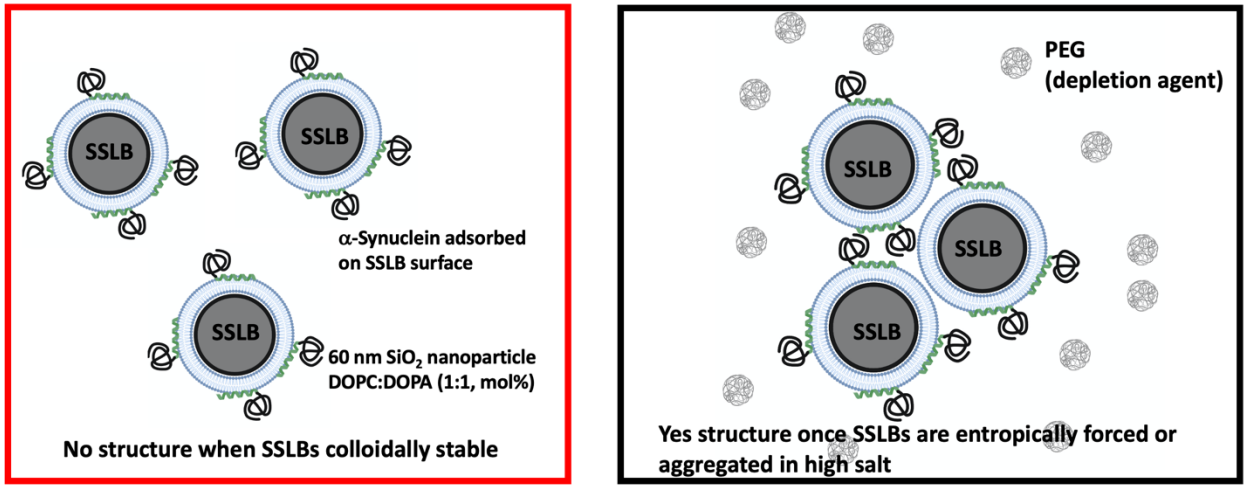

Fig. 4.1. Schematic of force response experiments with αS-SSLBs.
DOPC:DOPA (1:1 mol%) SSLBs bound with αS (at 1 protein per 80 outer leaflet lipids) are forced to aggregate as a function of PEG10k depletant concentration, which can be related to osmotic pressure as shown on Equation (4.1). The critical pressure needed to induce nearest neighbor αS-SSLB correlation (as evidenced by SAXS correlation peak) is recorded for a range of salt conditions for both full-length and truncated forms of αS.

The force response SAXS experiments were performed with protein-bound DOPC:DOPA (1:1) SSLBs in presence of PEG, a non-interacting depletion agent. In presence of much larger colloids (SSLBs), PEG polymers are depleted in the interfacial zone between larger colloids that are in such close proximity to one another that PEG is forced to explore the configurational space outside of that zone — also known as "excluded volume". The preferential separation of PEG from SSLBs produces an entropically driven attraction between SSLBs. If the attraction is stronger than repulsion effected by bound protein, SAXS will show interparticle correlation (Fig. 4.1). It should be noted that these PEG experiments can also mimic the macromolecular crowding conditions found within the cell, adding an important feature absent in most biochemistry experiments where dilute conditions are the norm.

For sample preparation, SSLBs (20 μL at 2 mg/mL SiO_2 particle concentration), protein (αS or αSΔCTD), PEG at a chosen concentration, HB7, and a stock of 10 mM $CaCl_2$

or $MgCl_2$ solution in HB7 were mixed at appropriate volume ratios to produce 50 μL solution which was then loaded into 1.5 mm quartz capillaries (Hampton Research, Aliso Viejo, CA, USA). SAXS of αS-SSLBs at equilibrium was taken at beamline 4-2 at SSRL as detailed in Chapter 3.2.3. Osmotic pressure was calculated from PEG concentration using the following empirically obtained virial expansion.[10]

$$P = RT\left(\frac{10}{[\text{MW of PEG}]}[\text{PEO wt./vol\%}] + 1.4 \times 10^{-5} \times [\text{PEO wt./vol\%}]^2 + 2.0 \times 10^{-5} \times [\text{PEO wt./vol\%}]^3\right) \quad (4.1)$$

4.3. The presence of C-terminal domain is critical to SSLB steric stabilization

Following the successful αSΔCTD purification, the first measurements were aimed at obtaining binding data via ITC and verifying the structural integrity of αSΔCTD-bound SSLBs (Fig. 4.2). The truncated form compared to the full-length showed approximately two-fold increased binding to DOPC:DOPA (1:1) SSLBs with k_D = 42 μM, but notably it dispersed SSLB aggregates without compromising the membrane integrity, at the saturating protein-to-outer leaflet lipid ratio of Φ = 1:80. This shows that even without the C-terminal domain, the αS imparts some repulsive steric effect between membranes.

Given the αSΔCTD data, we then hypothesized that the presence of C-terminal domain would dramatically increase the inter-SSLB repulsion. In order to test this, we incubated αS-SSLBs in separate glass capillaries with different concentrations of PEG and recorded SAXS at equilibrium, to assess nearest neighbor correlation as a function of depletion attraction. Fig. 4.3 shows that at and above PEG10k concentration of 10.5 wt./vol %. (equivalent to 1.3×10^5 Pa), the SSLBs were found to be correlated, meaning that the repulsive αS-SSLB interaction was overcome by PEG induced depletion force at

the critical clustering pressure of $P_c = 1.3 \times 10^5$ Pa. This is close to two orders-of-magnitude increase in $P_c \sim 4 \times 10^3$ Pa required to correlate noninteracting gold colloidal spheres that are 70 nm in diameter.[11] An example of how the αS-SSLB samples appeared in capillaries is shown in Fig. 4.4.

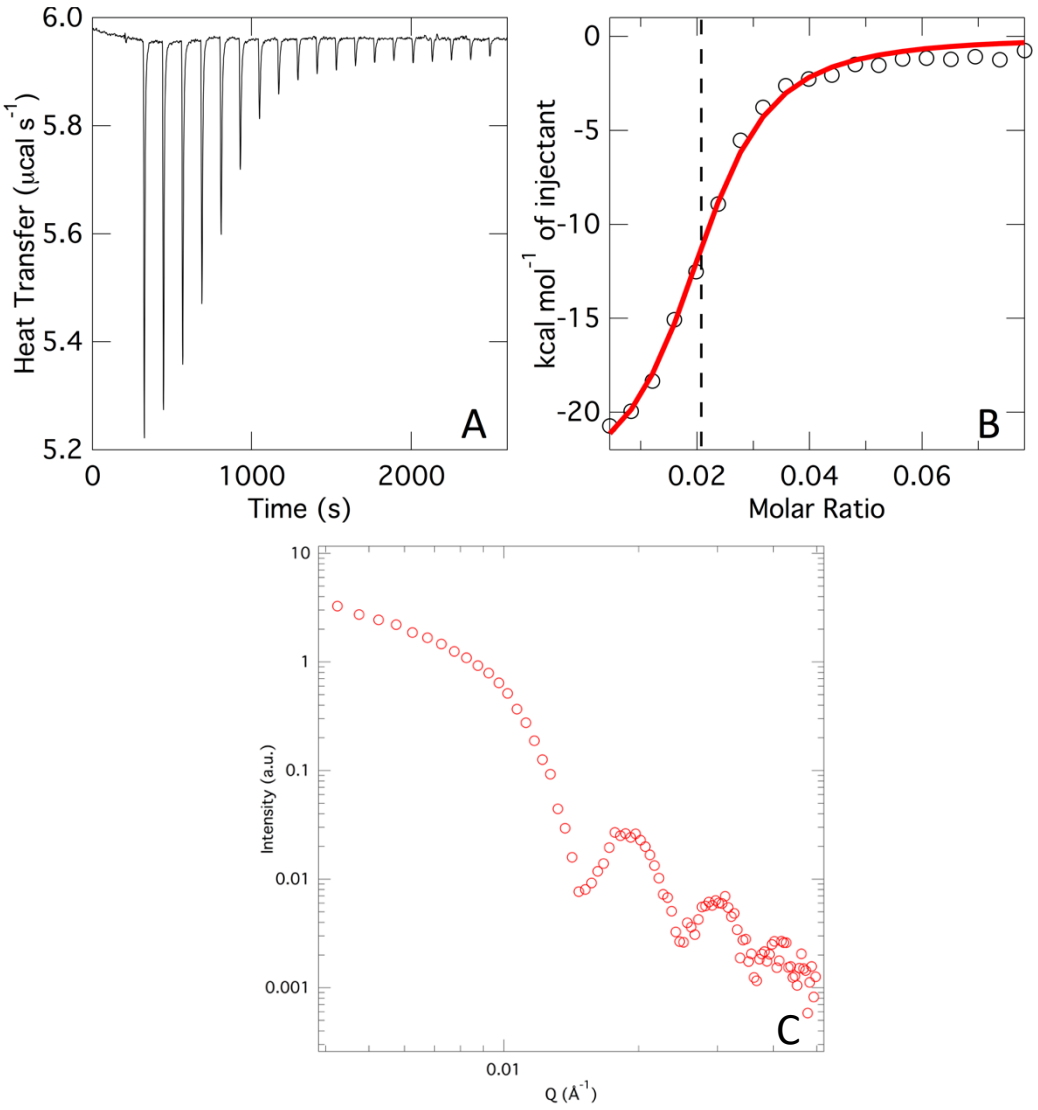

Fig. 4.2. Characterization of αSΔCTD binding and steric stabilization.
(A, B). ITC measurements (see Chapter 2.2 for protocol) using αSΔCTD revealed that the protein bound with an apparent dissociation constant k_D = 42 μM at a binding stoichiometry of 1 protein for every 46 outer leaflet lipids.
(C). SAXS of αSΔCTD bound SSLBs shows that the nearest neighbor interparticle correlation peak is suppressed due to bound protein. This result suggests that the binding

of N-terminal domain (without the disordered domain) does confer repulsive intermembrane potential to some extent.

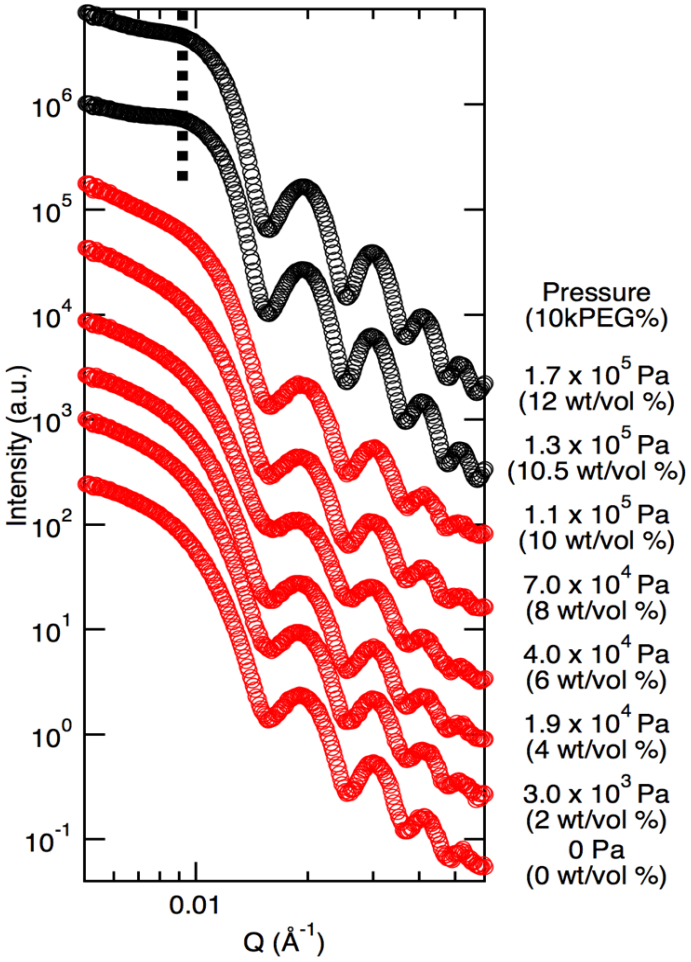

Fig. 4.3. Finding the critical osmotic pressure for SSLB correlation as a function of PEG10k concentration.
For DOPC:DOPA (1:1 mol%) SSLBs coated with Φ = 1:80 (1 protein per 80 outer leaflet lipids) coverage, the amount of PEG concentration required to induce the nearest neighbor SSLB correlation occurred at [PEG10k] = 10.5 wt./vol. %, corresponding to 1.3×10^5 Pa. At and above this critical pressure, the repulsion between αS-SSLBs was overcome by the depletion attraction. The critical pressure was examined for truncated αS and a wide range of salt conditions.

For αSΔCTD, however, the critical pressure for αS-SSLB correlation occurred at a much lower value of 1.9×10^4 Pa ([PEG10k] = 4 wt./vol. %), about seven times less than the critical clustering pressure of SSLBs complexed with full length αS (Fig. 4.5, left panel).

Thus, the presence of the C-terminal domain did significantly increase the pressure required to cluster the SSLBs.

There was a correspondence between the presence of a correlation peak and the visual observation of sample in capillaries. Where we observed sample correlation peak, we also observed the appearance of cloudy aggregates in solution reflecting the PEG induced αS-SSLBs aggregation (Fig. 4.4). The 12 wt.% PEG10k sample at 1 M NaCl, for instance, showed aggregates and subsequent pellet formation in the capillary while the rest of the capillaries showed clear solutions. XPCS used in Chapter 3 was able to tease out SSLB diffusion even after the sample aggregated and settled, since X-ray wavelength is not subject to the multiple scattering effects encountered when using dynamic light scattering with optical wavelengths.

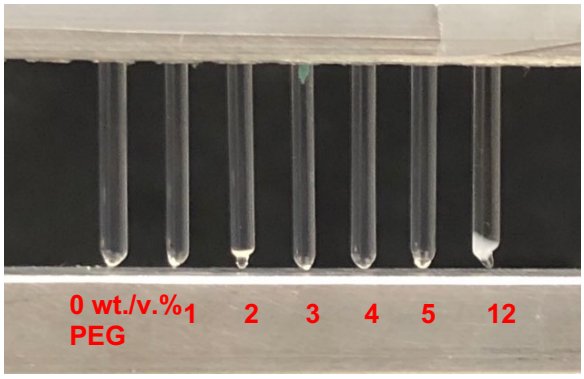

Fig. 4.4. Visual observation of PEG-induced pellet matched the presence of correlation peak in the sample.
An example image of quartz capillaries containing increasing wt./vol. % of PEG (0, 1, 2, 3, 4, 5, and 12) at 1 M NaCl condition. In particular, the sample with a SAXS correlation peak (12 wt./vol. % PEG) had a distinct appearance of cloudy aggregates. (Note that in 0, 1, 2, 3, 4, and 5 wt./vol. % PEG capillaries what appears to be aggregates at the bottom of glass capillaries are reflections from the glass.)

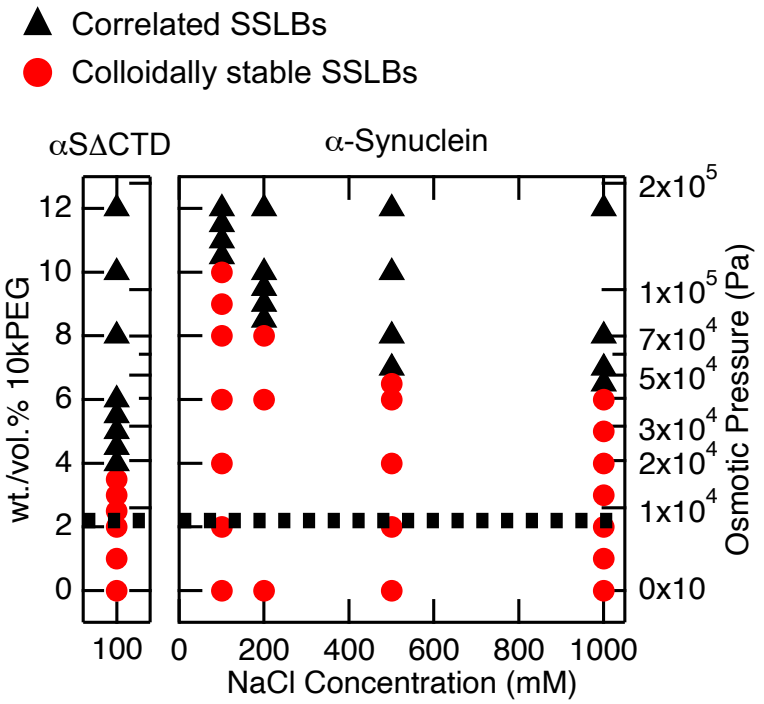

Fig. 4.5. The depletion force induced clustering of αS-SSLBs is dependent on C-terminal domain and electrostatic screening of its anionic residues
Two phases of αS-SSLBs were mapped out as a function of [NaCl] and wt./vol.% PEG10k. For full length αS, the critical pressure at which the SSLBs transitioned from sterically stable to correlated states was found for each of the following NaCl concentrations: 100, 200, 500, and 1000 mM. For truncated αS, this pressure was found for 100 mM NaCl (left panel). The comparison of two forms of αS (at 100 mM NaCl and same Φ) reveals seven-fold reduction in osmotic pressure needed to correlate SSLBs for the truncated form ($P_c = 1.3 \times 10^5$ Pa reduced to 1.9×10^4 Pa). The reduction of critical pressure for higher NaCl conditions revealed the electrostatics component of αS induced steric stabilization. The dotted line indicates pressure needed to correlate 70 nm colloidal spheres.

4.4. Electrostatic and steric contributions from C-terminal domain enable stabilization

As the truncated form showed significant reduction of critical clustering pressure, we proceeded to examine the parameters governing how the domain affects steric stabilization. First, increasing the monovalent salt (NaCl) concentration in solution screened the anionic charges contained in the C-terminal domain, allowing us to examine the effect of electrostatics in αS-SSLB force response. As shown in the phase diagram (Fig.

4.5), the critical pressure for clustering αS-SSLBs clearly decreased as a function of salt concentration, reflecting the decreased electrostatic screening length and therefore decreased repulsion between αS chains from apposing surfaces. At 1 M NaCl where the Debye length is sub-nanometer at ~ 0.3 nm and the repulsion is only steric in nature, the critical pressure was $P_c = 4.6 \times 10^4$ Pa, which is approximately a three-fold reduction from 100 mM NaCl for full-length αS and a two-fold increase in pressure from 100 mM NaCl for αSΔCTD. Therefore, the force response measurements suggest that the electrostatic and steric contributions are roughly equally important and clearly manifest in αS-induced stabilization.

Next, the polymeric nature of disordered domains was assessed. The C-terminal domains from apposing surfaces do not want to interpenetrate because of the high entropic cost of doing so, unless if they are *forced* to do so via depletion force. If the domains do initially interpenetrate but depletion force is subsequently reduced in a drastic fashion, the domains would disentangle and αS-SSLBs would again be sterically stabilized. When we initially induced αS-SSLB clustering under the 100 mM NaCl condition at $P_c = 1.3 \times 10^5$ Pa, and then diluted the PEG concentration by a factor of two by addition of HB7 buffer, the nearest neighbor correlation was lost (Fig. 4.6), indicating that the process is *reversible* by modulating the depletion force. This observation is consistent with non-specific steric repulsion of grafted polymers on opposing surfaces.[12,13] The reversibility of this phenomenon demonstrates the polymeric nature of disordered domain.

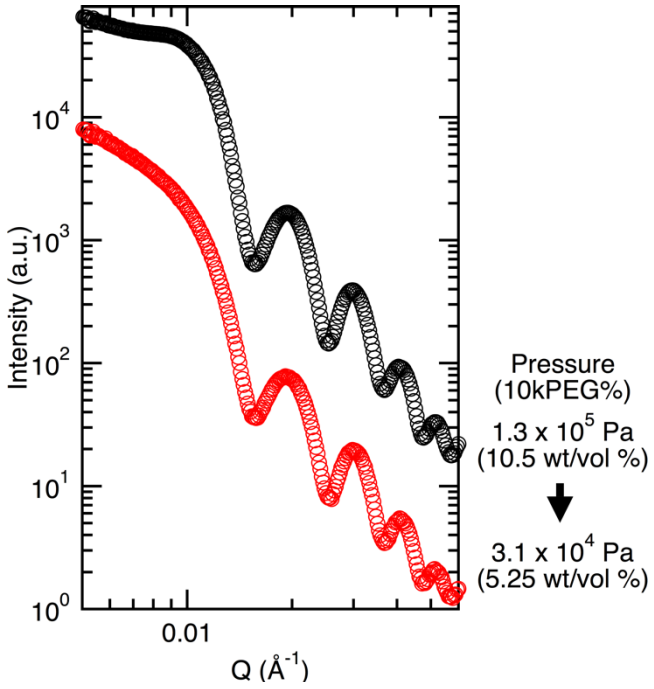

Fig. 4.6. Reduction of depletion force reversibly de-clusters αS-SSLBs
Depletion force induced αS-SSLB clustering is reversible. First, the αS-SSLBs were forced to cluster by addition of 10.5 wt/vol % of PEG10k. By adding in HB7 buffer and simply diluting the PEG in sample by half, the correlation peak disappeared. This reversible behavior is consistent with polymeric behavior of C-terminal domain and reversible flocculation of αS-SSLBs.

4.5. SSLB force response is sensitive to divalent ions in solution

The highly charged nature of the C-terminal domain implies divalent ion interactions and possible effects on αS-SSLB force response. Ca^{2+} ions have been known as a physiologically relevant binding partner for the C-terminal domain and a possible agent for clustering of synaptic vesicles in mM concentrations.[14,15] The reported affinity of Ca^{2+} for the domain is not well known but probably on the range of ~20 μM, with 6-8 ions binding one domain.[14] We hypothesized that the divalent cations neutralize the anionic charges of the C-terminal domain and subsequently weaken αS induced steric stabilization.

First, we checked that αS-SSLBs preserved membrane integrity in presence of 0-3 mM Ca^{2+} (and also Mg^{2+}) with negative stain TEM since Ca^{2+} is involved in membrane bridging and fusion, and found that he presence of divalent ions at the tested levels did not affect the integrity of SSLBs (Fig. 4.7). Then we assessed the critical clustering pressure as a function of divalent ion concentration. As hypothesized, force response measurements showed decreasing critical clustering pressure as a function of increasing [Ca^{2+}] or [Mg^{2+}], with Ca^{2+} imposing a more drastic response (Fig. 4.8). This suggested that divalent ions indeed play a role in decreasing electrostatic repulsion between disordered domains and that there is a calcium specific effect on αS mediated steric stabilization. Moreover, in presence of Ca^{2+}, the PEG induced αS-SSLB clustering was not reversible (Fig. 4.9). Ca^{2+} may have a role in coordinating C-terminal domains from opposing membrane surfaces, disallowing reversible clustering.

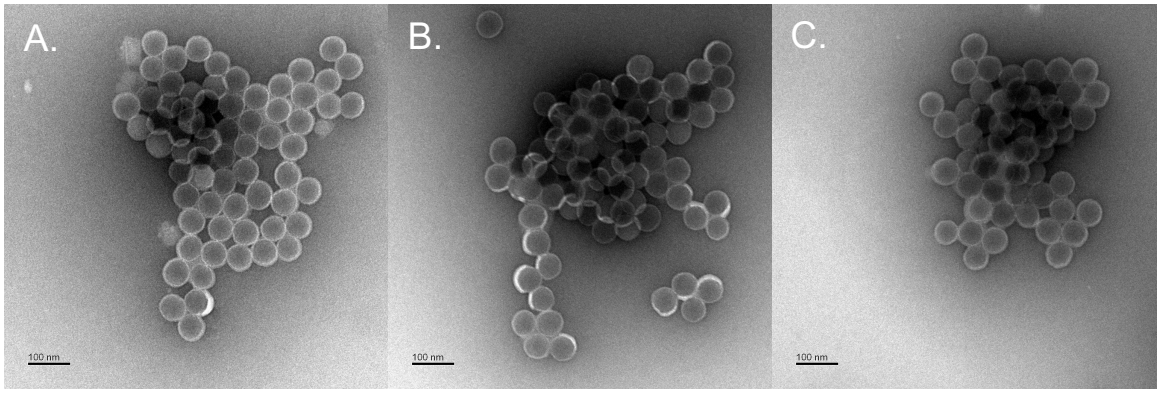

Fig. 4.7. Membrane integrity of αS-SSLBs is preserved in the presence of 3 mM $CaCl_2$ or $MgCl_2$.
(A). Negative stain TEM revealed DOPC:DOPA (1:1) SSLBs retaining the single lipid bilayer shown by 4-5 nm concentric white ring around SiO_2 nanoparticle upon addition of αS (Φ = 1:80)
(B). SSLBs + αS + 3 mM Ca^{2+}
(C). SSLBs + αS + 3 mM Mg^{2+}

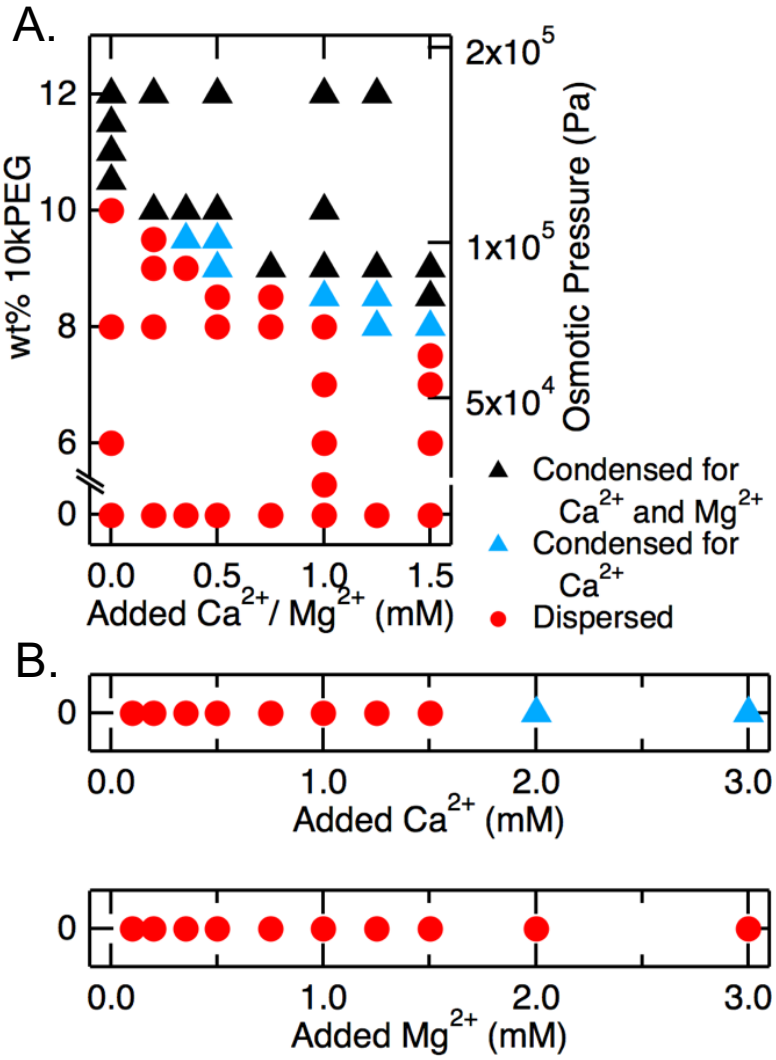

Fig. 4.8. Force response of αS-SSLBs is modified by divalent ions, with Ca^{2+} showing a much higher sensitivity in the μM regime.
(A). Phase diagram of αS-SSLBs (Φ = 1 protein : 80 outer leaflet lipids) shows decreasing critical clustering pressure as a function of increasing Ca^{2+} or Mg^{2+} concentration. The labels show dispersed / sterically stabilized αS-SSLB state (red circle); correlated or condensed state for Ca^{2+} (blue triangle); and condensed state for both Ca^{2+} and Mg^{2+}.
(B). Clustering of αS-SSLBs occurs in presence of Ca^{2+} at and above 2.0 mM, but not Mg^{2+}.

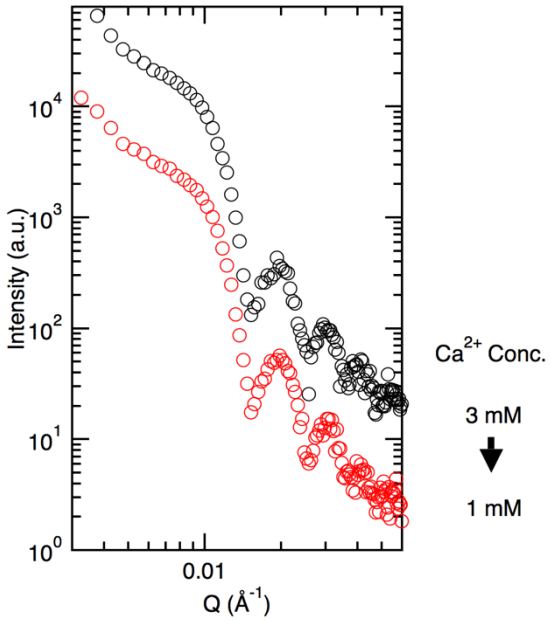

Fig. 4.9. Ca^{2+} induced αS-SSLB clustering is not reversible.
The dilution of Ca^{2+} from 3 to 1 mM Ca^{2+} does not de-cluster αS-SSLBs, suggesting calcium may be binding to the C-terminal domains from apposing membrane surfaces.

4.6. The significance of C-terminal domain in physiology and pathology

In summary, the findings detailed in this chapter clarified the role of the C-terminal domain in conferring steric stabilization in the *in vitro* system of αS, model lipid membranes, and depletion agent. Both the electrostatics and sterics of the domain play important function in its behavior as the C-terminal domain behaves like a grafted polyelectrolyte on the membrane surface. The truncated protein without the domain showed significantly diminished force response, as assessed by reduction in crucial clustering pressure. The steric stabilization was found to be reversible with depletion force, revealing an interaction potential governed by nonspecific steric repulsions of surface-bound polymers. Finally, Ca^{2+} in physiologically relevant sub-millimolar

concentrations noticeably reduced the critical clustering pressure, indicating its importance in modulating interactions between αS bound synaptic vesicles.

In the context of αS-lipid interactions, the N-terminal domain of αS has understandably been the focus of most biophysical experiments since it contains all of the lipid binding residues and the aggregation-prone region. The membrane association, along with the presence of C-terminal domain, has been viewed as a feature inhibiting protein self-association and aggregation, since αSΔCTD is upregulated in familial Parkinson's disease mutations of αS.[16] However, focusing solely on the N-terminal domain cannot reveal why the protein possibly retains some of its intrinsic disorder on membrane binding, and why this may be functionally important for synaptic vesicles that continually cluster, de-cluster, fuse to the cell membrane, and recycle. Coupled with the fact that αS is present in extremely high concentration in the presynaptic terminal and in high copy number on the synaptic vesicle surface (Fig. 3.11), it has been increasingly recognized that understanding its C-terminal domain may be the key to elucidating its physiological role.[4,14,17] In particular, the possibility for this domain to have strong interactions with other protein binding partners has emerged an active area of research, since its functional role (beyond being a chaperone for N-terminal folding) can then be much more clearly defined. If so, αS would be understood as having a more direct presynaptic role rather than a long-term regulatory one.

Ca^{2+} ions, dynamically regulated in the neuron, have been the focus of several studies on C-terminal domain as they can coordinate with its acidic residues. Although we did not directly probe Ca^{2+} binding, we were able to infer how it can alter the properties of C-terminal domain and force response. Reducing Ca^{2+} concentration from 3 to 1 mM

(Fig. 4.9) did not de-cluster αS-SSLBs, implying that Ca^{2+} can potentially bridge C-terminal domains on apposing membrane surfaces or allow the disordered domain to interact with a neighboring lipid surface. Without molecular level resolution a firm conclusion for Ca^{2+} role cannot be stated, but Ca^{2+} clearly mitigates polyelectrolytic behavior and repulsive potential between membrane surfaces. A recent study probing the direct relationship between Ca^{2+} and C-terminal domain found that the domain is in fact amenable to binding lipids of purified synaptic vesicles in the presence of as low as 200 μM Ca^{2+}, and this binding is reversed by the addition of Ca^{2+} chelating EGTA.[14] Given this and our own findings, we speculate a biological picture wherein αS acts to sterically stabilize synaptic vesicles in absence of Ca^{2+} (most likely for synaptic vesicle release from pools) and perhaps to promote intermembrane and protein-protein interactions in presence of elevated local Ca^{2+} concentration.

In contrast to Ca^{2+}, reducing PEG concentration – and therefore reducing the depletion force — certainty resulted in de-clustering of αS-SSLBs. This result pointed to a physical, polymer mediated response, one that is not driven by chemical specificity. This result also suggested that the bridging conformation (Fig. 1.4) of αS, also known as double anchor mechanism, did not form under our experimental conditions. αS sterically stabilized SSLBs in all cases as a function of surface density. The binding of two distinct membrane surfaces would have otherwise prohibited αS-SSLB declustering via dilution of PEG.

The C-terminal domain has been found to have several protein binding partners such as the disordered N-terminus of membrane bound synaptobrevin-2,[18] and Rab proteins, GTPases that catalyze cellular trafficking.[17] These C-terminus-protein

interactions are likely further modulated by post-translational modifications to αS such as acetylation and phosphorylation, which can alter binding affinities, induced structures, and the protein's activity as a chaperone. It is well known that αS can be phosphorylated at Tyr-39, Ser-87, Tyr-125 and Ser-129, with Ser-129 most well-known as the disease implicated modification.[19] Although these mutants were not examined in this work, it would be important to find how these biophysically alter inter-synaptic vesicle interactions — and affect the overall homeostasis of vesicle trafficking.

Lastly, what is interesting about the synuclein family is that the sequence similarity of their C-terminal domain is much lower than that of their N-terminal domain. Compared to αS, β-synuclein has a more proline-rich C-terminal domain, giving it a possibly more compact C-terminus conformation, and γ-synuclein has a much shorter C-terminal domain.[20] The force response for β- and γ-synuclein could differ considerably from αS — yet another possible line of inquiry for future experiments.

4.7. References

(1) Chung, P. J.; Zhang, Q.; Hwang, H. L.; Leong, A.; Maj, P.; Szczygiel, R.; Dufresne, E. M.; Narayanan, S.; Adams, E. J.; Lee, K. Y. C. α-Synuclein Sterically Stabilizes Spherical Nanoparticle-Supported Lipid Bilayers. *ACS Appl. Bio Mater.* **2019**, *2* (4), 1413–1419. https://doi.org/10.1021/acsabm.8b00774.

(2) Bodner, C. R.; Maltsev, A. S.; Dobson, C. M.; Bax, A. Differential Phospholipid Binding of α-Synuclein Variants Implicated in Parkinson's Disease Revealed by Solution NMR Spectroscopy. *Biochemistry* **2010**, *49* (5), 862–871. https://doi.org/10.1021/bi901723p.

(3) Fusco, G.; De Simone, A.; Gopinath, T.; Vostrikov, V.; Vendruscolo, M.; Dobson, C. M.; Veglia, G. Direct Observation of the Three Regions in α-Synuclein That Determine Its Membrane-Bound Behaviour. *Nat. Commun.* **2014**, *5* (1), 1–8. https://doi.org/10.1038/ncomms4827.

(4) Snead, D.; Eliezer, D. Intrinsically Disordered Proteins in Synaptic Vesicle Trafficking and Release. *J. Biol. Chem.* **2019**, *294* (10), 3325–3342. https://doi.org/10.1074/jbc.REV118.006493.

(5) Schneggenburger, R.; Neher, E. Intracellular Calcium Dependence of Transmitter Release Rates at a Fast Central Synapse. *Nature* **2000**, *406* (6798), 889–993. https://doi.org/10.1038/35022702.

(6) Llinás, R.; Sugimori, M.; Silver, R. B. Microdomains of High Calcium Concentration in a Presynaptic Terminal. *Science* **1992**, *256* (5057), 677–679. https://doi.org/10.1126/science.1350109.

(7) Vargas, K. J.; Schrod, N.; Davis, T.; Fernandez-Busnadiego, R.; Taguchi, Y. V.; Laugks, U.; Lucic, V.; Chandra, S. S. Synucleins Have Multiple Effects on Presynaptic Architecture. *Cell Rep.* **2017**, *18* (1), 161–173. https://doi.org/10.1016/j.celrep.2016.12.023.

(8) Games, D.; Valera, E.; Spencer, B.; Rockenstein, E.; Mante, M.; Adame, A.; Patrick, C.; Ubhi, K.; Nuber, S.; Sacayon, P.; et al. Reducing C-Terminal-Truncated Alpha-Synuclein by Immunotherapy Attenuates Neurodegeneration and Propagation in Parkinson's Disease-like Models. *J. Neurosci.* **2014**, *34* (28), 9441–9454. https://doi.org/10.1523/JNEUROSCI.5314-13.2014.

(9) Parsegian, V. A.; Rand, R. P.; Fuller, N. L.; Rau, D. C. Osmotic Stress for the Direct Measurement of Intermolecular Forces. *Methods Enzymol.* **1986**, *127* (C), 400–416. https://doi.org/10.1016/0076-6879(86)27032-9.

(10) Cohen, J. A.; Highsmith, S. An Improved Fit to Website Osmotic Pressure Data. *Biophys. J.* **1997**, *73* (3), 1689–1694. https://doi.org/10.1016/S0006-3495(97)78200-6.

(11) Park, K.; Koerner, H.; Vaia, R. A. Depletion-Induced Shape and Size Selection of Gold Nanoparticles. *Nano Lett.* **2010**, *10* (4), 1433–1439. https://doi.org/10.1021/nl100345u.

(12) Björkegren, S. M. S.; Nordstierna, L.; Törncrona, A.; Persson, M. E.; Palmqvist, A. E. C. Surface Activity and Flocculation Behavior of Polyethylene Glycol-Functionalized Silica Nanoparticles. *J. Colloid Interface Sci.* **2015**, *452*, 215–223. https://doi.org/10.1016/j.jcis.2015.04.043.

(13) Israelachvili, J. *Intermolecular and Surface Forces*; Elsevier Inc., 2011. https://doi.org/10.1016/C2009-0-21560-1.

(14) Lautenschläger, J.; Stephens, A. D.; Fusco, G.; Ströhl, F.; Curry, N.; Zacharopoulou, M.; Michel, C. H.; Laine, R.; Nespovitaya, N.; Fantham, M.; et al. C-Terminal Calcium Binding of α-Synuclein Modulates Synaptic Vesicle Interaction. *Nat. Commun.* **2018**, *9*, 712. https://doi.org/10.1038/s41467-018-03111-4.

(15) Lowe, R.; Pountney, D. L.; Jensen, P. H.; Gai, W. P.; Voelcker, N. H. Calcium(II) Selectively Induces α-Synuclein Annular Oligomers via Interaction with the C-Terminal Domain. *Protein Sci.* **2009**. https://doi.org/10.1110/ps.04879704.

(16) Li, W.; West, N.; Colla, E.; Pletnikova, O.; Troncoso, J. C.; Marsh, L.; Dawson, T. M.; Jäkälä, P.; Hartmann, T.; Price, D. L.; et al. Aggregation Promoting C-Terminal Truncation of α-Synuclein Is a Normal Cellular Process and Is Enhanced by the Familial Parkinson's Disease-Linked Mutations. *Proc. Natl. Acad. Sci. U. S. A.* **2005**. https://doi.org/10.1073/pnas.0406976102.

(17) Yin, G.; Lopes da Fonseca, T.; Eisbach, S. E.; Anduaga, A. M.; Breda, C.; Orcellet, M. L.; Szego, É. M.; Guerreiro, P.; Lázaro, D. F.; Braus, G. H.; et al. α-Synuclein Interacts with the Switch Region of Rab8a in a Ser129 Phosphorylation-Dependent Manner. *Neurobiol. Dis.* **2014**, *70*, 149–161. https://doi.org/10.1016/j.nbd.2014.06.018.

(18) Burré, J.; Sharma, M.; Tsetsenis, T.; Buchman, V.; Etherton, M. R.; Südhof, T. C. Alpha-Synuclein Promotes SNARE-Complex Assembly in Vivo and in Vitro. *Science* **2010**, *329* (5999), 1663-1667.

(19) Goedert, M. Alpha-Synuclein and Neurodegenerative Diseases. *Nat. Rev. Neurosci.* **2001**, 492–501. https://doi.org/10.1038/35081564.

(20) George, J. M. The Synucleins. *Genome Biol.* **2002**. https://doi.org/10.1186/gb-2001-3-1-reviews3002.

CHAPTER 5.

UNDERSTANDING THE SELECTIVE BINDING OF α-SYNUCLEIN TO SYNAPTIC VESICLES

5.1. Overview: A biologically driven hypothesis for αS binding to neurotransmitter-loaded synaptic vesicles

The previous two chapters showed that αS sterically stabilizes membrane surfaces via its polymeric properties and yet, much remains unknown about what physiological contexts drive αS membrane selectivity (assuming the lipid composition of synaptic vesicle does not significantly change during its cycle and composition is not a consideration) and how αS can "sense" which synaptic vesicle membrane to bind. This question was driven in part by the observation that GFP-tagged αS selectively associated with a sub-population of synaptic vesicles in live cells (Chapter 4.6).

We began thinking about this question by understanding that not all synaptic vesicle membrane surfaces are "equal" because structural changes accompany the synaptic vesicle surface once the vesicle is loaded with neurotransmitters.[1] This observation was remarkable in that the synaptic vesicle, normally monodisperse at 40 nm, swells to 60 nm upon loading and possibly alters its membrane protein rearrangements so that its surface no longer resembles that of a neurotransmitter-unloaded vesicle. This finding is illuminating in light of yet another observation that synaptic vesicle mobilization from clustered pools is likely *initiated* by neurotransmitter loading.[2] It is then conceivable that αS binding to neurotransmitter-loaded vesicle surface can differ from binding to an unloaded surface — and that may be how αS selects some vesicles to bind and sterically stabilizes them in order to dissociate those vesicles from the condensed pool.

We specifically hypothesized that αS binding affinity to synaptic vesicles would significantly increase as a function of neurotransmitter loading. This hypothesis made sense because it aligns with the larger idea that αS binding could be a neuronal mechanism to de-cluster synaptic vesicles. Moreover, this hypothesis appears biophysically sound. Loading and swelling of synaptic vesicles would likely increase membrane tension and defect presentation, which in turn should recruit more αS to the surface. This chapter presents an experiment that mimics neurotransmitter loading of synaptic vesicles using a LUV model system and monitors the binding of αS to LUVs as a function of such loading.

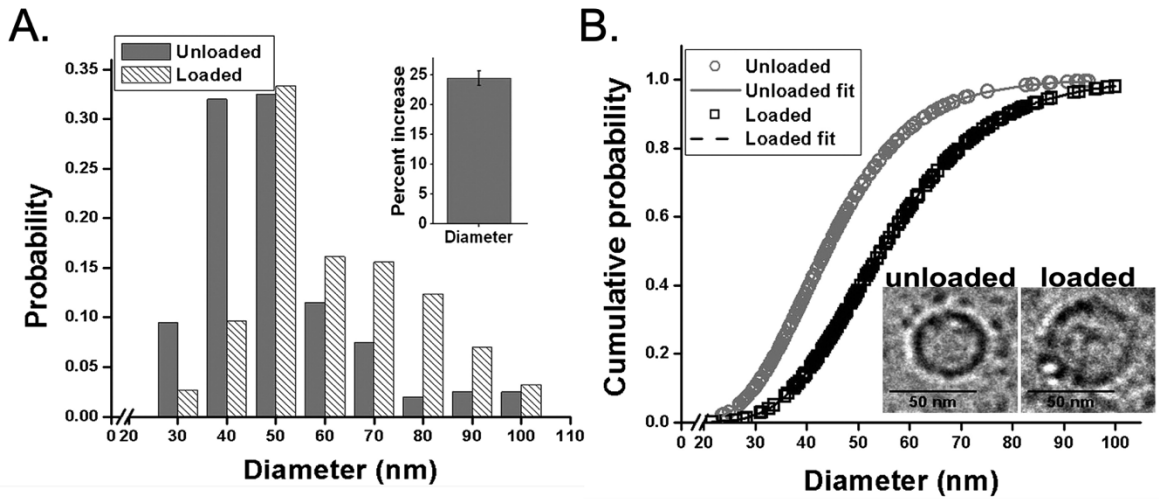

Fig. 5.1. Size expansion accompanies glutamate loading of synaptic vesicles
Cryo-TEM imaging of purified synaptic vesicles unloaded or loaded with glutamate, one of the most abundant neurotransmitters, reveals structural changes to vesicle surface and implies heightened membrane tension upon loading.
(A). Histogram of unloaded and loaded synaptic vesicle diameters. Inset shows an average increase in synaptic vesicle size by ~25%.
(B). Cumulative probability plot of unloaded and loaded vesicle diameters, where the shown fits are lognormal distributions with 45.7 ± 13.9 nm (mean diameter ± SD) for unloaded and 56.9 ± 17.1 nm for loaded. Adapted from ref. (1).

5.2. Materials and Methods

5.2.1. Materials

DOPC, DOPS, DOPE, and Chol lipids were purchased from Avanti Polar Lipids and used without further purification for the preparation of LUVs in a buffer containing 10 mM HEPES, 150 mM NaCl, 150 mM glucose, 0.2 wt.% NaN3 at pH 7.0. The synaptic vesicle composition — composed of DOPC:DOPS:DOPE:Chol (55:20:15:10 mol%) – LUVs were extruded through 50 nm membrane pores (refer to Chapter 2.2 for extrusion procedure). NaN_3 was included in buffer to inhibit bacterial growth in glucose containing medium.

5.2.2. Tryptophan mutation of αS

The mutation followed prior protocols that used tryptophan fluorescence of αS as a binding assay.[3] Single tryptophan residue was introduced at F4 by site directed mutagenesis and subsequently, acid precipitation and chromatographic separation (see Chapter 2.2.7 for details) were performed to purify αSF4W. The concentration was determined by Nanodrop using a molar extinction coefficient, $\varepsilon_{280\,nm} = 10{,}810\ M^{-1}cm^{-1}$. Purified αSF4W was aliquoted and stored at –80˚C until further use.

5.2.3. Tryptophan fluorescence of αS as a binding assay

Tryptophan fluorescence is a classic technique used in biochemistry to measure protein concentration and binding affinity. The amino acid tryptophan excites at 280 nm and emits in 300-420 nm range, which can be detected by standard fluorometers. There are meticulous reviews on the topic of tryptophan fluorescence as a way to probe protein

binding[4,5]; in essence the binding measurement is based on a shift in tryptophan fluorescence of αSF4W that results from the burial of tryptophan in the hydrophobic lipid environment.

We quantitate the shift in fluorescence by first establishing the baseline fluorescence spectrum, $U(\lambda)$, from just αSF4W alone in buffer (corresponding to "0 %" binding of αSF4W to LUVs), and then obtaining the "fully bound" spectrum, $B(\lambda)$, of αSF4W in presence of saturating concentration of LUVs (corresponding to "100 %" binding). With just the protein alone in buffer, the emission peak of αSF4W fluorescence occurs at 350 nm. At a saturating concentration of LUVs, we observe a blue shift in fluorescence to peak wavelength of 325 nm (Fig. 5.2). We define saturating concentration as one in which an addition of LUVs no longer shifts the tryptophan fluorescence. The spectrum taken at the saturating concentration therefore defines the fully bound spectrum for αSF4W binding — corresponding to "100 %" binding with no more available binding sites. By establishing the two spectra that respectively represent 0 and 100% binding, any intermediate binding can be understood as a linear combination of these two spectra. In other words, if αSF4W partitions between these two states, the bound fraction of αSF4W can be calculated by

$$F(\lambda) = b \cdot B(\lambda) + (1 - b) \cdot U(\lambda) \quad (5.1)$$

where $F(\lambda)$ is the experimentally obtained spectrum; b is the bound fraction; $B(\lambda)$, the fully bound spectrum; and $U(\lambda)$, the free αSF4W spectrum without LUVs.

Tryptophan fluorescence experiments were performed using a spectrofluorometer (Horiba Fluorolog-3) equipped with a xenon short arc lamp, using an excitation wavelength of 280 nm and a recording range of 300–420 nm, with the sample stage at

37˚C. The sample was pipetted into a 3-mL quartz cuvette that has a pathlength of 1 cm. The cuvette contained 980 µL of buffer, 20 µL of αSF4W (whose concentration was typically ~7 µM), and a chosen volume of LUVs (typically at 20 mM total lipid concentration) for a desired lipid-protein ratio.

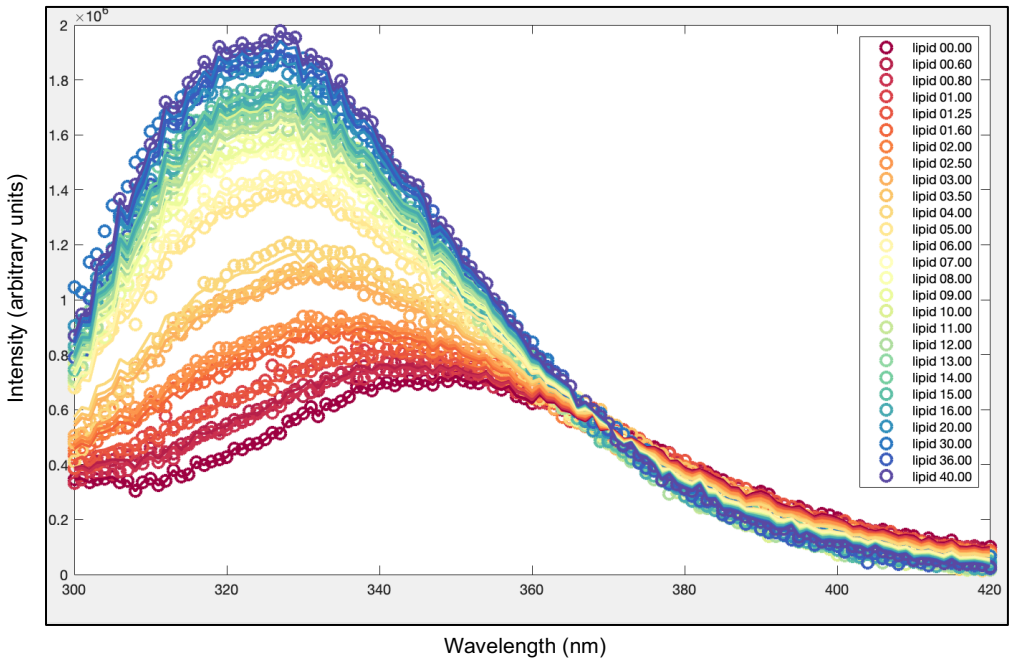

Fig 5.2. An example of background subtracted fluorescence data showing a progressive shift in tryptophan fluorescence
A series of background subtracted fluorescence spectra as a function of increasing lipid-αSF4W ratio. The legend indicates total LUV volume (20 mM lipid concentration) injected into cuvette (~1 mL total volume) containing 7.3 µM αSF4W. The free protein spectrum, $U(\lambda)$, indicated by 'lipid 00.00' curve, shows a peak at 350 nm; with progressive addition of LUVs, there is a blue shift and an increased intensity of tryptophan fluorescence. The fully bound spectrum, $F(\lambda)$, indicated by 'lipid 40.00' curve, shows a peak at 325 nm with signal saturated at that concentration.

For the measurement protocol, 980 µL of preheated buffer at 37˚C was first added to the cuvette, followed by a desired volume of LUVs. The solution was then mixed vigorously using a small magnetic stirrer in the cuvette for a full minute. The fluorescence spectrum was taken for buffer + LUV mixture to obtain the background fluorescence

signal for buffer + LUV at a given concentration. Next, 20 μL of αSF4W was added and the resulting buffer + LUV + αSF4W mixture was stirred for two minutes, and the second spectrum was taken. Subtraction of these two spectra resulted in a curve solely accounting for αSF4W fluorescence. This process was repeated for every LUV concentration, to obtain a series of fluorescence spectra, each of which can be converted to a binding fraction, *b*, by a linear combination analysis described above.

Finally, multiple values of binding fraction *b* are plotted as a function of lipid-protein ratio and the data appropriately fitted to extract binding parameters.

5.2.4. Glucose loading of LUVs (Hypo-osmotic stress protocol)

The glucose loading of LUVs (which can also be understood as applying hypo-osmotic stress to the membrane) was implemented as previously reported.[6] We formed highly concentrated LUVs in physiological buffer containing 150 mM glucose, and prepared five separate buffer solutions all containing the same amount of physiological salt but with different concentrations of glucose: 90, 105, 120, 135, and 150 mM. Prior to taking a fluorescence scan, we pipetted a small volume of LUVs into a large volume of buffer (980 μL) containing less glucose, in order to mimic the transmembrane solute differential found for neurotransmitter loaded synaptic vesicles. Such protocol results in higher glucose concentration within LUVs compared to the outer aqueous environment without lysing the LUVs, and this would subject the LUVs to a hypo-osmotic stress akin to what synaptic vesicle membrane would experience when it loads neurotransmitters — the amount of "solute" within it is greater than the amount that is exterior.

5.2.5. Independent binding sites model to extract binding parameters

The bound fraction, *b*, extracted from a linear combination model explained above, was first plotted as a function of lipid-protein ratio. The set of bound fraction values was fit using a well-known independent binding sites model, which assumes one αS has one single binding site on LUV surface. The equilibrium of protein *P*, binding site *S*, and protein-lipid complex resulting from binding [SP],

$$K_A = \frac{[SP]}{[S][P]} \quad (5.2)$$

where K_A is the association constant, can be rewritten as

$$\frac{[SP]}{[P]_{tot}} = \frac{[SP]}{([S]_{tot} - [SP])([P]_{tot} - [SP])}$$

Here, $[P]_{tot}$ refers to total amount protein, and the $[S]_{tot}$ refers to the total amount of binding sites. Rearranging this quadratic expression in $[SP]$ yields

$$\frac{[SP]}{[P]_{tot}} = \frac{1}{2[P]_{tot}}\left([P]_{tot} + [S]_{tot} + \frac{1}{K_A} \right.$$

$$\left. \pm \sqrt{\left([P]_{tot} + [S]_{tot} + \frac{1}{K_A}\right)^2 - 4[P]_{tot} - [S]_{tot}} \right) \quad (5.3)$$

where $\frac{[SP]}{[P]_{tot}}$ is the bound fraction for protein and K_A, the association constant, can be fit. From experimental design we know the concentrations of $[P]_{tot}$ and $[S]_{tot}$. The model does not reflect protein self-association or cooperativity in binding, which we assume did *not* occur for αS since it is far removed from aggregation conditions. Our TEM images showed no evidence for aggregation on membrane surface or in solution (Chapter 2.5).

5.3. Increase in αS binding affinity to vesicles subjected to osmotically induced tension

We saw a strong increase in the binding affinity of αS to glucose loaded LUVs as a function of LUV loading amount. Comparing the control unloaded LUVs, and slightly loaded LUVs at ΔC = 15 mM (meaning, the glucose concentration within LUVs is 150 mM while outside of LUVs is 135 mM, amounting to a transmembrane differential concentration of 15 mM), the change in affinity was insignificant. However, at ΔC = 30 and 45 mM, K_A increased by seven- and ten-fold, respectively (Fig. 5.3). The increased affinity was reflected in the slope of the binding curves and fitted parameters of binding affinity and binding stoichiometry. While the change in stoichiometry is not significant, the change in affinity is remarkable considering that the membrane composition remained the same and only one membrane property, membrane tension, was physically altered.

The finding that loading of LUVs increasing affinity was similarly reported for the curvature sensing N-BAR protein (Fig. 5.4), where the binding at ΔC = 45 mM, as measured by ultracentrifugation binding assay, increased by a factor of 7 compared to control (ΔC = 0 mM). The increase in affinity also resulted from loading NaCl, which suggested that the effect was osmotic in nature, and not chemically specific. In either case of αS or N-BAR, the increase in affinity would be attributed to the more pronounced hydrophobic interaction between the protein and the membrane. The osmotic effect, which increases the size of the vesicle and thus exposes more of the hydrophobic core of the membrane, likely leads to a deeper burial of protein into the membrane accounting for the significant pelleting in the case of N-BAR or the shift in tryptophan fluorescence in the case of αS.

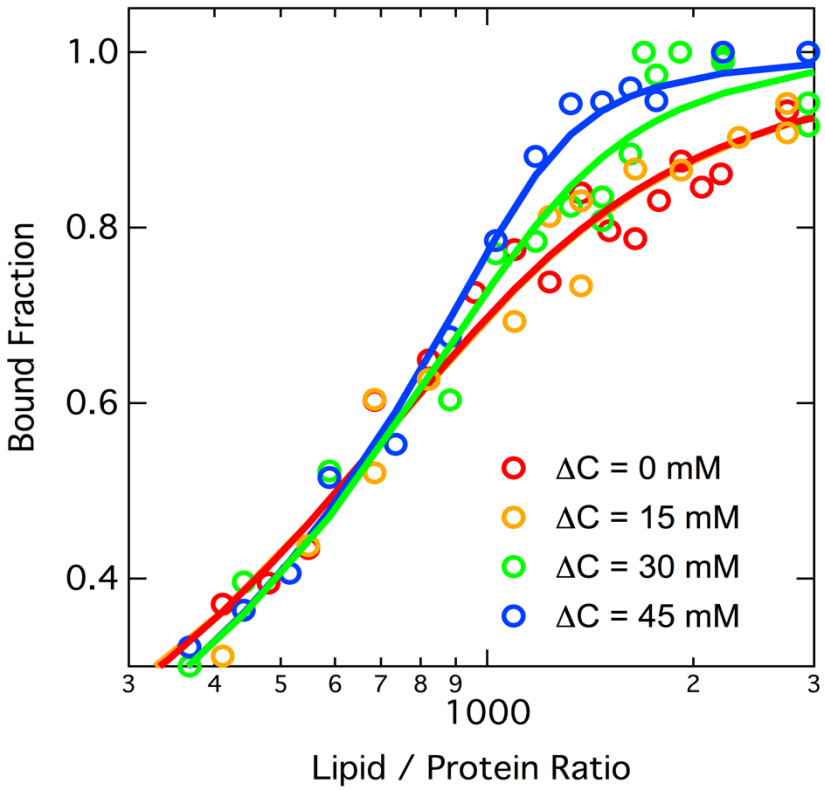

ΔC (mM)	Apparent K_a (μM^{-1})	Lipids per aSF4W binding site
0	34.9	434
15	34.2	431
30	244.8	671
45	334.7	593

Fig. 5.3. Transmembrane glucose gradient of LUVs increases the binding affinity of αS.
An overlay of binding curves as a function of hypo-osmotic stress (or glucose loading) showing the increasing slope of binding curves — corresponding to higher affinity. K_A increased by an order of magnitude from control to ΔC = 45 mM, followed by a modest increase in lipids per bound protein. K_A and binding stoichiometry were fit from Equation (5.3). The curve for ΔC = 60 mM (data not shown) overlaid with ΔC = 45 mM, indicating that the binding increase plateaus.

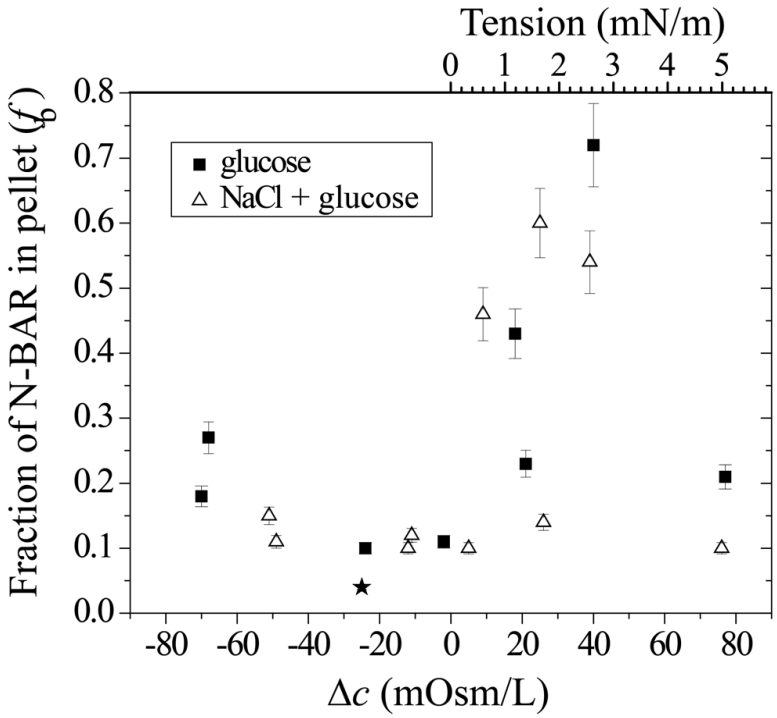

Fig. 5.4. Membrane binding of N-BAR, quantified by the fraction of N-BAR pellet in a sedimentation assay, as a function of applied osmotic stress.
An increase in hypo-osmotic stress (ΔC >0) resulted in a marked increase in N-BAR binding; the fraction of N-BAR in pellet at ΔC = 40 mOsm/L was roughly seven times that of the control experiment at ΔC = 0 mOsm/L. Adapted from ref. (6).

This finding importantly demonstrates that curvature is not the defining parameter for αS binding affinity, as many previous reports would suggest. While the initial biophysical interest in αS stemmed from its membrane curvature sensing, a closer look at αS-lipid interactions showed that it is in fact the lipid *packing defects* that drive αS membrane binding. The glucose loading into LUVs (and subsequent hypo-osmotic stress of vesicles) certainly does not increase curvature and in fact decreases curvature from osmotic swelling, but possibly augmented the presentation of packing defects on surface.

How does glucose loading, and subsequent hypo-osmotic stress, exactly lead to increased packing defects? The transmembrane glucose mismatch leads to water influx

into LUVs, laterally stretching the membrane and therefore increasing the membrane tension overall. The increased tension correlates with the density of defects on the surface, since lateral stretching exposes hydrophobic tail region to the outer aqueous environment. Because packing defect is an intuitive concept, but not an experimental parameter, computational tools have revealed the correlation between membrane tension and defect presentation. The bilayer packing defects, quantitated from atomistic snapshots of the lipid membrane, increased linearly as a function of applied membrane tension.[7,8] The increase in defects would result in an increased hydrophobic insertion. Therefore, αS can be thought of as a membrane tension "sensing" protein, with synaptic vesicles increasing its membrane tension by loading in neurotransmitters.

If this biophysical mechanism of membrane tension sensing is true for αS, we speculate that the selective binding of αS to neurotransmitter-loaded vesicles triggers a release of αS-bound synaptic vesicles from pools to cytosol. To further establish this mechanism, we would have to compare the membrane tension-sensing ability of other proteins within the presynaptic terminal and determine that αS is *uniquely* sensitive to the membrane tension increase resulting from loading. This initial result of αS binding sensitivity to glucose loading of LUVs could be a promising biophysical explanation for αS selective affinity.

5.4. References

(1) Budzinski, K. L.; Allen, R. W.; Fujimoto, B. S.; Kensel-Hammes, P.; Belnap, D. M.; Bajjalieh, S. M.; Chiu, D. T. Large Structural Change in Isolated Synaptic Vesicles upon Loading with Neurotransmitter. *Biophys. J.* **2009**. https://doi.org/10.1016/j.bpj.2009.08.032.

(2) Denker, A.; Rizzoli, S. O. Synaptic Vesicle Pools: An Update. *Front. Synaptic Nerusci.* **2010**, *2*, 135. https://doi.org/10.3389/fnsyn.2010.00135.

(3) Pfefferkorn, C. M.; Lee, J. C. Tryptophan Probes at the α-Synuclein and Membrane Interface. *J. Phys. Chem. B* **2010**, *114* (13), 4615–4622. https://doi.org/10.1021/jp908092e.

(4) Vivian, J. T.; Callis, P. R. Mechanisms of Tryptophan Fluorescence Shifts in Proteins. *Biophys. J.* **2001**, *80* (5), 2093–2109. https://doi.org/10.1016/S0006-3495(01)76183-8.

(5) Chen, Y.; Barkley, M. D. Toward Understanding Tryptophan Fluorescence in Proteins. *Biochemistry* **1998**, *37* (28), 9976–9982. https://doi.org/10.1021/bi980274n.

(6) Hutchison, J. B.; Karunanayake Mudiyanselage, A. P. K. K.; Weis, R. M.; Dinsmore, A. D. Osmotically-Induced Tension and the Binding of N-BAR Protein to Lipid Vesicles. *Soft Matter* **2016**, *12* (8), 2465–2472. https://doi.org/10.1039/c5sm02496j.

(7) Pinot, M.; Vanni, S.; Ambroggio, E.; Guet, D.; Goud, B.; Manneville, J.-B. Feedback between Membrane Tension, Lipid Shape and Curvature in the Formation of Packing Defects. *bioRxiv* **2018**, 389627. https://doi.org/10.1101/389627.

(8) Vanni, S.; Hirose, H.; Barelli, H.; Antonny, B.; Gautier, R. A Sub-Nanometre View of How Membrane Curvature and Composition Modulate Lipid Packing and Protein Recruitment. *Nat. Commun.* **2014**. *5*, 4916. https://doi.org/10.1038/ncomms5916.

CHAPTER 6.

CONCLUSIONS AND FUTURE DIRECTIONS

6.1. Summary of findings and comments

This work probed the membrane-bound behavior of αS on model membrane surfaces mimicking biological synaptic vesicles. The experiments spanned designing an appropriate biophysical SSLB platform whose membrane curvature is enforced; studying its binding of the N-terminal domain to SSLB and LUV surfaces with an enhanced membrane tension; and quantitatively evaluating the polymeric activity of the C-terminal domain by X-ray methods and depletion force response. Taken together these measurements established that membrane binding of αS conferred SSLB steric stabilization, enabled by the C-terminal domain acting as a charged, physisorbed polymer projecting from the membrane. Our findings were contextualized to the synaptic vesicle cycle, where clustering and release of synaptic vesicles from clustered pools are important homeostatic phenomena. Membrane binding is implicated as a biophysical mechanism for the release of synaptic vesicles from clusters. Moreover, the selective binding of synaptic vesicles as a function of neurotransmitter loading was proposed from a membrane biophysical perspective. Our results have led to an important general point in understanding neuronal complexity — that the polymeric properties of proteins along with their steric effects, phase transitions, and weak interactions with other constituents can importantly govern many at-large *in cellulo* behaviors.

The big picture question of physiological function of αS was assessed from the perspective of understanding its C-terminal domain, since the lipid binding N-terminal domain has been studied extensively in literature, in part due to the fact that disease state

mutations mostly manifest in the N-terminal domain. Now we know that in the reduced system of model lipid membranes and αS, the C-terminal domain drives a repulsive steric potential mediating one membrane interaction with another, as a function of the surface density of αS. We approached the force response experiments from a polymer physical view of physisorbed polymer chains (C-terminal domain) on spherical colloids (SSLBs).

What would make this finding more physiologically relevant? If in the future we have more refined knowledge of surface density of αS on a synaptic vesicle depending on its functional state (neurotransmitter-unloaded versus loaded; clustered versus released), we would have a much better grasp on the relevance of biophysics αS in physiology. If we gain detailed knowledge of the C-terminal domain's binding partners at specific synaptic vesicle "states", we could more clearly specify αS role in the synaptic vesicle cycle.

If indeed the C-terminal domain plays the steric repulsive role in physiology, it would be important for us to know how its conformation can possibly alter in response to external environment. We conceived the divalent ion study (Chapter 4.4) as a physiologically relevant external environment affecting the domain's polymeric properties, but force response does not have the molecular resolution to inform us of what is actually happening to the polymer. We tried an experiment early on with the project to examine whether the C-terminal domain can phase transition from a condensed mushroom to an extended brush by increasing its surface density on a Langmuir lipid monolayer and monitoring the monolayer-αS interface via X-ray reflectivity. But αS turned out to be overly surface active and continued to intercalate into the lipid monolayer and disrupt its structure, preventing equilibrium measurements and obfuscating useful analysis that can capture different αS conformational states. Capturing the polymeric

conformational states can be an opportunity to collaborate with structural biologists and biomolecular NMR spectroscopists.

The presynaptic terminal is a particularly relevant study target for biophysicists because this is where intrinsically disordered proteins like αS may play a subtle yet effective physiological function. Disordered proteins defy the conventional paradigm that the three-dimensional structure governs protein function and therefore dynamics is generally less important when there exists a defined structure. This paradigm is ill suited for proteins like αS, however, and now the protein biophysics community is increasingly recognizing this fact — that the structural plasticity of such proteins can be functionally suitable for the formation of weak interactions-driven protein/vesicle clusters, condensates, and membrane-less organelles. If we can better recreate the presynaptic terminal *in vitro*, αS function (as well as those of other intrinsically disordered presynaptic proteins) will be far better understood.

6.2. Future directions

6.2.1. SSLB system development

The questions for next studies on SSLBs as a model should center around how "good" a model system it is, and in what contexts is the system is useful or unworkable. We have developed this model system that can recapitulate curvatures below 100 nm-diameter and that can load highly charged lipids. We measured the binding of αS, a peripherally interacting protein, to SSLBs and compared them against LUVs in order to validate their use as a probe for this protein. These initial findings lead to the specific

molecular question — in what ways is the lipid packing different on a nanoparticle substrate?

There may be several approaches for tackling the question. There are fluorescence and calorimetry experiments that can probe the lipid order of SSLBs. For instance, by incorporating a minute amount of fluorescent lipids or hydrophobic fluorophore (e.g. Laurdan, diphenylhexatriene) that is sensitive to the local hydrophobic environment, we can monitor the changes in fluorescence and quantitate the differences via some order parameter. As another example, we can monitor the thermotropic phase transition of lipids on SSLBs by using nano-differential scanning calorimetry and measure the change in phase transition temperature, which gives an idea about the packing state in the presence or absence of nanoparticle substrate. Spin labels and deuteration can be probe free approaches to examining local molecular arrangements. As mentioned in Chapter 2.4, certain lipids may not form a single lipid bilayer on nanoparticle substrate at all — such as having a high mole fraction of PE lipids in the composition. Mapping out the possible compositions for SSLB formation, while painstaking, would be an important addition to the already existing literature. Furthermore, solving the challenges of colloidal stability would critically improve the system.

Real cell membranes, in fact, can be thought of as a supported lipid bilayer rather than a freestanding one because cytoskeletal network underpins the lipid bilayer. This is to say, freestanding regular LUVs, as much as it is useful and has been taken as a conventional model system for biophysical experiments, do not capture several biophysical features of a real membrane such as membrane tension. Probing the membrane tension of SSLBs via micropipette aspiration or the use of novel fluorescent reporters of tension can be an interesting biophysical direction. As for applications, while

the use of the SSLB system would be limited to peripheral proteins that do not significantly disrupt the lipid bilayer, it can find much broader use for drug delivery system purposes. The SSLBs can be developed on porous nanoparticles to effectively encapsulate the drug cocktail within the particle. Formation on a porous surface could be another interesting direction.

6.2.2. Force response experiments with mutants and synuclein isoforms

The force response experiments revealed the extent of pressure effected by the C-terminal domain for acetylated and truncated αS. On the other hand, mutants have been studied extensively for reduction in their lipid binding affinity and how they promote self-association of αS to form fibrillar structures. How the mutants would affect αS-SSLB force response is an interesting question that delves into how the C-terminal domain might also be responsible for αS dysfunction upon mutation. Perhaps the critical clustering pressure would change dramatically and/or the local order and conformation of the domain may be different — which would allow us to possibly re-contextualize the role of C-terminal domain in disease states. Moreover, the fact that the C-terminal domain is amenable to post-translational modifications (for instance phosphorylation of S127) bring implications for force response, since local charge can be tuned.

β- and γ -Synuclein, comprising the synuclein family in addition to αS, show dissimilar sequence in the C-terminal domain. It is important to know their differential force response, since this knowledge would hypothetically contribute to a more comprehensive picture of how the three isoforms of synucleins constructively (or opposingly) mediate a repulsive intermembrane interaction. Because the differential

localization of the synucleins in the brain has been studied,[1] biophysical insights from their membrane-bound behavior would complement the existing findings to shed light into the overall homeostatic regulatory mechanisms conferred by all three synuclein isoforms in the nervous system.

6.2.3. Towards an improved *in vitro* model of the presynaptic terminal

Our efforts to better replicate the neuronal presynaptic terminal are underway — one of them being the replication of synapsin-1 liquid droplets that phase separate synaptic vesicles into protein rich condensates.[2] We have shown that heightened membrane tension in response to transmembrane osmolyte mismatch drastically increased αS binding affinity. How the αS steric stabilization effect may play out in the context of liquid droplets and an improved *in vitro* model of the synaptic vesicle cycle is an ongoing effort in our laboratory. This includes the question of how the diffusivity of αS-bound SSLBs differs from the diffusivity of SSLBs trapped within condensed synapsin-1 droplet.

From a membrane biophysics perspective, how the αS binding affinity responds to a change in osmotically driven tension as a function of lipid composition is a fundamental question that needs to be explored. With a basic understanding that lipids that promote shallow or deep packing defects (Fig. 1.3) can increase binding affinity, we would ask how the increase in tension differentially affects lipid compositions and then arrive at a detailed understanding of lipid determinants that modulate tension-driven binding.

Lastly, our experiments have relied on model membrane systems, but moving towards physiology would mean the use of purified synaptic vesicles including their

embedded membrane proteins. How the surface activity of αS alters on this membrane protein-rich surface is a question worth pursuing, especially given past findings that the C-terminal domain may have functionally relevant interaction partners (Chapter 1.2). To this end, studying αS interactions with purified synaptic vesicles could be an important next step for our laboratory.

6.3. References

(1) Li, J.; Henning Jensen, P.; Dahlstrom, A. Differential Localization of Alpha-, Beta- and Gamma-Synucleins in the Rat CNS. *Neuroscience* **2002**, *113* (2), 463–478.

(2) Milovanovic, D.; Wu, Y.; Bian, X.; De Camilli, P. A Liquid Phase of Synapsin and Lipid Vesicles. *Science* **2018**, *361* (6402), 604–607. https://doi.org/10.1126/science.aat5671.